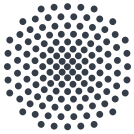

Universität Stuttgart

Advanced fabrication strategies for complex micro-optics

Von der Fakultät Mathematik und Physik
der Universität Stuttgart zur Erlangung der Würde
eines Doktors der Naturwissenschaften (Dr. rer. nat.)
genehmigte Abhandlung

vorgelegt von

Simon Niklas Ristok
aus Schwäbisch Hall

Hauptberichter:	Prof. Dr. Harald Giessen
Mitberichter:	Prof. Dr. Alois Herkommer
Prüfungsvorsitzender:	Prof. Dr. Christian Holm

Tag der mündlichen Prüfung: 19. September 2022

4. Physikalisches Institut der Universität Stuttgart
2022

Simon Niklas Ristok: *Advanced fabrication strategies for complex micro-optics*, 2022

Für Jonathan.

I'm a physicist. I have a working knowledge of
the entire universe and everything it contains.

— Sheldon Cooper, *The Big Bang Theory, S02E18*

ABSTRACT

The rapid evolution of additive manufacturing techniques and an ongoing trend towards miniaturization in many industrial sectors open up completely new approaches for the fabrication of high-tech devices of millimeter or sub-millimeter size. Especially when it comes to optical devices on this scale, the recent advances in the field of 3D printed optical components have resulted in a plethora of new applications. Among the fabrication methods capable of producing optical-grade surfaces, a laser-based 3D printing technique using two-photon polymerization of transparent materials has gained increasing attention over the last years. A highly focused laser beam can locally harden a liquid photoresist with sub-micrometer resolution. By moving the laser focus through the photoresist, arbitrary 3D geometries can be created.

The general aim of this thesis was the investigation, analysis and optimization of different aspects of two-photon polymerization as manufacturing method for optical elements, using a commercial 3D printing system. One of the key goals was the realization of high-quality optics with ~500 µm diameter, which was not possible before due to different limitations. We demonstrate the fabrication of lenses with up to 2 mm diameter, introducing new components and materials to the 3D printing setup. This widens the range of possible applications, as it enables the combination with standard components of similar size, e.g., small camera chips for optical sensors or imaging fiber bundles for endoscopy. Another key element was the optimization of the shape fidelity. While 3D printing can intrinsically create complex shapes, e.g., aspheric or nonrotationally symmetric surfaces, there are typically deviations from the design, induced by intrinsic shrinking of the polymer material. We introduce an iterative optimization procedure, resulting in shape deviations < 1 µm. Using the optimized design of a dual-lens imaging system with ~500 µm diameter, we demonstrate excellent imaging quality. Furthermore, we can fabricate such imaging systems directly on camera chips and image conducting glass fibers, paving the way for various applications. Concerning the efficient use of our advanced high-tech fabrication device, we also investigated a novel printing strategy which can reduce the printing duration by 25%.

In order to improve the performance of 3D printed optical systems, it is straightforward to use additional lenses. Such multi-lens devices are printed in a single step, where all lenses are connected by supporting structures, ensuring perfect alignment. The larger number of lens-air interfaces, in turn, leads to increased reflections, which can deteriorate the optical performance and limit the overall transmission. Therefore, a customized manufacturing process for anti-reflective coatings on multi-lens systems was required. Standard directive coating techniques could not be used, as only surfaces which are directly facing the source of the coating material are coated. This excludes the inner-lying lens surfaces in a 3D printed multi-lens system. Additionally, the polymer lenses must not be exposed to temperatures > 200 °C during the coating process. We solved these challenges by using a low-temperature coating process based on atomic layer deposition. The coating material is deposited from the gas phase, and can therefore move freely into the hollow parts of a multi-lens system. Our coatings reduce the reflectivity in the visible wavelength spectrum to below 1% and increase the transmission through a dual-lens imaging system by 20%.

As there is a rising demand for polymer (micro-)optics, e.g., for smartphone cameras, fabrication methods for mass-production are also of interest. We investigated the direct structuring of a mold insert for injection-compression molding, a standard large-scale reproduction technique. A focused ion beam is used to mill the inverse geometry of a Fresnel lens into a titanium mold insert. Compared to the standard nickel mold inserts, titanium has the potential to sustain a larger number of molding cycles. Our direct structuring approach does not require an additional inversion step, reducing the susceptibility to errors throughout the fabrication process. We apply an iterative optimization procedure similar to the optimization of 3D printed optics. The Fresnel lenses made by injection compression molding using our titanium mold insert exhibit high imaging quality in good agreement with simulations.

In summary, the advances presented in this thesis contribute to the available tool-box of microfabrication techniques for optical elements and can potentially also be transferred to and combined with other fields. Particularly the 3D printing by two-photon polymerization is a powerful and versatile fabrication technique used for a wide range of applications, e.g., in micro-fluidics and biomedical applications. Combining the optical elements introduced in this work with 3D printed structures from different fields could lead to cutting-edge innovative devices and novel intriguing research topics.

DEUTSCHE ZUSAMMENFASSUNG

Die rasante Weiterentwicklung additiver Fertigungsverfahren und eine anhaltende Tendenz hin zur Miniaturisierung in den verschiedensten Industriezweigen ermöglichen völlig neue Möglichkeiten für die Herstellung von High-Tech Komponenten mit Abmessungen im Millimeter- oder sub-Millimeterbereich. Gerade bei optischen Komponenten konnten durch die Fortschritte in der 3D-Drucktechnik vielfältige neue Anwendungsgebiete erschlossen werden. Unter den verschiedenen Herstellungsverfahren für Oberflächen optischer Güte hat vor allem ein laserbasiertes 3D-Druckverfahren in den letzten Jahren für Aufsehen gesorgt, welches das Prinzip der Zwei-Photonen-Polymerisation nutzt. Dabei wird ein flüssiger, transparenter Fotolack durch einen fokussierten Laserstrahl mit sub-Mikrometer Auflösung lokal ausgehärtet. Durch die gezielte Verschiebung des Fokus im Fotolack können nahezu beliebige 3D-Strukturen hergestellt werden.

Das Ziel dieser Arbeit war die Untersuchung und Optimierung verschiedener Aspekte der Zwei-Photonen-Polymerisation für die Herstellung von optischen Elementen. Hierbei kam ein kommerziell erhältliches 3D-Drucksystem zum Einsatz. Damit war es zunächst nicht ohne Weiteres möglich, Optiken mit Durchmessern > 500 µm zu fertigen. Dieser Größenbereich ist interessant, da hier Kombinationen mit anderen Bauteilen ähnlicher Größe möglich werden, z.B. mit kleinen Kamerachips für optische Sensoren oder mit Bildleitfasern für die Nutzung in der Endoskopie. Der 3D-Druck von Linsen mit bis zu 2 mm Durchmesser wird ermöglicht, indem der bestehenden 3D-Drucker um neue optischen Komponenten und ein neues Material erweitert wird. Ein weiteres wichtiges Thema war die Formtreue der gedruckten Optiken. Zwar ist es mit 3D-Druck problemlos möglich, komplizierte Oberflächen wie z.B. Asphären oder nicht-rotationssymmetrische Geometrien herzustellen, aber durch das Schrumpfen des Linsenmaterials kommt es zwangsläufig zu Abweichungen von der Soll-Form. Durch ein iteratives Optimierungsverfahren können Abweichungen < 1 µm erreicht werden. Zweilinsige Abbildungssysteme mit ~500 µm Durchmesser, die auf diese Weise optimiert wurden, besitzen eine hervorragende Abbildungsqualität. Solche Linsensysteme können ebenfalls direkt auf Kamerachips und Glasfasern gedruckt werden, was viele neue Anwendungsmöglichkeiten eröffnet. Um das Drucksystem effizient zu nutzen wurde weiterhin untersucht,

wie die Prozesszeit verringert werden kann. Dies ist mit einer neuartigen Druckstrategie möglich, die eine um 25% kürzere Druckdauer ermöglicht.

Ein bewährtes Mittel, um die Leistungsfähigkeit eines optischen Systems zu erhöhen, ist das Hinzufügen weiterer Linsen. Solche Mehrlinsensysteme lassen sich über 3D-Druck in einem einzigen Prozessschritt fertigen, indem die einzelnen Linsen durch ebenfalls gedruckte Abstandshalter miteinander verbunden sind. So wird gleichzeitig der korrekte Abstand zwischen den Linsen und die perfekte Zentrierung auf der optischen Achse gewährleistet. Durch die vielen optischen Grenzflächen entstehen jedoch vermehrt Reflexionen, die einen negativen Einfluss auf die Abbildungsqualität haben können und das transmittierte Licht reduzieren. Deswegen sollte ein Prozess gefunden werden, der die Herstellung von Antireflexbeschichtungen auf 3D-gedruckten Mehrlinsensystemen ermöglicht. Da bei klassischen Beschichtungsverfahren das Material meist aus einer bestimmten Richtung auf die Linsen trifft, können nie alle Oberflächen eines 3D-gedruckten Mehrlinsensystems gleichzeitig beschichtet werden, weil die innenliegenden Flächen nicht getroffen werden. Weiterhin darf die Prozesstemperatur für Polymerlinsen maximal 200 °C betragen. Diese Anforderungen werden durch einen Niedrigtemperaturprozess mit Hilfe von Atomlagenabscheidung erfüllt. Dabei wird die Beschichtung aus der Gasphase heraus aufgebracht. Da die Gasmoleküle problemlos auch die innenliegenden Flächen erreichen, wird die Antireflexbeschichtung gleichzeitig und homogen auf allen Oberflächen des Mehrlinsensystems aufgebracht. Die gezeigten Beschichtungen reduzieren die Reflektivität im sichtbaren Spektralbereich auf maximal 1% und steigern die Transmission durch ein zweilinsiges Abbildungssystem um 20%.

Aufgrund der steigenden Nachfrage nach Polymerlinsen, z.B. für Smartphonekameras, sind Verfahren zur Massenfabrikation solcher Optiken ebenfalls von Interesse. Ein Spritzprägewerkzeug aus Titan soll mit einem fokussierten Ionenstrahl direkt strukturiert werden. Spritzprägen ist ein Standardverfahren für die Massenherstellung, bei dem normalerweise Werkzeuge aus Nickel benutzt werden, welche die inverse Geometrie der gewünschten Optik beinhalten. Das harte Titan verspricht im Vergleich zu Nickel eine längere Lebensdauer und damit eine größere Anzahl von Spritzprägevorgängen. Durch das direkte Strukturieren wird ein Inversionsschritt vermieden, was die Fehleranfälligkeit in der Prozesskette reduziert. Für die Optimierung der inversen Geometrie im Titan wurde ein ähnliches Verfahren wie bei den 3D-gedruckten Linsen eingesetzt. Am Beispiel einer durch Spritzprägen

gefertigten Fresnel-Linse konnte die gute Abbildungsqualität in Übereinstimmung mit Simulationen gezeigt werden, was die hohe Qualität des hergestellten Titanwerkzeugs bestätigt.

Die hier vorgestellten neuartigen Herstellungsprozesse erweitern die Liste der zur Verfügung stehenden Methoden für die Fertigung von Mikrooptiken, können jedoch potentiell auch auf andere Themengebiete übertragen oder mit diesen kombiniert werden. Gerade der 3D-Druck mittels Zwei-Photonen-Polymerisation ist eine sehr vielseitige Fertigungsmethode und wird in vielen verschiedenen Feldern genutzt, z.B. für Mikrofluidik und in biomedizinischen Anwendungen. Die Kombination aus den hier gezeigten 3D-gedruckten Optiken und gedruckten Elementen aus anderen Themengebieten könnte zu neuen, hochintegrierten Komponenten führen und zur Erschließung neuer spannender Forschungsfelder beitragen.

CONTENTS

1 Introduction 5
1.1 Thesis outline . . . 8
2 Fundamentals 11
2.1 Two-photon-absorption . . . 12
2.2 Two-photon polymerization . . . 16
2.3 Nanoscribe Photonic Professional GT . . . 25
2.4 Nanoscribe Quantum X . . . 35
3 Doublet imaging systems 39
3.1 Optical design and 3D models . . . 40
3.2 Shape optimization . . . 43
3.3 Printing on imaging fibers . . . 49
3.4 Printing on camera sensors . . . 56
3.5 Writing time reduction by core-shell writing . . . 62
3.6 Conclusion . . . 66
4 3D Printed Lenses on the Millimeter Scale 69
4.1 Introduction . . . 70
4.2 Lens fabrication . . . 71
4.3 Aspherical focusing lens . . . 73
4.4 Comparison with glass lenses . . . 76
4.5 Post-printing surface smoothing . . . 82
4.6 Conclusion . . . 85
5 Anti-reflective Coatings for 3D Printed Lenses 87
5.1 Introduction . . . 88
5.2 Atomic layer deposition . . . 90
5.3 AR coating design . . . 92
5.4 Reflectivity measurements . . . 95
5.5 Transmission measurements . . . 99
5.6 AR coated doublet lens . . . 105
5.7 Conclusion . . . 108
6 Mass-producible Diffractive Optical Elements 111
6.1 Introduction . . . 112
6.2 Fabrication and replication . . . 113
6.3 Shape optimization . . . 115
6.4 Imaging characterization . . . 117

6.5 Conclusion 120
7 Conclusion 121
8 Outlook 125
A List of available focusing objectives 127
B Fabrication parameters for 3D printing 129
List of Acronyms 141
List of Figures 142
List of Tables 145

Bibliography 149
Acknowledgments 163

PUBLICATIONS

Parts of this thesis and associated work have been published in scientific journals, have been submitted to a journal, are being prepared for publication, and/or have been presented at national and international conferences.

JOURNAL PUBLICATIONS

P1 S. Ristok, P. Flad, and H. Giessen
"**Atomic layer deposition of conformal anti-reflective coatings on complex 3D printed micro-optical systems**",
Optical Materials Express **12**, 2063-2071 (2022),
DOI 10.1364/OME.454475.

P2 S.Ristok, S. Thiele, A. Toulouse, A. M. Herkommer, and H. Giessen
"**Stitching-free 3D printing of millimeter-sized highly transparent spherical and aspherical optical components**",
Optical Materials Express **10**, 2370-2378 (2020),
DOI 10.1364/OME.401724.

P3 S. Ristok, M. Roeder, S. Thiele, M. Hentschel, T. Guenther, A. Zimmermann, A. M. Herkommer, and H. Giessen
"**Mass-producible micro-optical elements by injection compression molding and focused ion beam structured titanium molding tools**",
Optics Letters **45**, 1184-1187 (2020),
DOI 10.1364/OL.385599.

P4 D. Schäffner, T. Preuschoff, S. Ristok, L. Brozio, M. Schlosser, H. Giessen, and G. Birkl
"**Arrays of individually controllable optical tweezers based on 3D-printed microlens arrays**",
Optics Express **28**, 8640-8645 (2020),
DOI 10.1364/OE.386243.

P5 A. V. Baranikov, S. Q. Li, D. Eschimese, X. Xu, S. Thiele, S. Ristok, R. M. Veetil, T. W. W. Mass, P. Moitra, H. Giessen, R. Paniagua-Domínguez, and A. I. Kuznetsov
"**80-degree field-of-view transmissive metasurface-based spatial light modulator**",
arXiv preprint (2021)
DOI 10.48550/ARXIV.2107.11096.

P6 S. Fischbach, A. Schlehahn, A. Thoma, N. Srocka, T. Gissibl, S. Ristok, S. Thiele, A. Kaganskiy, A. Strittmatter, T. Heindel, S. Rodt, A. Herkommer, H. Giessen, and S. Reitzenstein
"**Single Quantum Dot with Microlens and 3D-Printed Micro-objective as Integrated Bright Single-Photon Source**",
ACS Photonics **4**, 1327-1332 (2017),
DOI 10.1021/acsphotonics.7b00253.

CONFERENCE CONTRIBUTIONS AS PRESENTING AUTHOR

C1 S. Ristok, S. Thiele, A. Toulouse, A. M. Herkommer, and H. Giessen
"**Stitching-free 3D printing of millimeter-sized highly transparent spherical and aspherical optical components**",
CLEO Technical Conference, All-Virtual (2021), Conference presentation.

C2 S. Ristok, S. Thiele, A. Toulouse, A. M. Herkommer, and H. Giessen
"**Stitching-free 3D printing of millimeter-sized highly transparent spherical and aspherical optical components**",
SPIE Photonics West, All-Virtual (2021), Conference presentation.

C3 S. Ristok, S. Thiele, A. Toulouse, A. M. Herkommer, and H. Giessen
"**Millimeter-sized 3D printed high-quality optical elements**",
Spring Meeting of the German Physical Society (DPG), München, Germany (2019), Conference presentation.

C4 S. Ristok, K. Weber S. Thiele, M. Schmid, T. Gissibl, A. M. Herkommer, and H. Giessen
"**3D Printing of Complex Microoptics**",
IEEE International Conference on Nano/Micro Engineered and Molecular Systems, Singapore (2018), Conference presentation.

C5 S. Ristok, S. Thiele, T. Gissibl, A. M. Herkommer, and H. Giessen
"**Shape fidelity of 3D printed microoptics**",
Spring Meeting of the German Physical Society (DPG), Erlangen, Germany (2018), Conference presentation.

C6 S. Ristok, S. Thiele, T. Gissibl, A. M. Herkommer, and H. Giessen
"**3D direct laser writing of camera lenses on CMOS substrates**",
Fraunhofer IISB Lithography Simulation Workshop, Behringersmühle, Germany (2017), Conference presentation.

C7 S. Ristok, S. Thiele, T. Gissibl, A. M. Herkommer, and H. Giessen
"**Diffraction-limited imaging with 3D printed complex mesoscale objectives**",
Spring Meeting of the German Physical Society (DPG), Mainz, Germany (2017), Conference presentation.

1

INTRODUCTION

Optical lenses have been used by humans for many centuries, with early examples dating back to the ancient high-cultures of Egypt and Greece. In his comedy play "The Clouds" from 420 B.C., the Greek playwright Aristophanes already mentioned the use of a rudimentary burning-glass. The stone from which the burning-glass was made is referred to as a "... beautiful and transparent one, from which they kindle fire" [1]. In the historical context, this is a comparably advanced and abstract way of using an optical lens. The main driving force empowering the development of optical elements throughout the ages was the human desire to look at nature in more detail, e.g., by the use of a magnifying glass or a telescope. This motivation is still present in different fields, such as the need for filigree medical endoscopes to access the finest vessels and opening in the human body. Two examples are the root canals in a tooth (endodontics [2]) and the salivary ducts and glands connected to the oral cavity (sialoendoscopy [3]). If medical treatment is required here, e.g., due to an inflammation or the presence of salivary stones, endoscopes with ~1 mm diameter are used. Apart from the imaging optics, this includes also the illumination optics and an optional working channel, all enclosed by a protective housing (Figure 1.1a). This results in a diameter of the imaging optics well below 1 mm.

While the first optical lenses were most likely made from natural transparent crystals, glass was the state-of-the-art material for lens making for a long time. The demand for cheap and lightweight eyeglasses in the last century resulted in the introduction of lenses made from various organic polymer materials. Nowadays, both glass and polymer lenses are standard products and the lens material is selected according to the field of application. The ongoing trend towards miniaturization in many industrial branches has increased the demand for optical elements with diameters on the few-millimeter or even sub-millimeter scale (micro-optics). With decreasing lens

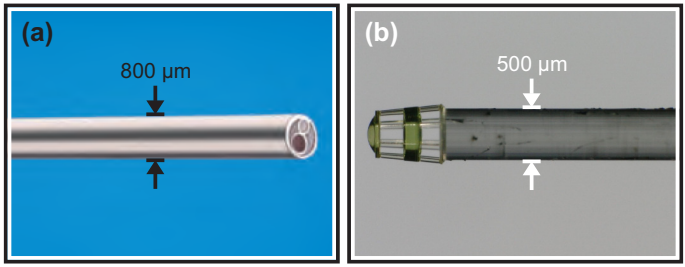

FIGURE 1.1. Commercial endoscope and 3D printed endoscope prototype. **(a)** Semi-flexible endoscope for sialoendoscopy with a full diameter of 800 µm [3]. The circular structures on the tip are the imaging optics and the working channel. **(b)** 3D printed doublet objective on imaging fiber bundle with a diameter of 500 µm. A similar imaging fiber (without 3D printed optics) is used in the endoscope in **(a)**.

diameter, the choice of commercial glass lenses is reduced significantly, as the fabrication by conventional techniques [4] gets more and more challenging. Instead of glass, polymers are often used as lens material here. In terms of lens fabrication, polymer materials have the advantage of being compatible with manufacturing methods for mass-production, e.g., injection molding of lenses for smartphone camera modules. For R&D applications, where an optical system might be designed, produced, evaluated and changed on a daily basis, a different type of fabrication is more feasible, which is the rapidly growing field of additive manufacturing. While there is ongoing research on the topic of glass 3D printing [5–8], polymer-based additive manufacturing methods can already produce surfaces of optical quality [9–13]. Among the numerous available 3D printing techniques used to fabricate optical elements of different size, a direct laser writing (DLW) process based on two-photon polymerization (2PL) has emerged as the perfect method for the 3D printing of optics on the sub-millimeter scale [14–34]. In this process, a laser is focused into a liquid photoresist, which is polymerized in a small, confined volume around the focal spot. The size of this so-called voxel (= volume pixel) can be on the order of a few hundred nanometers, resulting in a superior printing resolution. By moving the laser focus through the material, arbitrary 3D structures can be generated, offering nearly unlimited freedom in the geometry and optical design (free-form surfaces, nonrotationally symmetric lenses, etc.). An intrinsic benefit for the fabrication of multi-lens systems is the perfect alignment of the individual lenses on the optical axis, as all lens elements are printed in a single printing run and

are interconnected by supporting structures, which also ensure the correct distance between the lenses.

In this thesis, different aspects of the 3D printing process by two-photon polymerization in the context of lens fabrication are analyzed and optimized. As this method was first used to fabricate small structures with < 100 µm diameter, one of the main goals was to increase the structure size, in order to combine the printed optics with other optical components, e.g., imaging fiber bundles for endoscopy or small camera chips for optical sensors. We realize two-lens imaging systems with ~500 µm diameter (Figure 1.1b) and demonstrate that even lenses with millimeter size can be printed. Using an iterative optimization process based on shape analysis by confocal microscopy, we can effectively counteract the shape deviations caused by polymer shrinking. Furthermore, a novel two-step printing strategy is investigated in order to reduce the printing duration.

The design freedom of 3D printing enables the fabrication of new optical components, which could scarcely be made by conventional lens manufacturing techniques on the macro-scale. Before the realization of such new devices, however, the fabrication of standard optical components, which are well-known for centimeter-sized lenses, must be transferred and adapted. Apart from aspheric lens surfaces, there are additional ways to improve the imaging quality in a macroscopic complex optical system, namely the use of different lens materials, an absorptive aperture stop and anti-reflective coatings, which decrease reflection losses in multi-lens systems. Multi-material printing [23, 29, 35] and different approaches to incorporate absorptive structures [36, 37] into 3D printed lenses have been demonstrated before. To complete the toolbox of standard components, we introduce a low-temperature coating process, which is not harmful to the polymer lens material and can apply high-quality anti-reflective (AR) coatings to all surfaces of a 3D printed multi-lens system simultaneously.

While the design freedom offered by 3D printing is very convenient for high-end optical applications, there is also a plethora of cases where a single optical surface is sufficient. Such devices can be made in large quantities by injection compression molding, using a molding tool which has the inverse shape of the optical structure. This molding tool is normally made by two inversion steps. We examine a new direct fabrication strategy using focused ion-beam milling, corresponding to only one inversion step and consequently reducing the fabrication effort and the susceptibility to errors. A molding tool for a Fresnel lens is fabricated and optimized, and

the optical quality of the reproduced polymer lenses is found to be close to our simulations.

1.1 THESIS OUTLINE

In the following, a short summary of the content presented in the individual chapters of this thesis is given.

In Chapter 2, the underlying physical and chemical processes of the fabrication principle are introduced first. The main components of the two microfabrication systems used in this work are explained, and the printing process is described step-by-step. We also discuss the limitations and boundary conditions of this 3D printing technique.

The main topic of Chapter 3 is the fabrication of doublet objectives for imaging applications. After introducing the optical design and the 3D models of the objectives, an iterative optimization process is described, which reduces shape deviations. The optimized objectives are then printed on imaging fiber bundles and camera chips, in order to demonstrate their potential use in endoscopic applications or in optical sensors. Finally, a core-shell printing mode is explained, which can reduce the printing duration.

Chapter 4 covers the fabrication of singlet lenses with sizes of 1 mm and 2 mm, combining a new printing objective with a new printing material. The laser focusing ability of an aspheric lens is demonstrated and 3D printed spherical half-ball lenses are compared to identical commercial glass lenses. At the end of the chapter, a post-printing process is introduced, which results in smoother lens surfaces.

In Chapter 5, a low-temperature atomic layer deposition process is developed, which can be used to apply multi-layer anti-reflective coatings on 3D printed lenses without damaging the polymer material. The quality of the AR coatings applied on glass substrates is evaluated first, followed by transmission measurements through coated and uncoated 3D printed test structures. Eventually, we compare doublet imaging systems with and without AR coating in terms of imaging quality and overall transmission.

A mass-production compatible fabrication method for polymer Fresnel lenses is discussed in Chapter 6. The new fabrication approach for mold inserts used in injection compression molding uses focused ion-beam milling to create the inverse Fresnel lens in a Titanium block. The shape of the milled structure in the mold insert is characterized and optimized. Finally, the optical quality of the molded polymer Fresnel lenses is evaluated.

The detailed fabrication parameters for all 3D printed structures shown in this thesis are summarized in the appendix (Tables B.1 - B.20). A list of the available focusing objectives for 3D printing can also be found there in Table A.1.

2

FUNDAMENTALS

In the rapidly expanding field of additive manufacturing, the range of possible applications is often determined by the process material and process volume. When polymer structures with sub-millimeter dimensions and micrometer accuracy are required, fabrication strategies based on two-photon polymerization (2PP) can be used, due to the superior printing resolution. The underlying physical process is called two-photon absorption (2PA) and was first described theoretically by Maria Göppert-Mayer in 1931 in her thesis "Über Elementarakte mit zwei Quantensprüngen" [38]. Thirty years later it was experimentally verified by Kaiser and Garret, who could observe two-photon fluorescence in a crystal [39]. A milestone in the advent of light-induced polymer additive manufacturing was the demonstration of layer-by-layer hardening of a photopolymer with ultraviolet (UV) light to fabricate 3D structures by Kodama in 1981 [40]. The first 3D printing technique based on 2PP was introduced in 1997 by Maruo et al. using a laser with 200 fs pulse width at a wavelength of 790 nm to fabricate spiral structures with sizes of several micrometers [41]. Since then, this technology has developed and evolved to a point where commercial 3D printers based on 2PP are available.

In this chapter, the principle of 2PA is introduced and the probability of such a process is discussed first, followed by the extension to 2PP and the materials for 3D printing. Next, the 3D printers used in this thesis are explained in detail, including boundary conditions and limitations which are important when designing 3D models for printing. Last, the confocal microscopy setup used for the shape analysis of 3D printed lenses, is briefly introduced, as it is a crucial tool for our iterative optimization procedure.

2.1 TWO-PHOTON-ABSORPTION

The transition mechanism of a general 2PA process is sketched in Figure 2.1. A system in the ground state $|g\rangle$ can be excited optically by absorbing two photons at frequencies ω_1 and ω_2, bridging the energy gap $\Delta E = \hbar(\omega_1 + \omega_2)$ between $|g\rangle$ and $|e2\rangle$. The first photon (red arrow) excites the system from $|g\rangle$ to a virtual state (dashed line), and the second photon (green arrow) completes the transition to $|e2\rangle$. As virtual states typically have a very short lifetime, both photons have to be absorbed (nearly) simultaneously. The excited state $|e2\rangle$ can then decay into an energetically lower, but still excited state $|e1\rangle$ (gray dashed arrow). By emitting a photon of frequency ω_3, the system can go back to the ground state via fluorescence (blue arrow). In general, the absorbed photons can have different frequencies, this is called the non-degenerate case. In the following considerations we assume the degenerate case $\omega_1 = \omega_2$, as this is true for our 2PP process where both photons originate from the same laser source.

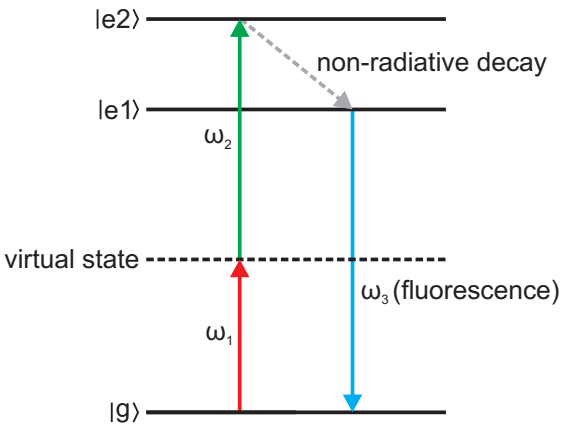

FIGURE 2.1. Transition scheme for two-photon absorption. Simultaneous absorption of photons with frequencies ω_1 (red arrow) and ω_2 (green arrow) excites the system from the ground state $|g\rangle$ to an excited state $|e2\rangle$. By a non-radiative decay (gray dashed arrow) the state $|e1\rangle$ is reached. From here, the transition back to the ground state takes place via fluorescence at the frequency ω_3 (blue arrow). The special case where $\omega_1 = \omega_2$ is called degenerate. Graph based on [42, 43].

Because the two photons need to arrive simultaneously to trigger 2PA, the probability of such an event is very small. Only for a high photon flux density the interaction rate becomes significant. Absorption of light inside a medium is usually characterized by a differential equation of the form

$$\frac{dI(z)}{dz} = -\alpha \cdot I(z) - \beta \cdot I^2(z), \tag{2.1}$$

where the light is propagating in z-direction, $I(z)$ is the light intensity inside the medium, α is the linear absorption coefficient and β the 2PA coefficient. In the following, we assume that there is no single-photon absorption and also neglect higher-order multi-photon absorption processes [44]. The 2PA coefficient β is linked to the molecular 2PA cross-section $\sigma^{(2)}$ by the relation

$$\sigma^{(2)} = \frac{\beta \cdot \hbar\omega}{N}. \tag{2.2}$$

Here, $\hbar$ is the reduced Planck constant, ω is the frequency of the light field and N is the density of the absorbing molecules in the medium. The interaction of an electric field $\mathbf{E}(t)$ with a medium is generally described by the polarization [45]

$$\begin{aligned}\mathbf{P}(t) &= \epsilon_0 \left[\mathcal{X}^{(1)}\mathbf{E}(t) + \mathcal{X}^{(2)}\mathbf{E}(t)\mathbf{E}(t) + \mathcal{X}^{(3)}\mathbf{E}(t)\mathbf{E}(t)\mathbf{E}(t) + \ldots\right] \\ &= \mathbf{P}^{(1)}(t) + \mathbf{P}^{(2)}(t) + \mathbf{P}^{(3)}(t) + \ldots \quad ,\end{aligned} \tag{2.3}$$

where ϵ_0 is the vacuum permittivity and t is time. This is a summation over terms which depend on different powers of the electric field $\mathbf{E}(t)$, and the contributions of the individual terms are determined by the coefficients $\mathcal{X}^{(i)}$. Here, $\mathbf{E}(t)$ and $\mathbf{P}(t)$ are vectors, therefore the coefficients $\mathcal{X}^{(i)}$ are tensors of rank $i+1$. The third-order non-linear polarization

$$\mathbf{P}^{(3)}(t) = \epsilon_0 \mathcal{X}^{(3)} \mathbf{E}^3(t) \tag{2.4}$$

is responsible for the 2PA process. In general, it describes the interaction of three electric fields simultaneously impinging on or emerging from a medium, so $\mathbf{E}^3(t)$ should be replaced by $\mathbf{E}_1(\omega_1)\mathbf{E}_2(\omega_2)\mathbf{E}_3(\omega_3)$, where the fields have different frequencies ω_i and may also have different polarizations. For the degenerate case of 2PA, where both photons have the same energy,

we can use a single frequency ω for the electric field. Furthermore, we assume a plane wave polarized along the x-axis and propagating in z-direction. The scalar field strength $E_x(z,\omega)$ is then given by

$$E_x(z,\omega) = A(z)e^{i(kz-\omega t)}, \tag{2.5}$$

where $A(z)$ is the amplitude of the field and $k = \dfrac{\omega \cdot n}{c}$ is the wavenumber, depending on the speed of light c and on the linear (intensity independent) refractive index n [46]. Equation 2.4 can be simplified to

$$P_x^{(3)}(z,\omega) = 3\epsilon_0 \chi^{(3)}_{xxxx}|E_x(z,\omega)|^2 E_x(z,\omega) = 3\epsilon_0 \chi^{(3)}|E_x(z,\omega)|^2 E_x(z,\omega). \tag{2.6}$$

The indices of $\chi^{(3)}_{xxxx}$ indicate the polarization of the involved vector elements, as we assume polarization along the x-axis we omit the indices from here on. Next, we plug Equations 2.5 and 2.6 into the general non-linear wave equation

$$-\nabla^2 \mathbf{E}(\mathbf{r},t) + \frac{n^2}{c^2}\frac{\partial^2 \mathbf{E}(\mathbf{r},t)}{\partial t^2} = -\frac{1}{\epsilon_0 c^2}\frac{\partial^2 \mathbf{P}^{NL}(\mathbf{r},t)}{\partial t^2}, \tag{2.7}$$

which can be derived from Maxwell's equations [45]. The non-linear term of the polarization $\mathbf{P}^{NL}(\mathbf{r},t)$ is replaced by $P_x^{(3)}(z,\omega)$ from Equation 2.6. After calculating the time derivatives the wave equation is reduced to

$$\frac{\partial^2 E_x(z,\omega)}{\partial z^2} + \frac{n^2\omega^2}{c^2}E_x(z,\omega) = -3\frac{\omega^2}{c^2}\chi^{(3)}|E_x(z,\omega)|^2 E_x(z,\omega). \tag{2.8}$$

When $\frac{\partial^2 E_x}{\partial z^2}$ is calculated, the term $\frac{d^2 A}{dz^2}$ can be neglected according to the slowly varying amplitude approximation [46]. The resulting expression

$$\frac{dA(z)}{dz} = i\frac{3\omega}{2nc}\chi^{(3)}|A(z)|^2 A(z) \tag{2.9}$$

gives a real and an imaginary term for $\frac{dA}{dz}$. We consider only the real part, as this will eventually give us the 2PA coefficient. Because $\chi^{(3)} = \mathrm{Re}\,\chi^{(3)} + i \cdot \mathrm{Im}\,\chi^{(3)}$ only the imaginary part of $\chi^{(3)}$ contributes,

and we loose the imaginary units i on the right side of the equation by using $i \cdot i = -1$, arriving at [47]

$$\frac{dA(z)}{dz} = -\frac{3\omega}{2nc}\mathrm{Im}\left(\chi^{(3)}\right)|A(z)|^2 A(z). \tag{2.10}$$

In the differential equation describing a general absorption process the intensity $I(z)$ is usually used, rather than the field strength amplitude $A(z)$. The time-averaged intensity is given by [45]

$$I = 2n\epsilon_0 c|E_x|^2 = 2n\epsilon_0 c|A|^2 = 2n\epsilon_0 cAA^* \tag{2.11}$$

and the derivative of Equation 2.11 yields

$$\frac{dI(z)}{dz} = 2n\epsilon_0 c\left(A(z)\frac{dA^*(z)}{dz} + A^*(z)\frac{dA(z)}{dz}\right). \tag{2.12}$$

Plugging Equation 2.10 into Equation 2.12 and using the definition of the intensity from Equation 2.11, we arrive at the correlation

$$\frac{dI(z)}{dz} = -\frac{3\omega}{2\epsilon_0 n^2 c^2}\mathrm{Im}\left(\chi^{(3)}\right)I^2(z) \tag{2.13}$$

between $\frac{dI}{dz}$ and I^2, where

$$\beta = -\frac{1}{I^2}\frac{dI}{dz} = \frac{3\omega}{2\epsilon_0 n^2 c^2}\mathrm{Im}\left(\chi^{(3)}\right) \tag{2.14}$$

is the absorption coefficient from Equation 2.1. Using Equation 2.2, the molecular 2PA cross-section $\sigma^{(2)}$ becomes

$$\sigma^{(2)} = \frac{3\hbar\omega^2}{2\epsilon_0 n^2 c^2 N}\mathrm{Im}\left(\chi^{(3)}\right), \tag{2.15}$$

which has the SI unit $\frac{\mathrm{m}^4\cdot\mathrm{s}}{\mathrm{molecule}\cdot\mathrm{photon}}$. In honor of Maria Göppert-Mayer, the unit GM (Göppert-Mayer) is often used:

$$1\mathrm{GM} = 10^{-50}\frac{\mathrm{cm}^4\cdot\mathrm{s}}{\mathrm{molecule}\cdot\mathrm{photon}} \tag{2.16}$$

For a photon flux of 1 photon per second per cm^2 and a density of 1 absorbing molecule per cm^3, a 2PA cross-section of 1 GM corresponds to 1 photon out of 10^{50} being absorbed along the distance of 1 cm [48].

2.2 TWO-PHOTON POLYMERIZATION

In order to successfully use 2PA for 3D printing by 2PP, the light source and the printing material have to meet certain prerequisites. Due to the required high light intensity, a laser with femtosecond pulses is used in combination with a focusing objective with a high numerical aperture (NA). The chemical composition of the printing material should allow the transition from the liquid phase to a solid, polymerized state upon laser irradiation. Common material systems are often designed for hardening by UV light. The main advantage of using infrared light instead for 2PP-based fabrication is illustrated in Figure 2.2. A dilute fluorescein solution is illuminated by light of different wavelengths focused through a microscope objective [49]. Fluorescein molecules can be excited in the blue spectral range and successively decay by emitting green fluorescence light. On the left, blue laser light was used for excitation. The generated fluorescence is visible along the beam

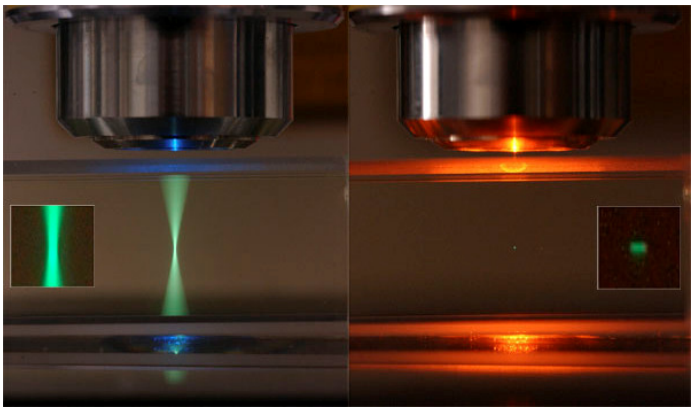

FIGURE 2.2. Comparison of one- and two-photon fluorescence. A dilute fluorescein solution is excited by blue light (left, 1PA) and infrared light (right, 2PA) and emits green fluorescence light. The fluorescence from 1PA is visible all along the laser beam propagation. For 2PA, fluorescence occurs only in a very small region around the laser focus. The insets show zoom-in images of the focal region. Photo from [49].

path of the laser. On the right, infrared light was used for excitation, and here only a very restricted region around the laser focus shows fluorescence, as only there the light intensity is high enough to trigger significant rates of 2PA. The zoom-in insets illustrate the size difference of the fluorescing region between the two excitation wavelengths.

These results for two-photon fluorescence can be transferred to 2PP. If a material which polymerizes upon UV illumination is used, the polymerized regions will resemble the fluorescent regions in the photo. In the case of 2PP, the small volume element around the laser focus which undergoes polymerization is commonly called a voxel (= volume pixel), and its dimensions represent the axial and lateral resolution of a 3D printing system. By moving the laser focus relative to the printing material, complex 3D structures can be fabricated with nearly unlimited design freedom.

2.2.1 *3D printing materials*

Because the polymerization reaction in the laser focus is the center of the 3D printing process, we will now briefly discuss the chemical aspect of the polymerization, and then take a closer look at the intensity distribution close to the laser focus to determine the size and shape of the polymerization voxel. The materials used for 3D fabrication by 2PP in this thesis are transparent liquids with high viscosity. They contain a certain amount of photoinitiator molecules, which can be excited by UV light or 2PA of light in the near infrared (NIR) spectrum. After several internal transition processes, the photoinitiator molecules generate radicals, which start the polymerization reaction [50]. Figure 2.3 shows a simplified scheme of the different stages in a typical radical polymerization. As many available photoresists are acrylic-based materials, the depicted sample molecule also features an acrylic group ($CH_2 = CH - CO$) and a generic organic part R_1. The radical R is generated from the photoinitiator molecule and can attach to the acrylic group. During this process the double bond is broken, resulting in an unpaired electron in the reaction product. This electron can react with the acrylic group of another molecule in the propagation step of the polymerization. The propagation will continue until another radical R reacts with the unpaired electron and terminates the chain reaction. Other chemical compounds of the resist material can also contribute to the termination of the polymerization process, especially the presence of oxygen can have a significant impact on the reaction dynamics [50–52].

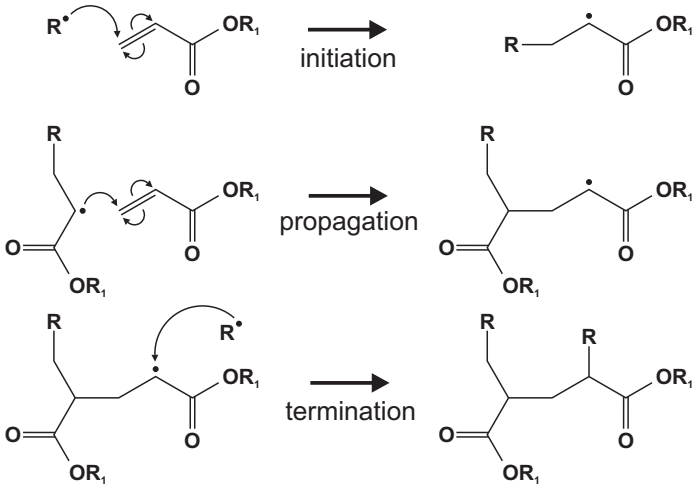

Figure 2.3. Exemplary polymerization scheme for acrylic-based materials. The polymerization starts when a radical R generated from a photoinitiator molecule by 2PA reacts with the acrylic group of a photoresist molecule. The reaction product provides an unpaired electron, which can react with the acrylic group of another molecule in the propagation process. The polymerization is terminated when another radical R reacts with the generated polymer chain. Graph based on [50].

2.2.2 *Gaussian beams*

As we have seen in the previous section, the 2PA cross-section depends on the squared intensity of the incident light. Essentially, there is a minimum threshold intensity above which 2PP occurs. We will now derive formulas for the threshold intensity and the lateral and axial dimensions of the polymerization voxel.

The intensity distribution of the focused laser beam can be described by the Gaussian beam formalism. Here, the spatial dependence of the intensity $I(r,z)$ on the position z on the optical axis and the radial distance r from the optical axis is given by

$$I(r,z) = I_0 \left(\frac{w_0}{w(z)}\right)^2 \exp\left(-\frac{2r^2}{w^2(z)}\right), \tag{2.17}$$

with the beam radius $w(z)$, the beam waist w_0 and the maximum intensity in the beam center I_0. Figure 2.4 shows the important beam parameters.

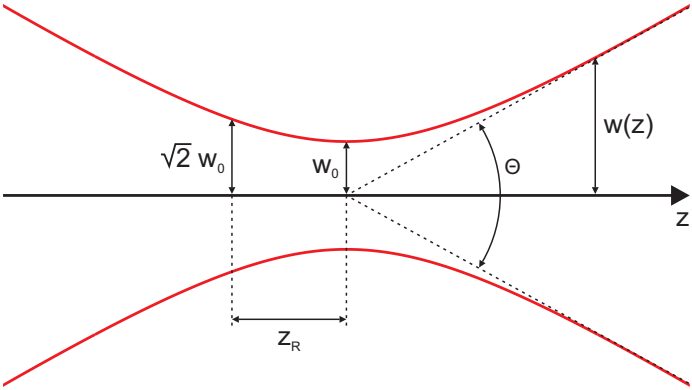

Figure 2.4. Gaussian beam width $w(z)$ plotted in red. In the focus, the beam width corresponds to the beam waist w_0. The Rayleigh length z_R indicates the distance from the focus where the beam width has increased to $\sqrt{2}w_0$. The angle Θ denotes the beam divergence.

The beam radius $w(z)$ denotes the radial position at which the intensity has dropped to $1/e^2$ times the intensity on the optical axis for the same z-position. The beam waist w_0 is the beam radius at the focal position. If focusing objectives with high NA are used, the beam waist can be calculated by [53]

$$w_0 = \frac{\lambda}{\pi \cdot \mathrm{NA}} \sqrt{n^2 - \mathrm{NA}^2}, \tag{2.18}$$

where λ is the laser wavelength and n is the refractive index in the focusing medium, which is the photoresist in the case of direct-immersion 2PP. The beam waist parameter w_0 fully determines the relative intensity distribution in the beam, as the spatial dependence of the beam radius $w(z)$ is also dependent on w_0 via the relation

$$w(z) = w_0 \sqrt{1 + \left(\frac{z}{z_R}\right)^2}, \tag{2.19}$$

in which the Rayleigh length z_R is given by

$$z_R = \frac{\pi \cdot n \cdot w_0^2}{\lambda} \tag{2.20}$$

and indicates the position on the optical axis where the beam diameter has increased to $w(z_R) = \sqrt{2}w_0$.

2.2.3 *Voxel size estimation*

In order to derive the voxel dimensions based on a set of experimental input parameters, the intensity I is not very convenient to work with. Instead, we will use the photon flux density Φ, which is related to the 2PA cross-section $\sigma^{(2)}$ derived earlier (Equation 2.15). As pulsed lasers are usually used for 2PP, parameters such as the laser power P, pulse energy E, pulse width τ and the repetition rate f also influence the voxel size and are therefore included in the calculations. For a pulsed laser, intensity I and photon flux density Φ are connected via the relation [54]

$$\Phi = \frac{I}{\hbar\omega} = \frac{E}{A\tau\hbar\omega}, \tag{2.21}$$

with the reduced Planck constant $\hbar$, the frequency ω of the photon and the cross-section A of the beam. While I is usually measured in $\frac{W}{cm^2}$, the unit of Φ is $\frac{\text{photons}}{cm^2 \cdot s}$.

Apart from the laser parameters, the chemical properties of the photoresist should also be taken into account. The following calculations can be found in detail in the publication by Serbin et al. [55]. As discussed previously, the polymerization process is initialized by the light-induced radical generation from photoinitiator molecules. We can assume that there is a certain threshold concentration ρ_{th} of generated radicals, above which polymerization can occur. The radical concentration $\rho = \rho(r, z, t)$ depends on the intensity $I(r, z)$, which in turn depends on the spatial coordinates r and z. The time dependence of $\rho(r, z, t)$ is described by the differential equation

$$\frac{\partial \rho}{\partial t} = (\rho_0 - \rho(t))\sigma^{(2)}\Phi^2, \tag{2.22}$$

where ρ_0 is the global concentration of photoinitiator molecules, $\sigma^{(2)}$ is the 2PA cross-section and Φ is the photon flux density of the incident laser light. The differential equation is solved by [56]

$$\rho(r, z, t) = \rho_0 \left(1 - \exp\left(-\sigma^{(2)}\Phi^2(r, z)t\right)\right). \tag{2.23}$$

When we now set $\rho(r,z,t) = \rho_{th}$ and rearrange Equation 2.23, we get an expression for the threshold photon flux density Φ_{th} above which polymerization begins [56]:

$$\Phi_{th} = \sqrt{\frac{C}{\sigma^{(2)} \cdot t}} \tag{2.24}$$

$$\text{with} \quad C = \ln\left(\frac{\rho_0}{\rho_0 - \rho_{th}}\right) \tag{2.25}$$

Because intensity and photon flux density differ only by a factor $\hbar\omega$ (Equation 2.21), the photon flux density in the laser focus ($z = 0$) and along the z-axis ($r = 0$) can be described using a Gaussian distribution in analogy to Equation 2.17 as

$$\Phi(r,0) = \Phi_0 \cdot \exp\left(-\frac{2r^2}{w_0^2}\right) \tag{2.26}$$

and

$$\Phi(0,z) = \frac{\Phi_0}{1 + \left(\frac{z}{z_R}\right)^2}. \tag{2.27}$$

For a pulsed laser, the amplitude Φ_0 is in general time-dependent, however, as many pulses are required to reach the necessary radical concentration we can assume time-independence [55]. To facilitate the estimation of the voxel size we also neglect the fact that radicals might be lost between successive laser pulses. When we combine Equations 2.27 and 2.26 with Equation 2.25 by setting $\Phi_{th} = \Phi(r,0)$ or $\Phi_{th} = \Phi(0,z)$, we can now calculate the voxel diameter

$$d = 2r = w_0 \cdot \sqrt{\ln\left(\frac{\sigma^{(2)} \cdot \Phi_0^2 \cdot t}{C}\right)} \tag{2.28}$$

and the voxel length

$$l = 2z = 2z_R \cdot \sqrt{\Phi_0 \sqrt{\frac{\sigma^{(2)} t}{C}} - 1}. \tag{2.29}$$

At this point, we need to consider the physical meaning of the time t in Equations 2.28 and 2.29. What t actually describes is the interaction period between the photons and the medium, represented by the 2PA cross-section $\sigma^{(2)}$. If a pulsed laser is used, we can assume that the interaction is restricted to the temporal center of each pulse with the pulse width τ. The total interaction duration t is then given by

$$t = f \cdot t_{exp} \cdot \tau = m \cdot \tau, \tag{2.30}$$

where f is the repetition rate of the laser and $m = f \cdot t_{exp}$ is the number of pulses arriving during the exposure time t_{exp} when the laser is switched on. Using Equation 2.30 and replacing the photon flux density Φ_0 with the expression [55]

$$\Phi_0 = \frac{2P}{\pi w_0^2 \tau f \hbar\omega}, \tag{2.31}$$

we arrive at the final identities for the voxel diameter d and the voxel length l:

$$d = w_0 \cdot \sqrt{\ln\left(\frac{4\sigma^{(2)} P^2 t_{exp}}{\left(\pi w_0^2 \hbar\omega\right)^2 C f \tau}\right)} \tag{2.32}$$

$$l = 2z_R \cdot \sqrt{\frac{2P}{\pi w_0^2 \hbar\omega} \sqrt{\frac{\sigma^{(2)} t_{exp}}{C f \tau}} - 1}. \tag{2.33}$$

We use these expressions to calculate the voxel dimensions depending on the exposure time t_{exp} for a set of parameters listed in Table 2.1. The material parameters ρ_0, ρ_{th} and $\sigma^{(2)}$ were taken from [55]. Comparing the 2PA cross-section $\sigma^{(2)} = 3 \cdot 10^{-55}\,\mathrm{cm^4\,s}$ with the unit $1\,\mathrm{GM} = 10^{-50}\,\mathrm{cm^4\,s}$ in Equation 2.16, we find that $\sigma^{(2)}$ is much smaller. This is because a conventional, UV-absorbing photoinitiator is used [55]. Other photoinitiator molecules designed specifically for 2PA can have significantly higher absorption cross-sections [58].

Parameter	Value
Wavelength λ	780 nm
Optical frequency $\omega = 2\pi c/\lambda$	$2.415 \cdot 10^{15}$ Hz
Repetition rate f	80 MHz
Pulse width τ	100 fs
Numerical aperture of focusing objective	0.8
Refractive index n of the photoresist at 780 nm	1.505 [57]
2PA cross-section $\sigma^{(2)}$	$3 \cdot 10^{-55}$ cm^{4}s [55]
Concentration of photoinitiator molecules ρ_0	2.4% [55]
Threshold radical concentration ρ_{th}	0.25% [55]

Table 2.1. Parameters used for voxel size estimation.

The curves resulting from plugging the parameters from Table 2.1 into Equations 2.32 and 2.33 are depicted in Figure 2.5. For each curve, the laser power is fixed and the exposure time is varied. The resulting voxel dimensions can be interpreted and used for the concrete laser beam trajectory used in 3D printing. Usually, 3D objects are split into slices with a certain thickness (slicing distance) which are printed consecutively. Each slice consists of many parallel lines separated by a fixed spacing (hatching distance). Looking at Figure 2.5a, we find that the voxel diameter is below 1 µm for all laser powers. If a closed and smooth surface is desired, this is the largest possible hatching distance where adjacent lines still overlap. For larger distances the separation between the lines leads to increased surface roughness. While the voxel diameter is smaller than 1 µm, the length of the voxel can reach several micrometers (Figure 2.5b). In principle, the slicing distance can be chosen as large as the voxel length. This efficiently uses the whole polymerization volume and is beneficial if big volumes have to be printed in limited time. However, the larger slicing steps will be visible in every tilted surface of the printed structure. Therefore, the slicing distance is typically chosen much smaller, in order to achieve better shape accuracy and surface quality. Figure 2.6 illustrates the effect of extreme hatching and slicing parameters. The edges of the cube are 15 µm long, the voxel diameter is assumed to be 1 µm and the voxel length is 5 µm. The cube can then be printed in three slices with 5 µm thickness, which corresponds to the slicing distance. The hatching distance is 1 µm, corresponding to the voxel diameter. Between the lines there are regions which are not covered by the laser trajectory and therefore only experience a lower degree of polymerization (or no polymerization

at all). This can have negative effects for the finished object, e.g., lead to increased shrinking and/or deformations.

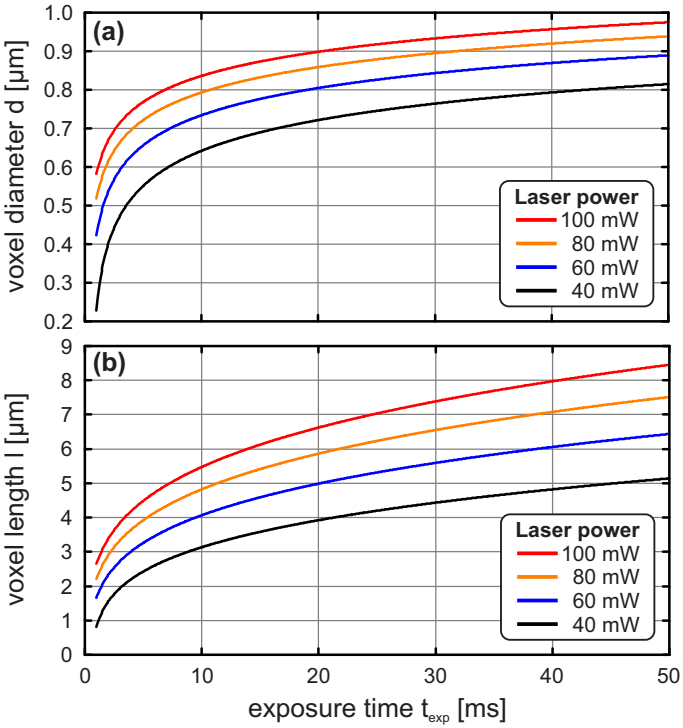

Figure 2.5. Voxel dimensions for different laser power P, depending on the exposure time t_{exp}. **(a)** Voxel diameter d calculated from Equation 2.32. **(b)** Voxel length l calculated from Equation 2.33.

It should be noted at this point that the prediction of the voxel size is a challenging task, as it depends on many parameters. For the present calculations, the laser parameters and numerical aperture of the focusing objective of our own 2PP setup were used. The chemical parameters and the 2PA cross-section in Table 2.1, however, were taken from [55], as those parameters are not readily available for our own printing materials. Nonetheless, the ORMOCER photoresists described in [55] are also standard materials for 2PP,

and therefore should give a good qualitative impression of the dependence of the voxel size on different laser powers and exposure times.

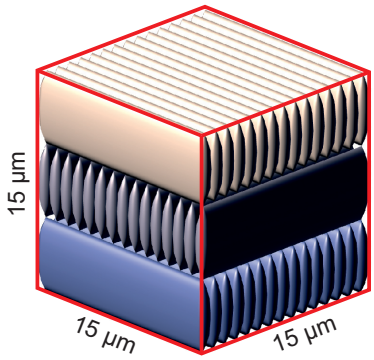

Figure 2.6. Cube with an edge length of 15 µm, separated into three slices with 5 µm thickness (= slicing distance). Each slice contains 15 lines with hatching distance 1 µm.

Next, the two 3D printing systems used in this work are introduced, starting with the Nanoscribe Photonic Professional GT. The improvements and differences of the newer Nanoscribe Quantum X system are discussed afterwards.

2.3 NANOSCRIBE PHOTONIC PROFESSIONAL GT

The Nanoscribe Photonic Professional GT (PPGT) is a commercial micro- and nanofabrication system for polymer structures based on 2PP. First, the working principle and main components are explained, followed by a detailed discussion of the steps from an optical design to a printed lens. Finally, we also look at different factors limiting the design freedom for this fabrication setup.

2.3.1 *Main components*

An overview of the main components in the setup is depicted in Figure 2.7. At the heart of the machine, a laser generates femtosecond pulses which

deliver the high photon density required for 2PA. Because the printed objects often have dimensions on the sub-millimeter scale, they are printed on a supporting substrate, e.g., a glass slide of 10 × 10 mm² size, which facilitates the further processing and characterization steps. The substrate is mounted on an xyz-piezo stage for high-accuracy positioning. The range of motion for each axis is 300 µm. For larger movements, the whole piezo stage can be moved by a mechanical xy-translation stage. A drop of photoresist is dispensed on the substrate before it is mounted in the setup. The focusing objective, which is part of an inverted microscope, is slowly moved upwards until it gets in contact with the photoresist, which serves as an immersion medium. This printing mode is called dip-in laser lithography (DiLL), and is used for the fabrication of all 3D printed structures presented in this work. The distance between substrate surface and objective is adjusted to equal the objective's working distance using the z-drive of the microscope. When the laser is switched on, the focus lies at the substrate-photoresist interface and the polymerization starts there, forming a connection between the printed

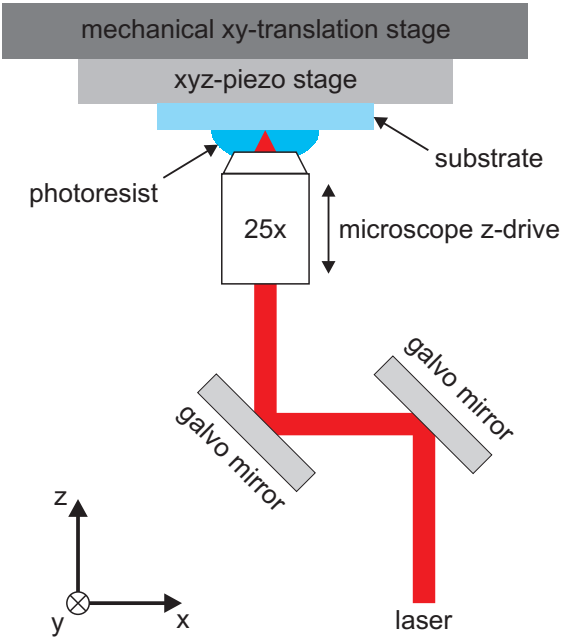

Figure 2.7. Schematic overview of the main components of the Nanoscribe Photonic Professional GT system used for substrate positioning and laser scanning.

structure and the substrate. Arbitrary 3D structures can be generated by moving the laser focus relative to the substrate. Translations in the xy-plane can either be achieved by moving the substrate using the mechanical or the piezo-driven stage, or by moving the laser focus with the use of two galvo mirrors. With these, extremely fast scan speeds are possible, which dramatically reduces fabrication time compared to printing strategies where the piezo stage is used for xy-scanning.

2.3.2 *Printing preparations step-by-step*

Next, we will take a look at the preparation and fabrication steps from an optical lens design to a 3D printed lens. For simple lens designs, e.g., a spherical plano-convex lens, the shape can be calculated analytically. When more complex lenses are required, optimization tools such as ZEMAX OpticStudio are used. As an example, the optical design of a two-lens imaging system is shown in Figure 2.8a. The optical design will be discussed in detail in the next chapter, here it is only used to illustrate the different steps in the printing preparation. For 3D printing, a 3D model of the lens is required, which can be exported directly from the optical design software. Optical designs with multiple lenses often need additional supporting structures outside the light path to adjust the distance between the lenses. Those can be added by standard CAD software, and the combined structure is saved in STL format, which is widely used in the 3D printing community (Figure 2.8b). The STL model is then processed by the Nanoscribe software DeScribe, which virtually cuts the model into slices and fills each slice with an arrangement of parallel hatching lines. The distance between slices (= slicing distance) and between the hatching lines in one slice (= hatching distance) have already been introduced in the previous section and can be set in the DeScribe software (Figure 2.8c). Figure 2.8c and 2.8d also highlight one of the main challenges in 3D printing, the staircasing effect. Instead of a smooth curved lens surface, the lens profile consists of discrete steps of different size, induced by the slicing process. By lowering the slicing distance this effect can be reduced, at the cost of prolonged printing time. This topic will be addressed again later in the thesis. For better visibility, the slicing and hatching distance is chosen very large here (slicing distance = 10 µm, hatching distance = 5 µm). Realistic values for a sufficiently smooth surface are 0.2 µm slicing distance and 0.5 µm hatching distance. The orientation of the hatching lines is usually changed from slice to slice to increase the homogeneity of the printed material, as depicted in the top view of the

lens in Figure 2.8d. Every single hatching line is defined by a pair of 3D coordinates in a text file generated by the DeScribe software. In this file, further adjustments can be made, e.g., including multiple structures or changing different printing parameters. Particularly the laser power and the scan speed can influence the quality of the printed structure. The laser

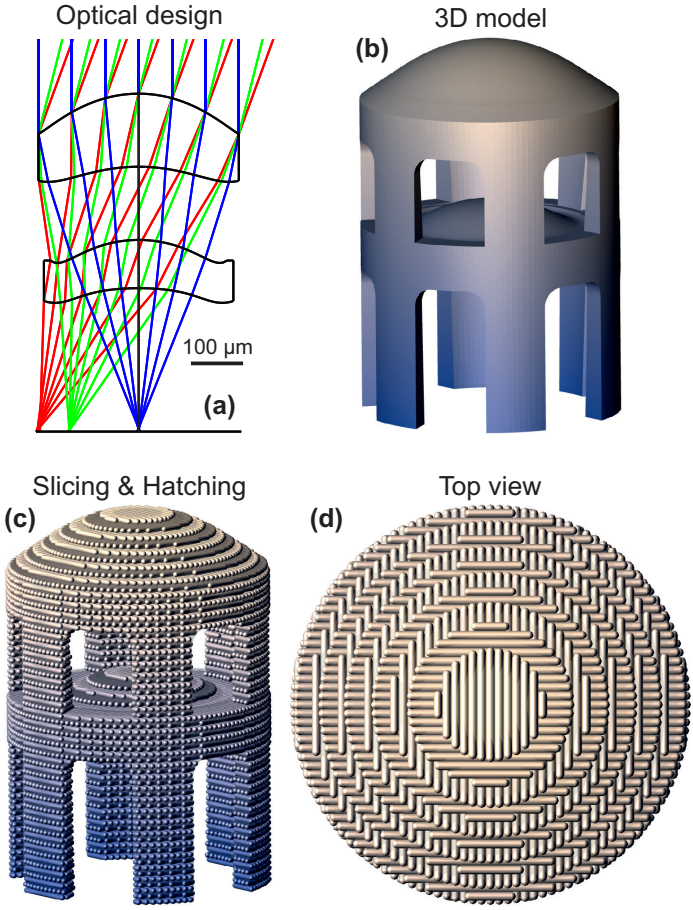

Figure 2.8. Preparation steps for 3D printing using the Nanoscribe PPGT. **(a)** Optical design of a doublet imaging system. **(b)** 3D model of the lens system with supporting structures. **(c)** 3D model processed by the DeScribe software, separated into slices and hatching lines. **(d)** Top view of the 3D model, showing the different hatching angles.

power is not set in absolute values of mW, but as a percentage of a defined reference value (which is determined by adjusting the power going through an objective with 63x magnification to 50 mW). The scan speed is set in units of µm/s. For high laser powers and/or slow scan speeds, the increased energy deposited in the photoresist can lead to the formation of micro-explosions [59], which will usually render the printed structure unusable. The parameter space of possible combinations of laser power and scan speed is called the process window and depends on the used printing material. At this point, the digital part of the preparation is finished, and the printing setup can be prepared for the fabrication process.

The PPGT system is controlled by a computer using the Nanoscribe software NanoWrite. It can be used to put the system in a defined state where it is safe to remove the sample holder without damaging the piezo stage. After removing the holder, the focusing objective with the desired magnification is inserted into the revolver of the PPGT microscope (a list of the available objectives can be found in Table A.1). The glass substrate which will support the printed objects is cleaned with acetone and isopropyl alcohol and dried with nitrogen. It is then exposed to an oxygen plasma for 5 min to increase the adhesion of printed structures to the glass surface [60]. The substrate is fixed on a aluminum sample holder using adhesive tape. A drop of photoresist is dispensed on the substrate and the sample holder is carefully inserted into its position in the machine. For the 3D printed structures in this thesis, two commercial Nanoscribe photoresists were used. The resist IP-S was used for all structures with sub-millimeter diameter, and the resist IP-Visio was used for bigger lenses. The boundary between photoresist and glass substrate can be identified automatically by the NanoWrite software. The interface finding algorithm is based on reflections at the resist-glass interface due to the difference in refractive index. As the printing process starts at the interface, the printed object is fixed to the supporting substrate there. The distance between focusing objective and substrate is increased to fabricate the whole 3D object slice-by-slice. This can be done by moving the substrate upwards with the piezo stage, or by moving the objective downwards with the microscope z-drive. When the first structure is finished, additional structures can be printed at different locations. For each new object, the glass-photoresist interface is searched again automatically. When all structures are printed, the system is put into the exchanger state, the sample holder is removed, and the substrate with the printed structures and the leftover liquid photoresist is immersed in a developing solution (mr-Dev 600, microresist technology) for 25 min. During this time, the liquid resist is dissolved and only the solid, printed objects stay on the substrate.

After another 5 min in an isopropyl alcohol bath the substrate is dried with nitrogen. If there are filigree structures on the substrate, blow-drying should be performed carefully. During sample development the focusing objective is rinsed with isopropyl alcohol to remove excess liquid photoresist.

2.3.3 *Boundary conditions and limitations*

While 3D printing as fabrication technique vastly expands the freedom in optical design, there are a few boundary conditions and restraints which should be considered when creating the lens designs and the CAD model.

Writing field diameter

The diameter of a 3D printed lens is limited by the area in the-xy plane which can be reached by the laser focus using the two galvo mirrors. The diameter of this area is an intrinsic property of the used focusing objective and is called writing field diameter (as the 2PP 3D printing technique is often called direct laser writing). The maximum writing field diameters for the available objectives are listed in Table A.1 in the appendix. For the standard Nanoscribe objectives it is, however, not recommended to use the entire available writing field, as the quality of the printed structures might decrease in the outer regions. The recommended writing field diameter is approximately half of the maximum writing field diameter.

In principle, bigger objects can be printed by separating them into smaller building blocks which fit into the writing field. However, this comes with other limitations and drawbacks. In terms of lens fabrication, the main disadvantage lies in the formation of unavoidable stitching marks at the transition from one block to the next. If they intersect an optical surface, this will deteriorate the quality of the lens.

Piezo stage

When several objects need to be printed with a defined distance in between, the piezo stage is used to move between the printing locations, as its accuracy is on the nanometer scale. The motion range of the piezo stage is 300 µm in each xyz-dimension. If larger distances in the xy-plane are required, the mechanical translation stage has to be used instead, which is not as accurate. Particularly in the z-direction (which normally is the symmetry

axis of rotationally symmetric lenses), the printed optical elements are often higher than 300 µm. In this case, there are two options: Either the z-drive of the microscope is used to move the focusing objective, or the 3D model is separated into segments < 300 µm along the z-direction, which can be printed using the piezo stage. After the fabrication of each segment (during which the piezo stage gradually moves upwards in positive z-direction), the piezo stage is moved back down to its starting position. Then, the focusing objective is moved downwards about the same distance, so the printing of the next segment continues on the surface of the previous one. In this case, the borders of the individual segments should not intersect with any optical surface, but should rather be located at other z-positions in the 3D model, e.g., in the supporting structures of the doublet objective in Figure 2.8b.

Working distance of focusing objective

Often multiple objects are printed on the same substrate, e.g., to print a lens array or to perform a printing parameter sweep. To account for deviations in the substrate thickness or a potential tilt of the substrate, the substrate-photoresist interface is determined every time a new structure is printed. After the interface finding is performed, the distance between the front lens of the focusing objective and the interface is equal to the working distance w of the objective. If any of the previously printed structures is higher than the working distance, the objective might crash into this structure when it is moved during the interface finding process. This can be avoided if the distance between the individual objects is large enough. The geometrical circumstances are illustrated in Figure 2.9. Two micro-objectives were already fabricated, and the printing of the next objective is about to begin. The printed objectives are approximated as cylinders with a flat top, neglecting the shape of the lens surface there (illustrated by the red lines at the top of the printed objective).

The minimum distance L between the printed objectives can be calculated by the formula

$$L = \frac{d}{2} + \frac{a}{2} + \frac{h - w}{\tan\theta}, \tag{2.34}$$

using the diameter d and height h of the printed objectives and the front lens diameter a, the working distance w and the angle θ of the focusing objective. As this is only the minimum distance it is recommended to add a sufficient safety margin.

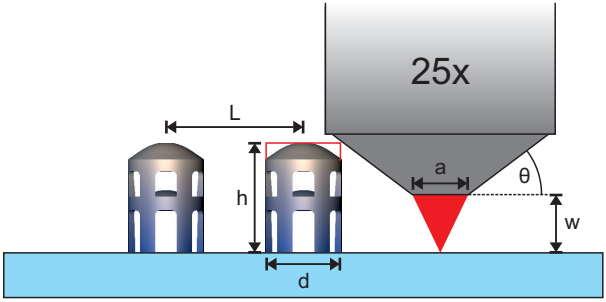

FIGURE 2.9. Array fabrication of high structures. The minimum distance L between structures with diameter d and height $h > w$ (working distance of the focusing objective) depends also on the front lens diameter a and the angle θ of the focusing objective. Due to the big size difference between printed micro-optics and focusing objective the illustration is not to scale.

We calculate the distance L for the standard Nanoscribe 25x objective with working distance $w = 380\,\mu m$, front lens diameter $a = 5.2\,mm$ and angle $\theta = 31°$. The diameter d of the printed structures is assumed to be $450\,\mu m$ and their height h is $650\,\mu m$. This results in a minimum distance between the objects of $L = 3.3\,mm$. When substrates with areas $> 1\,cm^2$ are used, this is not critical, although the large amount of photoresist required to cover the whole substrate increases the probability of bubble formation in the resist. When the substrate size is restricted, however, a focusing objective with larger working distance is beneficial. This is the case for standard Raspberry Pi camera sensors with an area of $3.76 \times 2.74\,mm^2$. A maximum of two objectives can be printed on this sensor with a working distance of $380\,\mu m$. As more objectives might be required, e.g., objectives with different field of view for foveated imaging [61], we introduce a new focusing objective with $740\,\mu m$ working distance for such specific tasks.

Printing overhanging structures

In layer-by-layer additive manufacturing techniques, the fabrication of overhanging parts is often challenging. If the printing process is started on a substrate, like here, the printed object is connected to a fixed structure, and every newly fabricated layer is connected to the substrate as well. Overhanging parts are segments, which are initially not connected to the already printed structure, and hence can move to a certain degree in the liquid photoresist. When this happens for only a few layers, there is normally no

need for special precautions, as the layers are printed fast enough, and the viscosity of the resist is high enough to limit the movement of the loose part. If the overhanging structure is bigger, it is often connected to the substrate by a sacrificial support in commonly used 3D printing techniques [62]. The sacrificial support is removed after the printing is done. Removing such a supporting structure on the micrometer scale is hardly possible without damaging the rest of the printed optical system. A better way to fabricate overhanging parts is explained in detail in Chapter 3. Essentially, the region which will later connect the overhanging part to the rest of the object is printed first, and the overhanging part itself is fabricated afterwards by focusing the laser beam through the already polymerized structure.

Dose accumulation

When a convex lens surface is printed, the diameter of the individual slices decreases towards the top of the lens. In turn, the time required to print the slices decreases as well. Because the voxel length is normally larger than the slicing distance, the voxel reaches into the lower-lying already printed slices. At the top of the lens, multiple slices are printed rapidly after each other, which can result in accumulated energy deposition in the photoresist. This leads to a bulging effect on the top of the lens, visible in shape analysis as a local increase of the lens height close to the top. This effect can be counteracted by increasing the waiting duration between successive slices, which can be set as the parameter PiezoSettlingTime if the piezo stage is used for movement along the z-axis, or has to be manually inserted via a "WAIT" command in the code if the microscope z-drive is used.

Proximity effect

Detailed knowledge of the voxel size and aspect ratio is beneficial for the estimation of hatching and slicing parameters. The voxel dimensions can be determined experimentally, as shown in several publications [55, 63, 64]. However, the size determination often uses a single printed line or point. For solid objects, like a lens, the polymerization voxel is always in close vicinity to regions which were polymerized earlier. The influence of printed structures on the polymerization process was examined in detail by Waller and von Freymann in 2016 [65], indicating that the voxel diameter is increased close to already polymerized structures due to diffusion processes. This is called the proximity effect and has to be considered especially when

structures with very narrow gaps are printed. The proximity effect partly counteracts the staircasing effect by rounding the edges of the individual slices due to the proximity of the underlying printed slice.

Surface analysis by confocal microscopy

Due to shrinking in the printed polymer material, the shape of printed lenses does normally not perfectly match the design. The shape deviations can be minimized by an optimization process introduced in detail in the next chapter. A necessary prerequisite for this process is the accurate knowledge of the printed lens shape. Only then can the deviations be calculated correctly and used for error compensation. The lenses described here typically have a diameter > 500 µm. The initial shape deviation can be in the range of several micrometers and should eventually be reduced at least to below 1 µm. Furthermore, the height of a lens can be several tens or even several hundreds of micrometers. This limits the choice of available measurement techniques. Atomic force microscopy (AFM) has the desired accuracy, but lacks the large-area component and is time-consuming, as it uses a scanning algorithm. Tactile measurement methods are commonly used for bigger objects, but their use on the micrometer scale is challenging.

In this thesis, a confocal microscopy setup (Nanofocus µsurf expert) is used for shape analysis. As this is an optical characterization technique, the lens surface is not damaged during the measurement. The sample is illuminated by a microscope objective, which also collects the light reflected back from the lens surface. The light is focused through a pinhole in the optical setup. This ensures that only light reflected from structures in the focal plane of the microscope objective reaches the sensor of the microscope. By moving the objective up and down in fine steps, the focal plane can be scanned over the whole lens surface. The signal from each position is recorded and then combined into a 3D height distribution. As the working distance of the microscope objective is 300 µm, this is the maximum height for a lens design which should be characterized by confocal microscopy. Additionally, the detectable slope angle of the lens surface is limited by the numerical aperture of the objective (Figure 2.10). The full illumination cone is shown in green, corresponding to the wavelength of the used light. The horizontal red lines mark the portion of the illumination cone which is reflected back into the objective, and the red dashed arrows mark the extreme rays at the border of this region. As the surface gets steeper, the amount of reflected light is gradually reduced, until only the ray at the

border of the illumination cone is directly reflected back into the objective. The maximum slope angle β is equal to the half-angle of the illumination cone. For an NA of 0.95, the maximum slope angle is 72°, which limits the measurable region of lenses with extreme curvature, e.g., a half-ball lens (see Chapter 4).

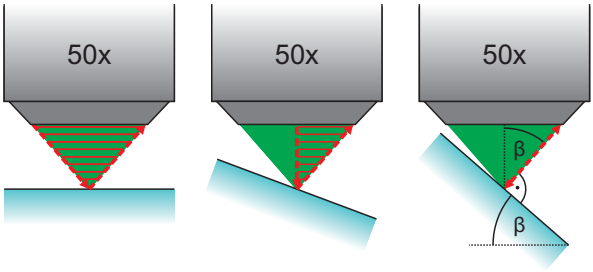

Figure 2.10. Slope angle limitation in confocal surface analysis. A flat surface with different slope angle is used as example (blue). The full illumination cone of light is shown in green. The portion of the cone covered by the red horizontal lines is reflected back into the objective and contributes to the measured signal. The dashed red arrows mark the extreme rays at the borders of this region. For increasing slope angles, the reflected light is reduced. The maximum slope angle β equals the maximum half-angle of the illumination cone.

2.4 NANOSCRIBE QUANTUM X

As a next step towards the industrial use of 2PP 3D printing machines, the new Nanoscribe Quantum X microfabrication system was released in 2020. While the working principle and basic components are similar to the Photonic Professional GT system, there are some important improvements. In analogy to Figure 2.7, an overview of the main components can be seen in Figure 2.11. In contrast to the PPGT, the orientation of focusing objective and substrate is reversed, resembling a standard microscope with the objective above the sample. Furthermore, the objective is fixed and can no longer be moved along the z-axis. The laser beam can still be scanned across the substrate in the xy-plane by two galvo mirrors. The substrate is mounted on a single translation stage which can move in all three directions.

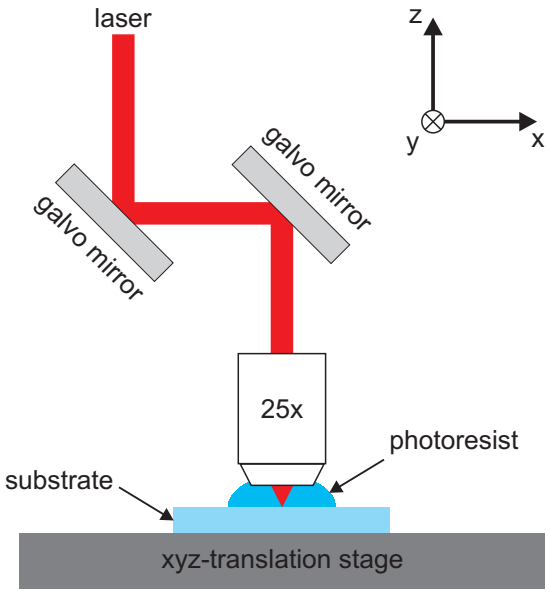

Figure 2.11. Schematic of the main components of the Nanoscribe Quantum X system. Compared to the Nanoscribe PPGT, the geometry is flipped upside-down and there is only a single translation stage which can move the substrate in all three dimensions. The objective is no longer movable.

The Quantum X supports two different printing modes. First, there is the classical 3D printing mode, which is basically identical to the printing process on the PPGT. The software for STL file conversion is now called DescribeX. In addition, there is a completely new printing mode called two-photon grayscale lithography (2GL). In this mode 2.5D structures, particularly lenses, can be fabricated with unprecedented surface quality while maintaining a fast printing speed. This is enabled by choosing a comparably large slicing distance in order to make use of the full polymerization volume of the voxel, as discussed earlier in this chapter. The superior surface quality and the removal of the staircasing effect are achieved by a variation of the voxel size close to the lens surface, in order to exactly match the designed shape. The voxel size variation is realized by carefully characterizing the influence of the laser power on the voxel size. During the printing preparations, a 3D model is no longer required. Instead, a grayscale image in PNG format is processed by the new Nanoscribe software GrayscribeX, which converts the grayscale values into a height distribution and successively into slices

and hatching lines. The important parameters are the size of the PNG image in the x- and y-direction and the maximum height of the structure. As grayscale images simply consist of values between 0 and 1 for each pixel, the software assigns a height of 0 µm to pixels with a grayscale value of 0 and the specified maximum height of the lens to the grayscale value 1. The grayscale images can be prepared in various ways. For aspheric lenses, the use of MATLAB was found to be convenient, as it is able to process formulas and variables and can directly save data as PNG files. The resolution of the image is chosen such that 1 pixel has the size of $0.2 \times 0.2\,\mu m^2$. The grayscale values are saved with a bit depth of 16 bit. Figure 2.12 shows the classical 3D model of a spherical lens, the corresponding surface profile and also the grayscale image used for 2GL printing. The grayscale image in Figure 2.12c has a size of $440 \times 440\,\mu m^2$ (2200 × 2200 pixels). The border of the lens is clearly visible as a discrete intensity step, as we added a 10 µm thick base layer between the substrate and the curved lens surface.

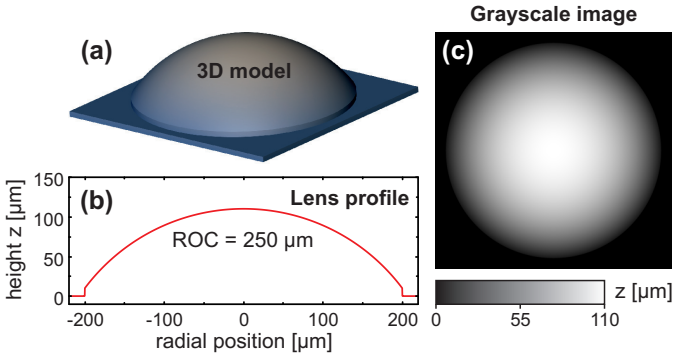

Figure 2.12. Preparation of a grayscale image for 2GL fabrication. **(a)** 3D model of the designed lens (not required for printing). **(b)** Profile of the spherical lens surface with a radius of curvature of 250 µm, a diameter of 400 µm, and 10 µm base thickness. **(c)** Grayscale image used for 2GL preparation. Grayscale values range from 0 to 1, representing heights between 0 µm and 110 µm.

Because grayscale images are used to define a printing project, there is exactly one z-value associated with each xy-coordinate in the image. Consequently, this limits the optical design freedom, as overhanging parts are not possible with this restriction. Therefore, this printing mode is also

called 2.5D fabrication, which is perfectly suited for rapidly printing large arrays of micro-lenses with a single curved surface onto a substrate. Using a combination of the classical 3D printing mode and the new 2GL mode, more complex multi-lens systems are also possible, as we will see in Chapter 5.

3

DOUBLET IMAGING SYSTEMS

Detailed studies of various 3D printed optical elements have been published before [66–69]. In context with the present work, especially the publication "Two-photon direct laser writing of ultracompact multi-lens objectives" by Gissibl et al. [66] is relevant, as it contains the ground-work for several goals and challenges throughout this thesis. In particular, the fabrication of multi-lens imaging objectives (Figure 3.1) was demonstrated there, and the influence of different numbers of optical surfaces was examined. The diameter of all investigated objectives was 100 µm, and they were fabricated using a printing objective with a magnification of 63x and a numerical aperture of 1.4, which is recommended for structures with a diameter < 200 µm. One of the main goals of this thesis was to increase the size of 3D printed optical elements, in order to make the fabrication technique compatible with other optical components. To enable diameters beyond 200 µm, a different focusing objective with a larger writing field had to be used and printing

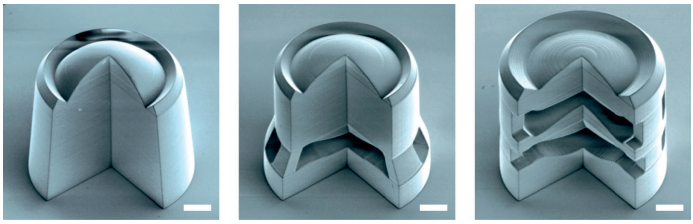

Figure 3.1. 3D printed singlet, doublet and triplet objective presented by Gissibl et al. in [66]. For better visibility of the individual lenses, only 270° of the objectives were printed. The scalebars are 20 µm wide. Reprinted by permission from Springer Nature Customer Service Centre GmbH: Springer Nature, Nature Photonics, "Two-photon direct laser writing of ultracompact multi-lens objectives," T. Gissibl et al., 2016.

parameters had to be adjusted. This chapter describes the optical design, the fabrication and the optimization of dual-lens imaging objectives with four aspheric free-form surfaces and diameters around 500 µm. Furthermore, the direct fabrication of such objectives on image conducting fibers and camera sensors will be discussed, and finally an approach for the reduction of the printing duration is proposed.

The research on the doublet objectives described in this chapter was a close collaboration with the Institute for Applied Optics at the University of Stuttgart, where Dr. Simon Thiele was responsible for the optical design and the CAD models, while the fabrication, confocal surface measurements and characterization of the imaging properties were carried out at the 4th Physics Institute.

3.1 OPTICAL DESIGN AND 3D MODELS

Before starting the optical design process for a certain objective, the boundary conditions have to be estimated. For 3D printed optics, there are some physical limitations induced by the utilized writing objective of the Nanoscribe PPGT system, which was used for the fabrication of the optical elements presented in this chapter. The standard objective for bigger structures > 200 µm has a magnification of 25x, a working distance of 370 µm, a numerical aperture of 0.8 and a theoretical maximum writing field diameter of 800 µm. As we want to print several identical objectives in close vicinity, the height of our printed structures is limited by the working distance. Therefore, another printing objective (Zeiss LD LCI Plan-Apochromat 25x/0.8 Imm Korr DIC M27) was used. It has the same magnification and numerical aperture as the standard Nanoscribe 25x objective, but an increased working distance of 780 µm, which defines the limit for the total height of the printed objectives as discussed in Subsection 2.3.3. The theoretical maximum writing field diameter is 720 µm, however, it is usually not recommended to use the full writing field, as the quality of the printed object might deteriorate towards the outer regions. Furthermore, one of the key applications of such 3D printed dual-lens objectives is the direct fabrication on image conducting fibers in order to build compact, high-quality endoscopes. While the fibers are in principal available with different fixed diameters, fibers with 500 µm diameter are of particular interest, as they can be used for specific medical applications, e.g., inspection of the salivary ducts [3] or the root canals of teeth [2]. Three different objective layouts are depicted in Figure 3.2a - 3.2c.

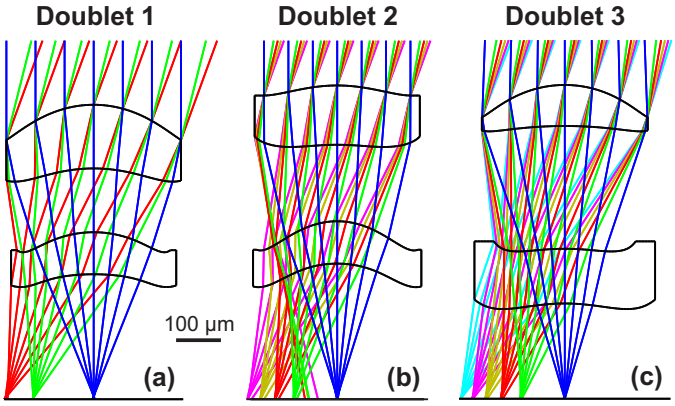

(d)	Doublet 1	Doublet 2	Doublet 3
Focal length	543 µm	550 µm	570 µm
f#	1.36	1.66	1.7
Object distance	infinity	infinity	5 mm
Height	657 µm	700 µm	700 µm
Image diameter	400 µm	400 µm	509 µm

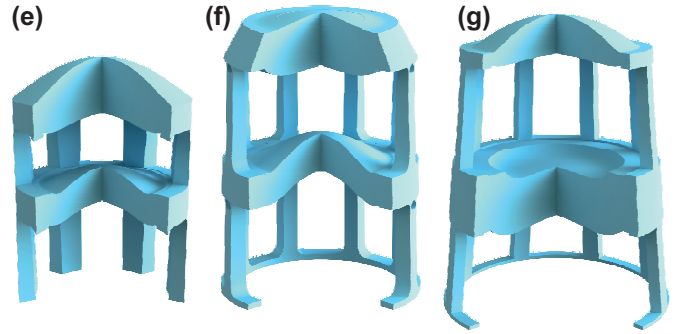

Figure 3.2. Optical design parameters and CAD models of 3D printed doublet objectives. **(a) - (c)** Layout of different optical designs for imaging doublet objectives. **(d)** Optical and geometrical parameters. **(e) - (g)** 3D models of the objectives, including supporting structures.

All objectives consist of two lenses with four aspheric free-form surfaces in total, which enables the correction of higher order optical aberrations. The field of view is 40° for all designs. The detailed optical and geometric parameters for each objective are listed in the table in Figure 3.2d. While doublet 1 and 2 are designed for imaging objects at infinite distance, doublet 3 is designed for a finite object distance of 5 mm. For characterization purposes the objectives are printed on standard flat glass substrates, where the image plane of the design is coincident with the substrate surface. To ensure the correct distance between the bottom lens and the substrate and also between the two lenses, the optical surfaces were transferred to a CAD software, and different supporting structures were added (Figure 3.2e - 3.2g). While the first objective contains only two refractive lenses, the other objectives also include diffractive optical elements on the upper surface of the top lens, which reduce chromatic aberrations.

All objectives are higher than 300 µm, which is the range of motion of the high-accuracy piezo stage in z-direction. Therefore, the objectives were split into multiple segments in z-direction and a combined movement of the piezo stage and the writing objective (using the microscope z-drive) was used. The lower lens surfaces in doublet 3 include hanging regions, which are difficult to fabricate, marked in red in Figure 3.3. As their lowest layer is not connected to the already printed supporting structures, it might not stay where it is printed, but rather move in the surrounding liquid photoresist. To circumvent this, the part of the lens situated directly above the curved

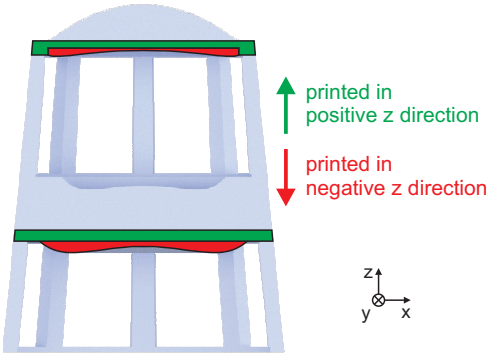

Figure 3.3. Printing strategy for hanging parts in doublet objectives. In both lenses in the cross-section of doublet 3, the flat green region was printed first in positive z-direction, followed by the red part where the laser was focused through the green part and moved layer-by-layer in negative z-direction.

lens surface (marked in green) was printed beforehand. The laser is then focused through this 5 µm thick flat plate and the red lens surface is printed by moving layer-by-layer in negative z-direction. We assume the influence of the additional polymerized structure on the laser beam propagation to be negligible or at least small enough to be compensated by the standard optimization procedure introduced in the next section.

3.2 SHAPE OPTIMIZATION

When the photoresist is polymerized by 2PP, the hardened structure has a slightly smaller volume than the liquid resist, which is effectively a shrinking process and is highly dependent on the geometry of the printed object. While shrinking might be an isotropic effect for symmetric objects, it becomes highly anisotropic for complex structures and therefore introduces local stress and deformations, resulting in shape deviations of optically active surfaces from the design. For smaller lenses (diameter < 100 µm), the absolute shape deviations cannot be measured easily, as they are too small and often do not even deteriorate the functionality of the optical element. For bigger lenses, shape deviations can be on the order of several micrometers, which can be measured and compensated, in order to improve the imaging quality.

A typical sample used for shape optimization is shown in Figure 3.4a. In the lower left corner, five complete doublet objectives (design 2) can be seen, which were used for imaging experiments and surface measurements. However, only the top surface of the upper lens can be measured by our confocal microscopy setup. Therefore, we additionally printed the lower and upper part of the objective separately, visible in the upper right corner. This also enabled the surface characterization of the top surface of the lower lens. As the individually printed lower and upper parts now lack the respective other half of the objective, the conditions during the printing process might be slightly different than for the printing of the entire objective. However, both parts of the objective are only connected by eight comparably thin pillars, therefore we expect that any interaction between the two parts in terms of shape deformations will mostly happen inside the connecting pillars and not in the comparably massive lenses.

Accessing the bottom surfaces of the lenses was less straightforward. While it would be possible to print the lenses upside-down, this would be a major change in the printing process and would most likely lead to surface deformations which differ from the conditions in the complete objectives

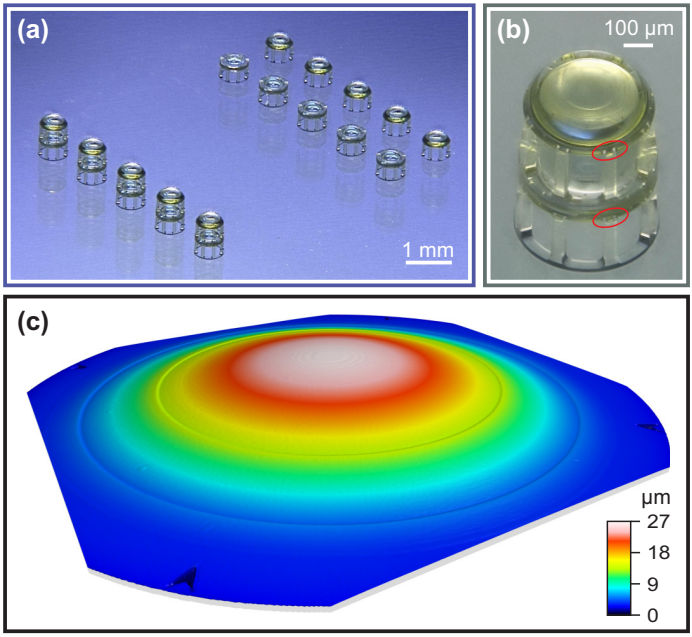

Figure 3.4. Sample for shape optimization of doublet objectives. **(a)** Sample overview. The full objective and the lower and upper parts are printed five times each. **(b)** Full objective with predetermined breaking points marked in red. **(c)** Confocal microscopy image of the top surface of the upper lens of a doublet objective. The visible discrete steps are part of the diffractive optical element for chromatic aberration control.

printed in the original direction. Instead, the lenses had to be flipped upside-down by carefully attaching adhesive tape to the top surfaces, which was then slowly peeled of with the lenses sticking on it and the supporting pillars remaining on the substrate. This procedure usually worked well, but occasionally some of the pillars would stick to the lens rather than to the substrate and therefore had to be removed manually under a microscope using the fine tip of a syringe needle. To avoid this, the connection between the pillars and the lenses was weakened by introducing predetermined breaking points in the 3D model. They are marked in red in the picture of a complete objective in Figure 3.4b. A confocal surface measurement of the top surface of the upper lens is shown in Figure 3.4c. To facilitate profile extraction, several arrowhead-shaped markers were added to the flat region around the curved lens surface. Here, the steps of the diffractive optical

element can be distinguished, which were incorporated into the lens for the reduction of chromatic aberrations.

The measured shape deviations of all four lens surfaces of an optimized and unoptimized doublet objective are depicted in Figure 3.5. We verified the rotational symmetry of the lenses by comparing profiles through the center of the lens, extracted along different directions. For the shape optimization, two perpendicular profiles were extracted from each surface measurement, and several lenses were characterized to monitor the repeatability of the printing process. The designed lens shape was subtracted from the measurements and the resulting deviations are plotted in black. A polynomial fitting function (red) was used to obtain an analytical expression for the shape deviation, which was then added to the original design for the next optimization iteration. The left column (Figure 3.5a - 3.5d) shows the shape deviations of the original design without any optimization, and the right column (Figure 3.5e - 3.5h) represents the optimized design. The lens surface under consideration is marked in blue in the optical design sketch in the upper right corner of each row. Three iterations were used for optimization, except for the bottom surface of the lower lens. Here, the surface characterization of the original design was not possible, as the removal procedure with adhesive tape did not work out well. In the first optimization step this surface was printed with the original design and the data shown in Figure 3.5d was obtained from this sample. Thus, surface 4 went through two optimization iterations. In general, the deviations of the optimized surfaces are much flatter than their unoptimized counterparts. Particularly the upper lens (surfaces 1 and 2) match the design nearly perfect after optimization. Those surfaces are not curved as strongly as the surfaces 3 and 4, which is probably the reason for the smaller shape deviation. But compared to the original design, the shape deviation of surfaces 3 and 4 have also been significantly reduced.

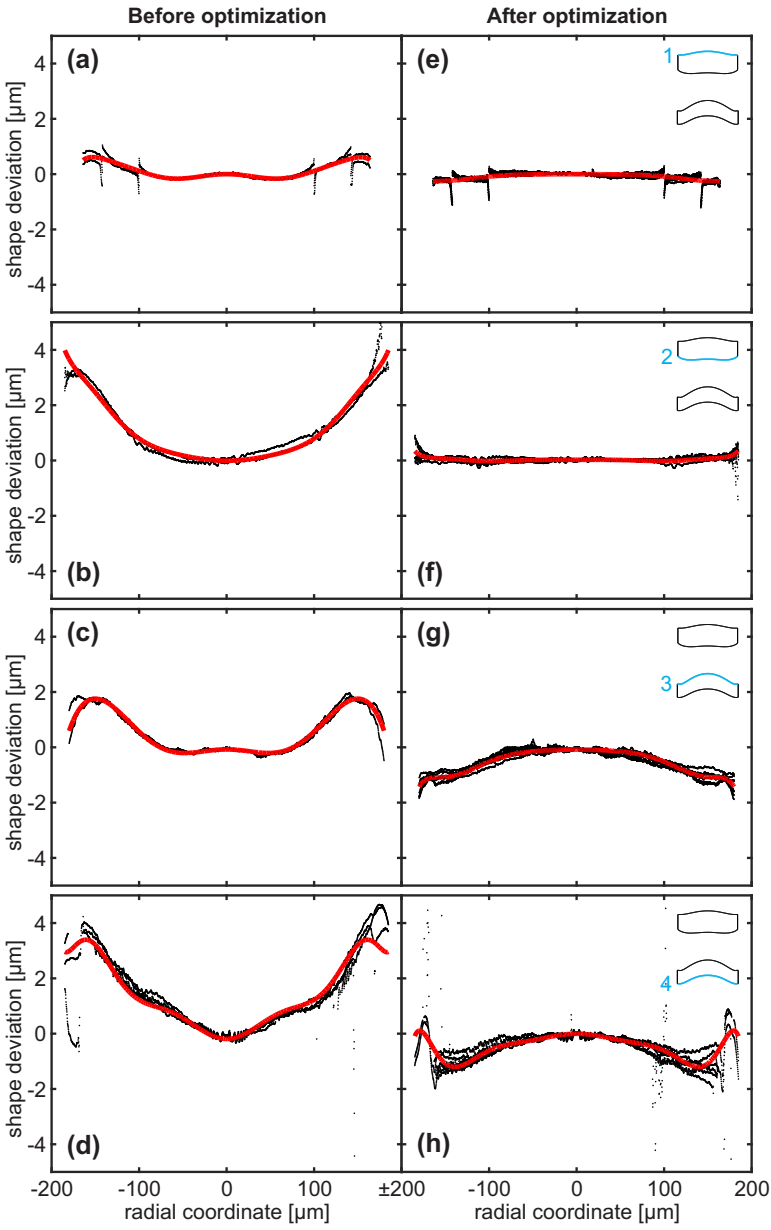

Figure 3.5. Shape deviations and optimization of lens surfaces in doublet objectives. **(a) - (d)** Shape deviations of the individual lens surfaces, printed without any optimization. Red curves are polynomial functions fitted to the black data, which were used for the iterative optimization. **(e) - (h)** Shape deviations after optimization.

The influence of the optimization process on the imaging quality of the objectives was experimentally analyzed by imaging a USAF 1951 resolution test target positioned at different distances d in front of the objective (Figure 3.6). The images in the left column (Figure 3.6a - 3.6c) were taken with an unoptimized objective, and the right column (Figure 3.6d - 3.6f) was imaged by an optimized objective. The superior imaging quality of the optimized objective is clearly visible when comparing Figures 3.6a and 3.6d, where the test target was placed $d = 7.2\,\text{mm}$ in front of the objective. For the unoptimized objective, the lines of the test target appear blurred, particularly elements 5 and 6 of group 2. In the image generated by the optimized objective the edges of the lines look much sharper. When the target is positioned closer ($d = 2.3\,\text{mm}$) to the objective, groups 4 and 5 can be resolved (Figures 3.6b and 3.6e). Again, the lines imaged by the unoptimized objective appear blurred, especially when looking at the elements of group 6 in the center of the image, the difference in imaging quality is evident. In Figures 3.6c and 3.6f the target was positioned even closer to the objective to resolve even smaller structures. All elements of groups 6 and 7 can be distinguished for the optimized objective, while the image is blurry for the unoptimized objective. The resolution limit of the optimized objective lies within group 8 in Figure 3.6f, where the dark and bright lines of elements 1 and 2 can be distinguished with the unaided eye. For smaller elements this gets increasingly difficult. The elements of group 9 can no longer be distinguished.

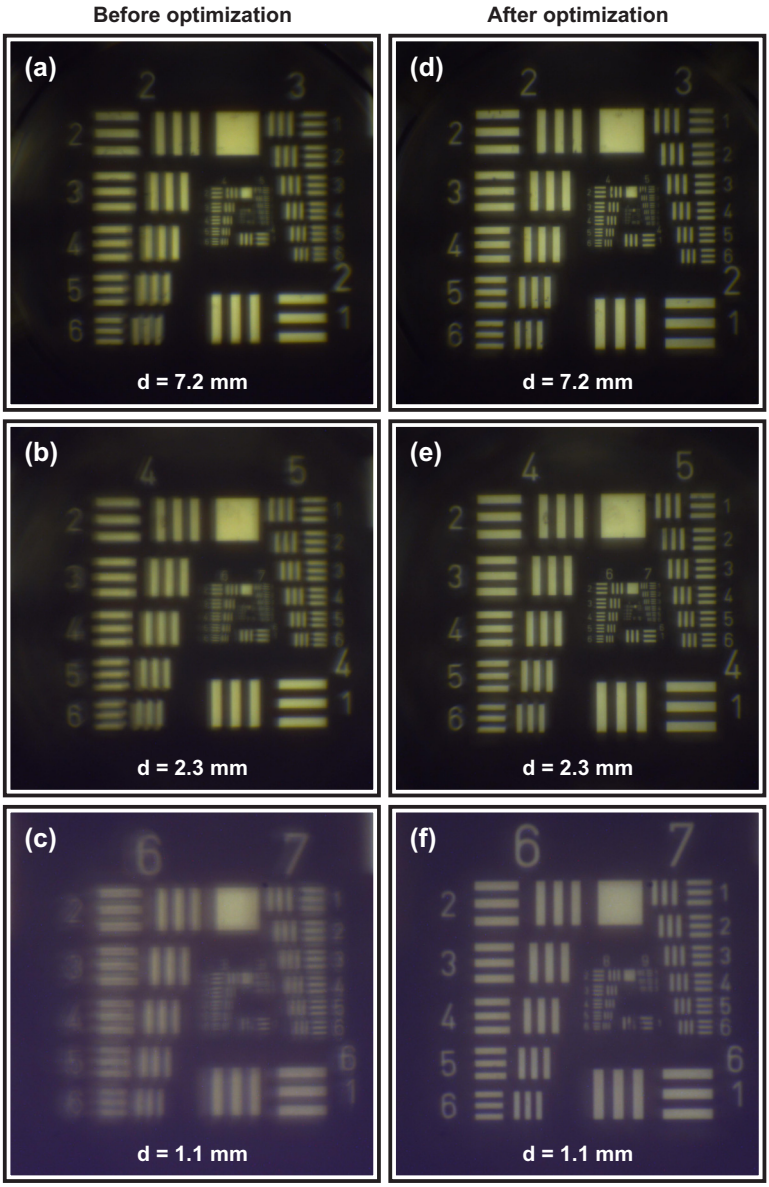

Figure 3.6. Imaging quality of optimized and unoptimized doublet objectives. **(a)** - **(c)** USAF 1951 resolution test target imaged by a doublet objective before optimization. For smaller distances d between target and objective, smaller elements of the target (higher group number) can be distinguished. **(d)** - **(f)** Resolution test target imaged by an optimized doublet objective.

3.3 PRINTING ON IMAGING FIBERS

One of the most promising applications for 3D printed optical elements with sub-millimeter size is the fabrication of endoscopic devices to access very narrow openings, both in medical diagnosis and in industry for quality monitoring. In order to bring the optical information from the tip of the endoscope to the observer, state-of-the-art endoscopes often make use of image conducting fibers. Unlike standard single-mode glass fibers they have not only one, but multiple fiber cores which effectively act as pixels on the fiber tip. As the arrangement of the fiber cores is maintained throughout the length of the fiber, an image projected onto one end of the fiber is guided all the way to the other end and can be extracted there. The fibers come with a black polymer coating, which keeps stray light from entering the fiber and also gives a certain degree of mechanical flexibility to the fiber (Figure 3.7a). Image conducting fibers are available with different numbers of fiber cores, which determines the resolution of the transmitted image. Because the diameter of a single fiber core is fixed (~3 µm), the number of cores also determines the total fiber diameter, and thus also the flexibility of the fiber. The end of a fiber with a total diameter of 580 µm (black polymer coating) is depicted in Figure 3.7b. The glass part has a diameter of 500 µm, of which an area with 460 µm diameter contains the fiber cores and is effectively used for image transmission. This section describes how optical elements for different endoscopic applications can be 3D printed directly on the end of such an image conducting fiber.

3.3.1 *Doublet objective*

The most straightforward approach to building an endoscopic device using an image conducting fiber is printing an imaging system onto one fiber end. In state-of-the-art endoscopes with sub-millimeter size, the imaging system often consists of a single gradient-index lens (GRIN lens), which is shaped like a glass cylinder and matches the diameter of the fiber. The refractive index inside the cylinder changes from the center towards the outer part. The radial dependence of the refractive index and the length of the rod-lens can be tailored to fulfill the requirements for a specific imaging task. Generally, the choice for commercial optical glass elements with diameters < 1 mm is limited, and apart from gradient-index type lenses, there are mostly simple spherical ball or half-ball lenses readily available.

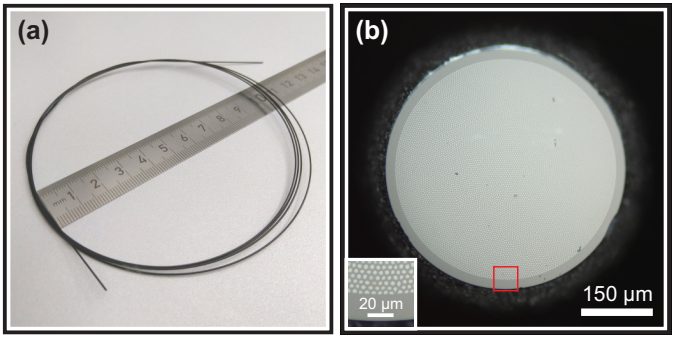

Figure 3.7. Image conducting fiber for semi-flexible endoscopic devices. **(a)** Wound up image conducting fiber with a length of 1.5 m. **(b)** Microscope image of fiber end. The diameter of the image conducting area containing the fiber cores is 460 µm and consists of ~10,000 fiber cores. The inset shows a magnified image of the area marked by the red square, which has a size of 50 × 50 µm². Fibers were kindly provided by Karl Storz SE & Co.KG.

In this size regime, 3D printed multi-lens systems containing aspheric free-form surfaces are an interesting alternative. As the fiber end where the objective will be printed on should be as clean as possible, we cleave the fibers directly before 3D printing, using a Vytran LDC-400 large diameter fiber cleaver. Before the cleaving step, the black polymer coating has to be removed, which is achieved by burning it and removing the remaining small particles using acetone and isopropyl alcohol. While real endoscopes can have lengths of several decimeters, we used mainly shorter pieces of 10 - 20 cm length for our 3D printing tests.

In the 3D printer, the fiber is mounted in a special fiber holder, effectively placing the end of the fiber at the same position where a standard glass substrate would be. All structures in this section are printed using a 25x focusing objective and IP-S photoresist. First, a 20x objective designed for use in air is used to determine the exact location of the fiber, which can vary due to the mechanical design of the fiber holder. Once the fiber can be seen via the system camera, the actual 25x focusing objective is mounted and the photoresist is dispensed on the front lens of the objective. The fiber-photoresist interface has to be located manually, as the implemented interface-finding algorithm is not compatible with fibers. To find the interface and the center of the fiber, the laser is switched on at a power level below the polymerization threshold. The interface will generate a reflection depending on the focal position of the laser, the reflected laser spot has

minimum size if the focus is exactly at the interface. For centering, the fiber is moved to an arbitrary position where the focused laser hits the boundary of the area containing the fiber cores. The coordinates are noted, and the fiber is moved along the x-direction until the laser hits the boundary on the other side of the core-containing region. Again the coordinates are noted, the mean x-values give the x-coordinate of the fiber center. The fiber is then moved to this x-position and the procedure is repeated for the y-direction.

Figure 3.8a shows the side-view of an image conducting fiber with 500 µm diameter and the previously introduced doublet objective 3 printed onto the fiber end. The image plane of the objective is designed to match the surface of the fiber. A tilted close-up view of the objective is depicted in Figure 3.8b. At the bottom of the objective, a conic supporting structure increases the connection between fiber and objective, as the pillars supporting the lower lens would otherwise be printed outside of the fiber end. To test the imaging of this fiber-objective system, a USAF 1951 resolution test target was placed in front of the objective and the back end of the fiber is monitored using a microscope. The overall imaging quality is good without any visible image distortion. The limitation of the system can be seen when taking a closer look at the individual fiber cores for smaller elements of the test target. In element 1 of group 2, the bright and dark lines are each 125 µm wide and can be clearly distinguished from each other, as every line covers several rows of fiber cores. Elements 1 and 2 of group 3 are also distinguishable, however, from element 3 of group 3 on this gets increasingly challenging, as one line of the test target is imaged on a single line (or even less) of fiber cores. To test color imaging, doublet design 1 was printed onto another fiber (Figure 3.8d) and a color test target was positioned $d = 20$ mm in front of the objective. The colors in the image (Figure 3.8e) are reproduced correctly, and the thin grid lines, which have a width well below 1 mm, are visible as well.

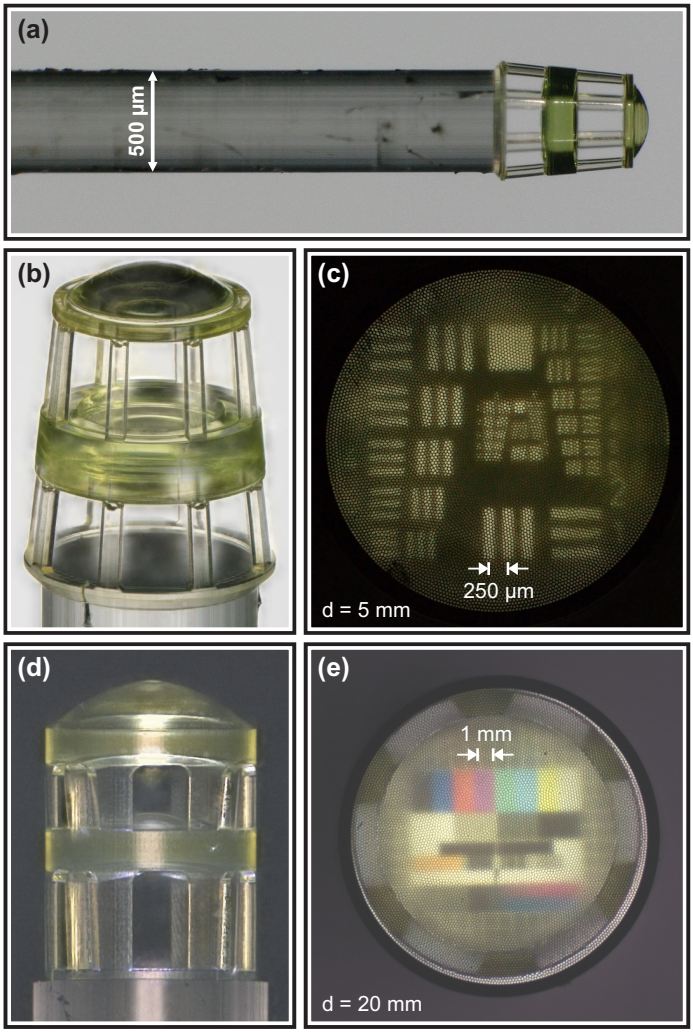

Figure 3.8. Doublet objctives printed on image conducting fiber bundles. **(a)** Image conducting fiber with doublet objective 3. **(b)** Close-up image of objective 3 on fiber end. **(c)** Image of USAF 1951 resolution test target placed $d = 5$ mm in front of the objective shown in **(b)**. The target is imaged by the objective on the front end of the fiber and can be viewed on the back end with a microscope. **(d)** Doublet objective 1 printed on image conducting fiber. **(e)** Image of color test target positioned $d = 20$ mm in front of the objective shown in **(d)**.

3.3.2 *Off-axis imaging*

In the fiber endoscope introduced in the previous section the direction of view was 0° with respect to the optical axis (which is going through the center of the fiber). For certain endoscopic tasks different viewing directions are required, e.g., in order to inspect the vascular walls of a blood vessel. This can be achieved by total internal reflection (TIR) at the inclined surface of a 3D printed prism on the fiber tip (Figure 3.9a). Light is emitted from the fiber cores with a numerical aperture of 0.35 with air as surrounding medium. The deflection mechanism for light coming from an exemplary fiber core is illustrated in the cross-section view of the system in Figure 3.9b. We assume that both the fiber and the printed prism have an identical refractive index of 1.5. The numerical aperture of the fiber is then reduced to 0.23, corresponding to a light cone with a full opening angle of 27°. Light rays in the cone will be reflected and transmitted at the prism surface depending on their angle of incidence. The two edge rays impinge on (and are also reflected from) the inclined prism surface under different angles $\alpha = 58.5°$ and $\beta = 31.5°$. As the angles of incidence for both rays are $\theta_1 = 90° - \alpha = 31.5°$ and $\theta_2 = 90° - \beta = 58.5°$, the upper ray undergoes TIR because the critical angle is $\theta_{TIR} = 41.8°$. The lower ray is partly transmitted through the prism, indicated by the red arrow. In general, a part of the light cone will meet the condition for total internal reflection and the remaining part will be transmitted to a certain degree. The working principle is verified by a simple experimental setup (Figure 3.9c), which images an object by a single lens onto one end of the fiber. The prism at the other end is positioned under the objective of a standard microscope, which is focused through the prism on the fiber end. As a first test, we illuminated the fiber end with an LED flashlight and observed the transmission along the fiber and through the prism (Figure 3.9d). Then, the setup from Figure 3.9c was used to successfully transmit images of a resolution test target (Figure 3.9e) and a printout of a portrait (Figure 3.9f).

To build an endoscope with a direction of view of 90°, an optical element has to be added to the prism, e.g., by printing a lens on the prism face which is perpendicular to the x-axis in Figure 3.9a. Fulfilling the necessary condition for total internal reflection, however, limits the optical design freedom here. If the shape of the reflecting surface of the prism is changed from planar to a more complex free-form shape, which can be incorporated in the optical design, this limitation can be lifted. Applying a highly reflective (metal) coating to the reflecting prism face also removes the requirement for

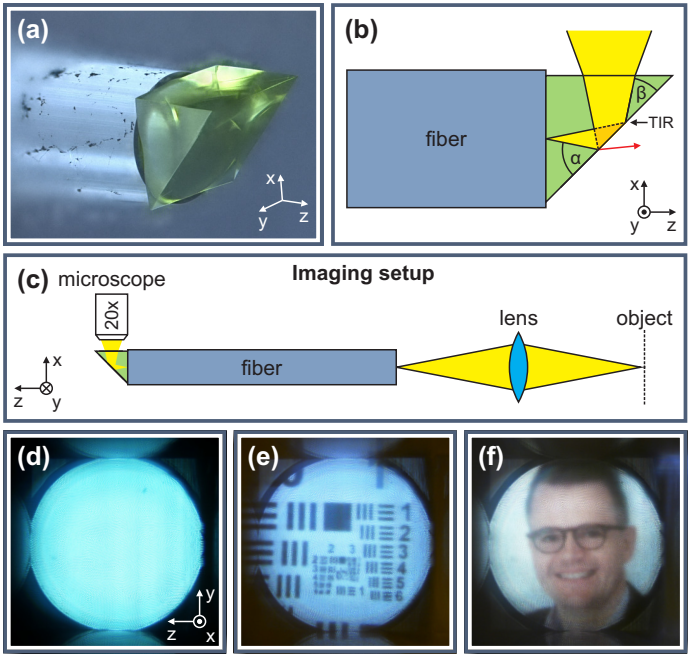

Figure 3.9. 3D printed prism on image conducting fiber. **(a)** Microscope image of fiber tip with printed prism. **(b)** Reflection of light coming from the image conducting fiber at the prism surface. **(c)** Test setup for image transmission through the fiber and the prism. **(d)** Light from an LED flashlight which is shined on the bare end of the fiber is transmitted by the prism and then collected by a microscope. **(e)** and **(f)** Resolution test target and portrait imaged by the setup shown in **(c)**.

TIR, at the cost of one additional processing step during sample fabrication. Following this approach, it becomes immediately clear that a solid prism is no longer needed if the change in viewing direction is achieved by conventional reflection from a highly reflective surface and not by TIR. Instead, a thin plate with an angle of 45° with respect to the z-axis will have the same effect. We realized this by printing the structure in Figure 3.10a on a new image conducting fiber. The geometry is in principle a hollow prism with a circular opening on one side, which is necessary to remove the liquid photoresist from the interior of the structure. After 3D printing, the inner surface of the inclined prism face was coated with aluminum using electron-beam assisted evaporation. Finally, a doublet objective was 3D printed on the prism face containing the opening. During the coating process the main part of the

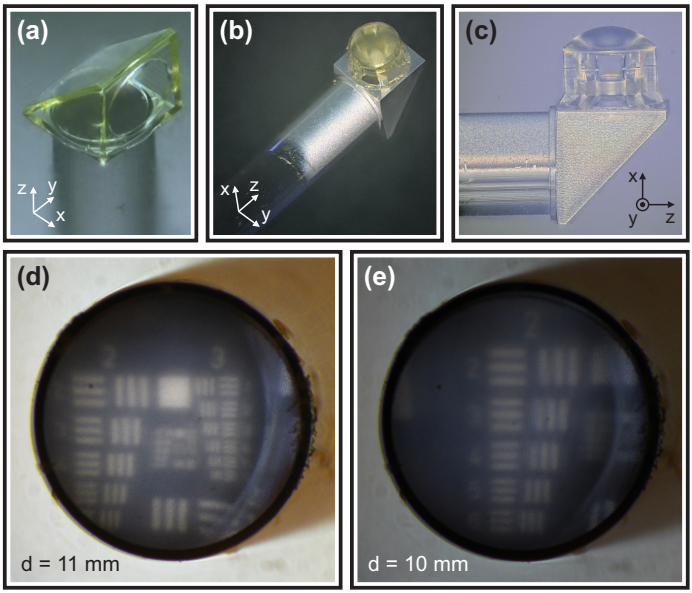

Figure 3.10. Mirror and doublet objective on image conducting fiber. **(a)** Hollow prism printed on image conducting fiber. **(b)** Tilted view of a doublet objective printed on the Al coated mirror structure. **(c)** Side-view of the mirror-objective combination. **(d)** Image of USAF 1951 resolution test target placed $d = 11$ mm in front of the objective on the front end of the fiber, viewed on the back end of the fiber by a microscope. **(e)** Image of resolution test target placed $d = 10$ mm in front of the objective.

fiber was shielded from the evaporation beam, however, a short part was still coated with aluminum (Figure 3.10b). A side view of the structure is depicted in Figure 3.10c. The focal plane of the objective is coincident with the fiber end. For the coating step and the subsequent 3D printing of the objective, the fiber had to be aligned precisely to avoid partially shading of the inner surface from the evaporation beam and to ensure a horizontal starting plane for 3D printing. This was achieved by looking at the open side of the prism with a microscope while the fiber was fixed in a rotation mount, which was adjusted such that all edges were in focus at the same time. While still mounted in the rotation mount, the fiber was then attached to a flat glass substrate by removable glue, resulting in the open side of the prism being parallel to the surface of the substrate. The substrate-fiber combination was then placed inside the evaporation chamber and in the 3D

printer, and the substrate was removed after successful fabrication of the objective. A setup similar to Figure 3.9c was used for imaging experiments. The resolution test target was placed in front of the printed objective and the back end of the fiber was viewed by a microscope and a conventional mirror, as the fiber was aligned horizontally. Figures 3.10d and 3.10e show the image of the test target for slightly different object distance d. Again, the limiting factor is the size of the single image conducting fiber cores. However, the overall contrast is not very high, which is attributed to a large amount of stray light from the comparably big 3D printed structures and the evaporated aluminum. Surrounding the objective and the hollow prism with a black shell should help to increase the imaging quality.

3.4 PRINTING ON CAMERA SENSORS

In order to make use of 3D printed micro-optics for different applications, it is often required to combine them with other (optical) devices, e.g., an image conducting fiber for endoscopy. For imaging systems with image diameters < 1 mm it becomes challenging to view the image with the unaided eye. Instead, the image can be magnified using additional optical components, or the image can be viewed on a screen where the image size can be increased. For this, the image has to be captured at some point by a camera sensor or similar system, which converts optical information to digital information. Combining 3D printed optics with different types of camera sensors is therefore an interesting approach. This section describes how to use such sensors as supporting substrate for 3D printing of optical elements and demonstrates the high imaging quality of the combined optical systems.

3.4.1 *Raspberry Pi camera sensor*

The sensor of the Raspberry Pi camera system was used to investigate the fabrication of micro-optics directly on the sensor surface. The actual CMOS chip inside the camera is a standard product and is installed in different variations in a wide range of sensor devices, therefore we assume that our fabrication method will work with other sensors as well. Using the Raspberry Pi camera sensor has certain advantages compared to other products. It is comparably cheap and the documentation for the Raspberry Pi environment is very detailed, facilitating the testing and evaluation of the 3D printed components on the chip. An image of such a camera module is shown in

Figure 3.11. As this is a commercial product designed to function as a camera, it is equipped with a standard imaging lens located in the center of the round black plastic part, which is connected to the black housing by a thread in order to change the focal position. To access the CMOS chip, the housing has to be removed using a razor blade. During this process it is crucial to avoid damaging the electronic parts arranged around the sensor by inserting the blade too far. The CMOS area used for imaging has a size of $3.7 \times 2.7\,\mathrm{mm}^2$ and square pixels of $1.4 \times 1.4\,\mu\mathrm{m}^2$. A microscope image of the sensor surface with the bayer color filter can be seen in the inset.

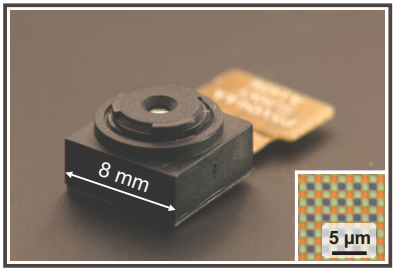

Figure 3.11. Raspberry Pi camera module. The black plastic block holding the standard lens has to be removed before 3D printing on the underlying sensor surface.

The doublet imaging objectives introduced previously were printed on Raspberry Pi camera sensors. Figure 3.12 exemplary shows the 3D model of doublet 3. Different colors correspond to different laser power settings during fabrication. Preliminary experiments showed that the polymerization behavior close to the sensor surface is different from the standard glass coverslips, which are usually used as supporting substrate. Glass and sensor surface have different reflecting and absorbing properties. Reflections from the sensor are much stronger than reflections from a glass surface, which can be easily seen by the unaided eye. As the sensors are not transparent, the incoming transmitted light has to be absorbed at a certain point. While absorption can lead to local heating of the sensor and the photoresist on top, the combined reflected light and the normal incoming laser beam result in an increased dose, which can in turn trigger micro-explosions in the resist [59]. Both effects induce inhomogenities in the polymerization process, and especially the micro-explosions can weaken the connection between the

printed structure and the sensor surface. Therefore, the printing parameters have to be adapted to those circumstances. It was found that reducing the laser power in the region close to the surface can solve this issue. The red part in Figure 3.12 is printed with only 5% laser power, for the green part the power is increased to 35%, which is half the regular power used for the remaining structure (70%, yellow). The layers with reduced power each have a thickness of 15 µm. For the lowest layer (red), the scan speed was also reduced to 10,000 µm/s, compared to 50,000 µm/s used for the remaining parts.

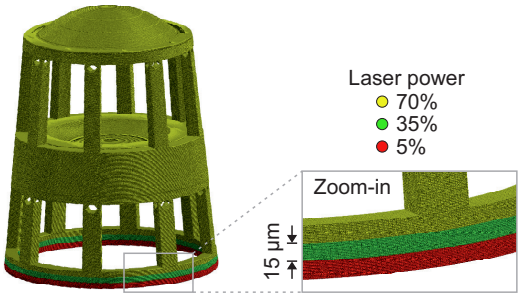

Figure 3.12. 3D model of doublet objective designed for printing on a Raspberry Pi camera sensor. At the bottom, two layers with 15 µm thickness are printed with reduced laser power to avoid micro-explosions due to excessive laser intensity. For the lowest layer, the scan speed is also reduced.

A triangular array of six doublet objectives (doublet 3) was printed on a sensor using the adaptive laser power settings. While the implemented interface finding algorithm works, the exact position of the interface might differ slightly from the perfect position of the printed objective's focal plane, as the CMOS pixels are covered by a bayer color filter and possibly also another protective layer. Therefore, the position of the focal plane was slightly varied among the six printed objectives by adjusting the space between sensor and lower lens. Figure 3.13a shows the camera chip with the printed objectives placed next to a ruler and a coin for size comparison. The golden bonding wires and electronic components surrounding the sensor area are not damaged by the chemicals used for developing, however, ultrasound treatment was avoided as it might destroy the bonding wire connections.

The imaging quality of the doublet objectives on the sensor was determined by connecting the chip to a Raspberry Pi computer, using a software tool which can read out the CMOS pixels. In Figure 3.13b the signal from the sensor area under one of the printed objectives can be seen. The image shows a USAF 1951 test target positioned ~5 mm in front of the sensor. The groups 3, 4 and 5 are shown. The purple ring around the actual image is the area where the polymerized photoresist is in contact with the sensor surface. The inner diameter of the ring is 509 µm and includes ~104,000 pixels. Groups 4

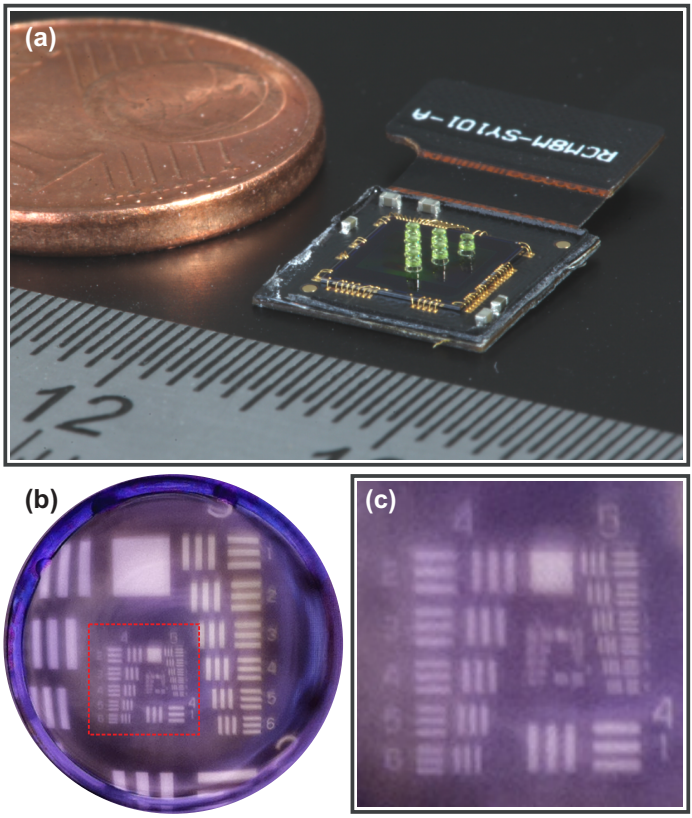

Figure 3.13. Imaging with Raspberry Pi camera sensor and doublet design 3. **(a)** Array of doublet objectives printed on a Raspberry Pi camera sensor. **(b)** Image of USAF 1951 resolution test target positioned ~5 mm in front of the sensor. The image diameter is 509 µm. **(c)** Magnified image of the area marked by the dashed red square in **(b)**.

and 5 (marked by the red dashed square) are depicted in a magnified image in Figure 3.13c. All elements of group 4 can be distinguished, as well as the elements 1 and 2 of group 5. The width of one line in element 2 of group 5 is only 14 µm.

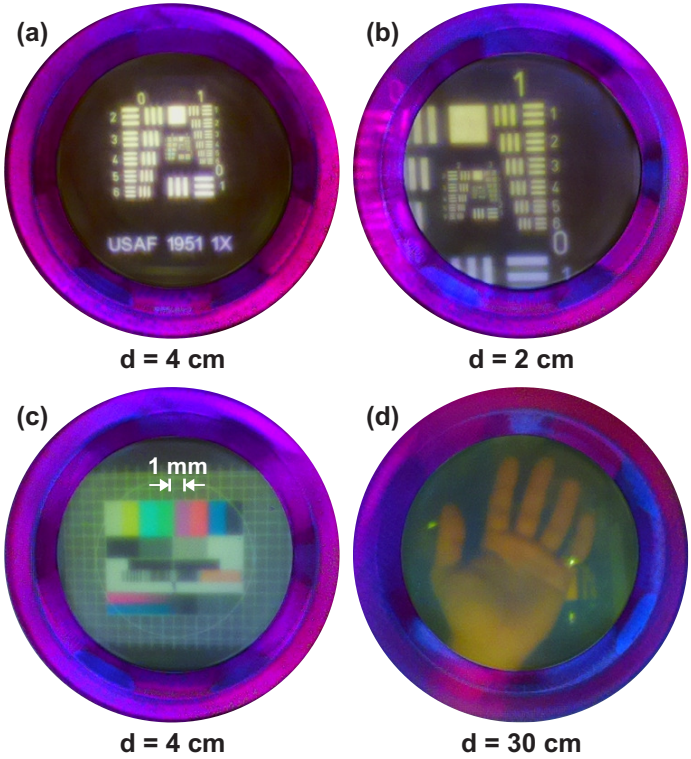

Figure 3.14. Imaging test of doublet design 1 printed on a Raspberry Pi camera sensor. **(a)** and **(b)** Images of USAF 1951 resolution test target at different object distances d. **(c)** Image of a typical color test target. **(d)** Image of a human hand.

To investigate the imaging quality for larger distances between camera sensor and object, the doublet design 1 was printed on another Raspberry Pi camera sensor, as this objective is designed for infinite object distance. In Figures 3.14a and 3.14b images of a USAF 1951 resolution test target positioned at a distance $d = 2$ cm and $d = 4$ cm in front of the sensor are depicted. The

inner diameter of the purple ring is 373 µm and includes ~56,000 pixels. The bright and dark lines of element 2 of group 1 can be distinguished for $d = 4$ cm in Figure 3.14a, corresponding to the width of a single line of 222.72 µm. When the target is moved closer (Figure 3.14b, $d = 2$ cm), element 2 from group 2 can be resolved. Here, single lines are 111.36 µm wide. The resolution test target was illuminated from the back by an LED panel covering a wide angular range. Figure 3.14c shows a color test image printed on transparent foil and illuminated in similar fashion. The different colors can be clearly distinguished and the white grid lines, which have a width well below 1 mm, are also imaged without significant image distortion. For a more application-oriented demonstration Figure 3.14d shows the image of a hand positioned at a distance of $d = 30$ cm in front of the sensor. This illustrates that such combined optical systems are well-suited for tasks like gesture recognition.

3.4.2 *Distal chip endoscopic sensor*

In the endoscopic devices discussed before, miniaturization is achieved by using a thin image conducting fiber and a small 3D printed objective, as those are the parts which are actually inserted into small, hardly accessible openings. At the end of the fiber the image can either by magnified by other optical components and then viewed directly by the inspecting person, or it can be focused onto a camera sensor to be viewed on a large screen. In both cases, the components used to bring the image from the end of the fiber to the human eye are not restricted by any size limitations. As an alternative approach, the image created by the 3D printed objective can be directly focused on a camera sensor, which is located close to the objective and therefore needs to be small enough to be inserted into the space under examination. This way, only a thin cable is required to transfer the image data to the outside. Such endoscopic systems are called distal chip systems. A standard distal chip system is depicted in Figure 3.15a. Here, the optical element is a commonly used GRIN rod-lens, which is attached to a glass sheet covering the actual sensor. Figure 3.15b shows a distal chip system with a 3D printed objective. As this was only a feasibility study on a non-functional dummy sensor, a model of an existing doublet objective (design 1) was scaled up to a diameter of 700 µm and the length of the supporting structures was adjusted to bring the focal plane to the sensor surface. Furthermore, hatching and slicing distances of 1 µm were used in order to reduce the printing duration.

While this approach in principle works, it was not developed further in the course of the thesis, as the perfect alignment of the distal chip system inside the 3D printer is challenging and the solution using image conducting fibers is in general much more convenient.

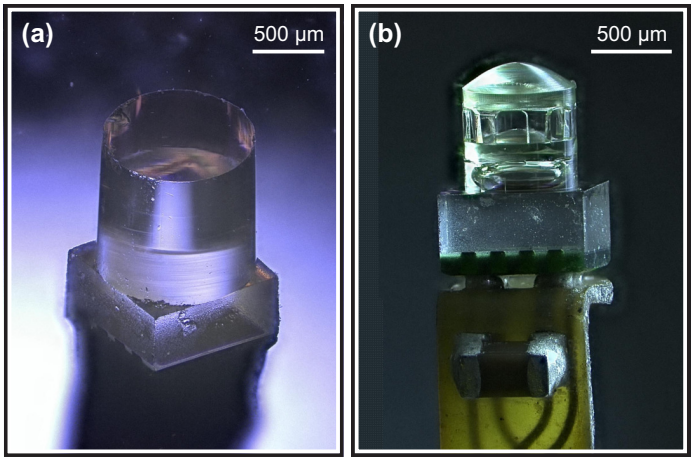

Figure 3.15. Distal chip endoscopic devices. **(a)** Endoscopic device with standard GRIN lens objective. **(b)** Endoscopic device with 3D printed doublet objective. Distal chip sensors were kindly provided by Karl Storz SE & Co.KG.

3.5 WRITING TIME REDUCTION BY CORE-SHELL WRITING

The slice-by-slice fabrication of our two-photon polymerization based 3D printing approach results in step-like surface shapes where a smooth curved shape was originally designed (Figure 3.16a). By increasing the number of slices into which an object is divided (by choosing a smaller slicing distance), the deviation from the design can be reduced, at the cost of a prolonged printing duration (Figure 3.16b). This is acceptable for structures which are only fabricated in small quantities, which is often the case for samples made for scientific purposes. For large-scale manufacturing, e.g., when the printed objects should be used in commercial devices, the printing duration is directly linked to the economical success of the product, and should therefore be as

short as possible. The most efficient way to polymerize a given volume is to choose the slicing distance equal to the actual physical thickness of the slices, which depends on the size of the voxel. This means that subsequent slices do not overlap at all. If the overlap between slices is increased by making the slicing distance smaller, the shape deviations are decreased at the cost of prolonged printing time. A two-step fabrication process where the lens is first printed with coarse slicing and then smoothed by printing an overlapping shell with fine slicing can reduce the printing duration while keeping the shape deviations low. The different slicing distances are depicted in Figure 3.16c. The dashed parts illustrate regions where the coarsely sliced core and the shell with fine slicing overlap. In Figure 3.16d a 3D model of a spherical lens also shows the differently sliced parts. For the first printing step, the normal 3D model of the full lens, consisting of both the light and dark blue parts in Figure 3.16d is used. For the shell, we use only the dark blue part, which is 5 µm thick. Both parts are processed separately by the standard Nanoscribe software DeScribe to generate the actual laser trajectories with different slicing distance.

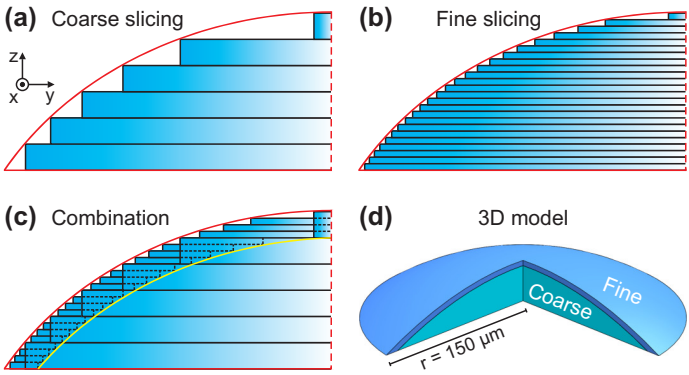

FIGURE 3.16. Slicing strategy for the core-shell printing mode. **(a)** and **(b)** Comparison of shape deviations of a curved surface (red) caused by slice-by-slice fabrication. The coarse slicing in **(a)** results in larger deviations than the fine slicing in **(b)**. **(c)** Combination of a coarsely sliced core and a shell with fine slicing results in good surface quality and a reduced printing duration. The yellow curve marks the inner boundary of the shell. **(d)** 3D model illustrating the regions with coarse and fine slicing.

To further increase the printing speed, the hatching distance can also be changed for the first part with coarse slicing. Finer hatching is required only for the shell, which contains the actual lens surface, as the hatching distance influences the surface roughness and therefore the optical quality. In Figure 3.17a a slice of the coarse part is shown. The hatching distance is chosen such that adjacent voxel lines still overlap, forming a closed surface (blue). Black line segments indicate where the laser is switched on. The red lines are transfer scanning trajectories to bridge the gap between the ending point of a line and the starting point of the next one. During this transfer the laser is switched off. The influence of those transfer lines becomes significant when looking at Figure 3.17b. Here, the standard hatching pattern for a slice of the shell is depicted. The red transfer lines in the center correspond to a large portion of the overall process duration which is wasted without actually polymerizing the photoresist. By changing the arrangement of the hatching lines the accumulated length of red line segments can be reduced, increasing the printing speed (Figure 3.17c). For this, the standard hatching pattern generated by DeScribe was rearranged and modified utilizing a self-written MATLAB code.

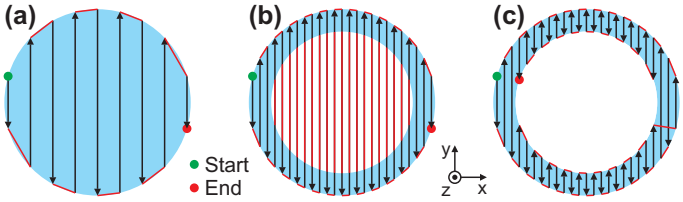

Figure 3.17. Hatching strategy for different printing regions. **(a)** Laser trajectory for an individual slice of the core with coarse slicing. The laser is emitting on the black lines and is switched off on the red lines. Arrowheads indicate the scanning direction. **(b)** Individual slice from the shell with fine slicing and standard hatching pattern. The hatching distance is also chosen smaller than in **(a)** here. **(c)** Optimized hatching strategy for the shell, resulting in a smaller overall length of the red line segments, effectively decreasing the printing duration.

The experimental results are summarized in Figure 3.18. Top-view microscope images of the coarsely sliced and hatched core structure without (Figure 3.18a) and with (Figure 3.18b) subsequent printing of the shell with fine slicing highlight the different surface quality. In Figure 3.18a, the coarse

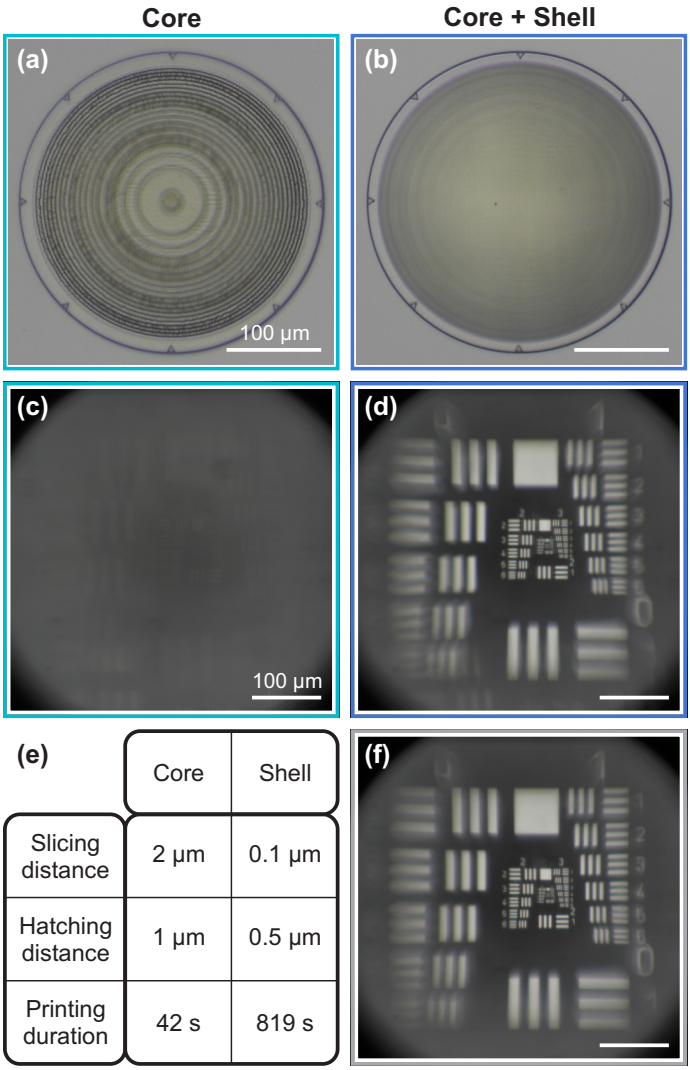

(e)	Core	Shell
Slicing distance	2 µm	0.1 µm
Hatching distance	1 µm	0.5 µm
Printing duration	42 s	819 s

Figure 3.18. Imaging quality of core-shell printed spherical lenses. **(a)** Top view of the coarsely sliced and hatched core structure. **(b)** Core structure covered by shell with fine slicing. The steps visible in **(a)** are almost completely removed. **(c)** USAF 1951 resolution test target imaged by the core structure from **(a)**. The image is barely visible. **(d)** Resolution test target imaged by the core-shell structure from **(b)**. **(e)** Printing parameters for core and shell. **(f)** Resolution test target imaged by a reference lens printed in a single step, but with the fine slicing and hatching parameters from the shell. The imaging quality is comparable to **(d)**. All scale bars are 100 µm wide.

slicing and hatching results in visible printing artifacts, which can be removed when adding the shell with finer slicing and hatching (Figure 3.18b). The spherical lens measures 300 µm in diameter, and has a radius of curvature of 300 µm, resulting in a height of 40 µm. The focal length is 600 µm, assuming n = 1.5 as refractive index. The lens sits on a 5 µm thick round base plate with 320 µm diameter, which incorporates arrowhead-shaped marks to facilitate the evaluation of shape accuracy measurements. To emphasize the role of the finer slicing and hatching parameters of the shell we compare the images of a USAF 1951 resolution test target, imaged by the core structure (Figure 3.18c) and by the core-shell structure (Figure 3.18d). The core structure is barely capable of producing an image of the test target, the contrast in Figure 3.18c is very low. In contrast, the image produced by the core-shell structure in Figure 3.18d has a much better overall quality, which is mostly attributed to the better surface smoothness and the smaller shape deviations. The printing parameters for the two parts are given in the table in Figure 3.18e. In order to estimate the time saving we compare the core-shell structure to a lens with identical dimensions which was printed in a single step, using the fine slicing and hatching parameters of the shell. The USAF 1951 test target imaged by this lens (Figure 3.18f) serves as a benchmark for imaging quality and looks very similar to the image produced by the core-shell structure in Figure 3.18d. The printing duration of this lens was 1142 s (~19 min). The printing of the combined core-shell structure took 861 s, corresponding to a 25% reduction in printing time while maintaining high imaging quality.

3.6 CONCLUSION

The fabrication of micro-optical elements with diameters around 500 µm was successfully demonstrated. Keeping the boundary conditions for 3D printing discussed in the previous chapter in mind, three doublet objectives were designed as exemplary structures. Each objective consists of two lenses with four aspheric free-form surfaces, resulting in a high degree of freedom in the optical design. A fabrication strategy for the overhanging parts of the objectives was introduced. The complex shapes of all lens surfaces were analyzed by confocal microscopy measurements, and the resulting shape deviations were compensated in an iterative optimization process. After optimization, the imaging quality of the printed objectives was increased significantly. The optimized doublets were combined with different optical components to investigate their potential implementation in endoscopic applications. First,

a doublet objective was printed onto the end of a semi-flexible image conducting fiber. The imaging quality of the combined fiber-objective system is not limited by the quality of the printed objective, but rather by the coarse pixel distribution of the cores in the image conducting fiber. Because certain endoscopic tasks require an off-axis viewing direction, different approaches for changing the light's direction of propagation were tested. A viewing direction perpendicular to the fiber axis was demonstrated, based on the 3D printing of a tilted surface which was subsequently covered with a metallic reflective coating. Apart from fibers, sensor chips usually used in commercial cameras were utilized as printing substrates. Here, the fabrication process needs to be adapted when printing close to the sensor surface, in order to avoid micro-explosions in the photoresist. We demonstrate camera sensors with objectives designed for infinite and finite object distance. Our imaging qualification suggests that combined optical systems could be used for tasks like gesture recognition. The compatibility of our fabrication technique with endoscopic distal-chip systems was shown using a non-functional sensor chip as printing substrate. Furthermore, we also investigate a method to decrease the shape deviations while keeping the printing duration at an acceptable level. The slicing and hatching parameters are not constant in the 3D model anymore, but are adapted in different locations in the model. This could be important on the way towards commercial 3D printed components, as it can decrease the printing duration by 25%.

4

3D PRINTED LENSES ON THE MILLIMETER SCALE

This chapter describes the fabrication of optical elements on the millimeter scale by 3D printing via two-photon polymerization. The maximum size of a 3D printed object is limited by the diameter of the writing field of the focusing objective, and was therefore restricted to ~800 µm so far. While bigger objects can be created by combining several structures of this size, the interfaces between adjacent blocks will be clearly visible, which can have a negative influence on the performance of optical elements. We overcome this by the use of a large writing field objective. Furthermore, we use a new printing material with optimized optical properties. The optical components fabricated by this combination are free of stitching defects due to a single step exposure and exhibit an unprecedented glass-like appearance due to the low absorption of the resist material throughout the entire visible wavelength range. First, we demonstrate an aspherical lens for laser focusing, which has a diameter of 1 mm. We characterize and optimize its shape fidelity by confocal microscopy measurements and find the spot size of a laser focused by the lens close to the simulated optimum. Then we compare 3D printed half-ball lenses with 1 mm diameter to commercially available half-ball lenses of the same size and shape in terms of imaging quality, which is similar for both lens materials. Finally, we show that the diameter of 3D printed half-ball lenses can be increased to 2 mm and compare those lenses also to their commercially available glass counterparts.

This chapter is mostly based on the following publication:

S. Ristok, S. Thiele, A. Toulouse, A. M. Herkommer, and H. Giessen
"**Stitching-free 3D printing of millimeter-sized highly transparent spherical and aspherical optical components**",
Optical Materials Express **10**, 2370-2378 (2020),
DOI 10.1364/OME.401724.

4.1 INTRODUCTION

Optical elements with diameters in the millimeter range are nowadays standard components in many technical devices. While the most prominent example is for sure the ever-present smartphone camera, there is a multitude of other possible applications, ranging from industrial and medical endoscopes to numerous optical sensors used by the automotive industry in state-of-the-art vehicles. Historically, the diameter of men-made lenses is in the centimeter regime, due to the fabrication methods available in those days. With modern highly precise and automatized production tools the accessible diameter range for optical elements has been widened dramatically. Concerning the optical design of a certain lens system with centimeter size, it is usually straightforward to scale the design down to millimeter size, which is due to scaling laws even in favor when it comes to aberration control. Despite the advances in controlling, optimization and automation of classical lens-making techniques such as grinding or milling, glass lenses with aspherical shape with few- or sub-millimeter diameter are rarely available. Spherical glass lenses (half-ball lenses or rod lenses with spherical shaped end facet(s)) are commercially available down to 0.3 mm diameter, however, this strongly limits the optical design freedom. Complex lens systems required for more elaborate applications often make use of aspherical lenses, which cannot be manufactured on this scale by grinding or milling. Here, different 3D printing techniques have emerged as interesting alternatives [9, 13, 68, 70, 71]. Particularly the fabrication of polymer lenses by two-photon polymerization is of great interest, as it has the capability to create arbitrary free-form surfaces and intrinsically offers excellent alignment of multi-component lenses [36, 66, 72–74]. So far, the diameter of 3D printed optical elements fabricated by this technique varied from tens of micrometers to several hundreds of micrometers [34, 37, 61, 67, 75–78], which leaves a size gap around the millimeter scale to the aforementioned standard fabrication techniques. The challenge thus is to increase the diameter of the 3D printed optical elements from the micrometer to the millimeter realm. The limiting factor here is the writing field diameter of the focusing objective, which is ~800 µm for a standard 25x objective which was used for many different structures. By dividing bigger objects into smaller building blocks which fit into the writing field of this objective, it is in principle possible to print millimeter-sized structures, however, the stitching marks between adjacent units usually deteriorate the imaging quality of lenses fabricated using this procedure. Advanced fabrication techniques can reduce the visibility of stitching marks, e.g., by synchronizing the movement of the

translation stage and the laser scanner [79], but it is more convenient to print a lens in one single step without any stitching. Furthermore, the increased size and volume of the lenses reveals one of the downsides of the commonly used materials: they often retain a yellow color after polymerization due to residual photoinitiator, which also has negative influence on the imaging quality, in particular in structures with large volumes.

We overcome these challenges with the help of two distinct advances: The use of a commercially available objective with a large writing field in combination with a new commercially available photoresist with low absorption and low luminescence in the visible wavelength range [57]. This combination enables us to 3D print millimeter-sized lenses without stitching marks and unprecedented optical clarity. We demonstrate spherical and aspherical lenses with 1 mm diameter as well as spherical lenses with 2 mm diameter. All lenses are printed directly on glass coverslips and consist of a single curved surface. The lenses are characterized in terms of shape fidelity, imaging quality, and modulation transfer function.

4.2 LENS FABRICATION

The 3D printer used for the fabrication is a Nanoscribe PPGT system. The supporting coverslip for the lenses is exposed to an oxygen plasma for 5 min to increase the adhesion of the polymerized structures. When the printing process is finished, the remaining liquid photoresist is dissolved by immersing the coverslip in a developing solution (mr-Dev 600, micro resist technology) for 25 min and subsequently in isopropyl alcohol for 5 min. After subsequent drying with nitrogen, the substrate is placed on a hot plate at 60°C for 1 h and is simultaneously illuminated by UV light to increase the degree of polymerization. An overview of the printed lenses under investigation is displayed in Figure 4.1a. The aspheric lens on the left is designed to demonstrate the superior focusing ability of non-spherical lenses with free-form surfaces. The lens diameter is 1 mm. The half-ball lenses in the middle and on the right have diameters of 1 mm and 2 mm and are printed to compare them to commercially available glass lenses with the same shape and size. The new Nanoscribe resist used for the lenses is called IP-Visio (Figure 4.1d). Compared to other resists for two-photon polymerization, e.g., Nanoscribe IP-S, the yellow color is significantly reduced. This is particularly obvious in Figure 4.1b, where cubes with 1 mm side length made from IP-S (left) and IP-Visio (right) are displayed side-by-side. The picture was taken nine months after fabrication, which demonstrates that the high optical

quality does not deteriorate over time. During this period, the sample was stored under ambient conditions. The 10x objective used for the fabrication is depicted in Figure 4.1c. It has a numerical aperture of 0.3, a working distance of 700 µm and a specified writing field diameter of 1 mm. The lenses presented in this chapter are printed with a slicing distance of 1.5 µm and a hatching distance of 0.5 µm. The laser power parameter is set to 100% and the laser focus is moved in lateral direction at a scan speed of 50,000 µm/s. To avoid the dose accumulation discussed in Subsection 2.3.3, a delay of 30 s between successive slices was used. The writing time is 3 h for the aspheric lens, 5 h for the 1 mm half-ball lens, and 23 h for the 2 mm half-ball lens.

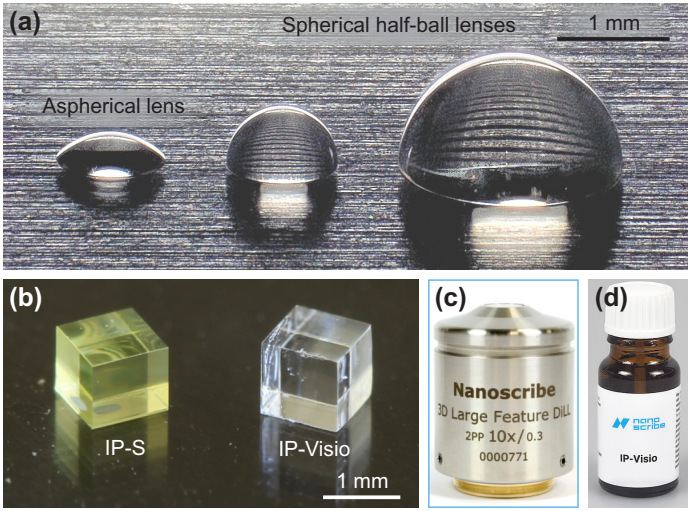

Figure 4.1. 2PP fabrication of millimeter-sized singlet lenses. **(a)** Overview of the different lenses discussed in this chapter, an aspheric lens with 1 mm diameter and half-ball lenses with 1 mm and 2 mm diameter. **(b)** 3D printed cubes with 1 mm side length, made from the photoresists IP-S and IP-Visio. **(c)** 10x objective with large writing field diameter. Image courtesy of Nanoscribe GmbH & Co. KG. **(d)** Photoresist IP-Visio used for all printed lenses in this chapter. Image courtesy of Nanoscribe GmbH & Co. KG.

4.3 ASPHERICAL FOCUSING LENS

Spherical glass lenses with diameters ranging from 0.3 mm up to several millimeters are standard products nowadays, e.g., ball-lenses for fiber coupling. While they are well-suited for certain applications, better results can often be achieved by introducing non-spherical surfaces into the optical system. In order to illustrate this, a spherical and an aspherical lens with identical center thicknesses and diameters are compared in Figures 4.2a and 4.2b. The superior focusing capability of the aspheric design is obvious due to correction of spherical aberration. The importance of aspherical components increases even more when we look at more complex optical systems with multiple optical elements. Being able to create non-spherical lens shapes is therefore one of the crucial advantages of 3D printing.

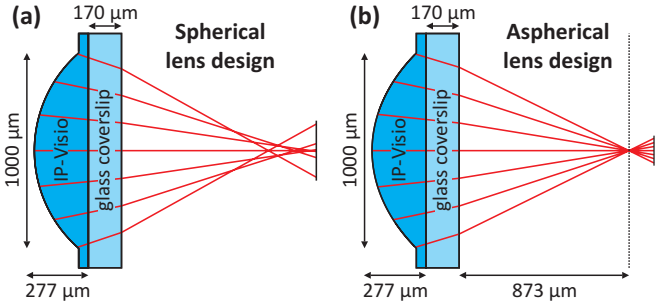

FIGURE 4.2. Spherical and aspherical singlet lens design for laser focusing. **(a)** Optical design of a spherical focusing lens. The rays do not intersect in a single point. **(b)** Optimized aspherical lens design with same diameter and thickness as the lens in **(a)**. Due to the reduction of spherical abberation a sharp focus is generated.

The shape of the curved surface of the aspheric lens is described by the formula

$$z(r) = \frac{\rho r^2}{1 + \sqrt{1 - (1+k) \cdot (\rho r)^2}} \tag{4.1}$$

where $z(r)$ is the thickness of the lens in dependence of the radial distance r to the lens center. $\rho = 1/R$ is the inverse of the radius of curvature R and

k is the conical constant. The numeric values for the aspherical lens design are R = 598 µm and k = -0.577.

We fabricate an aspherical lens corresponding to the design in Figure 4.2b. A 170 µm thick coverslip is used as substrate and is included in the optical design. First, a baseplate with a diameter of 1.2 mm and a thickness of 50 µm is printed, which is required for subsequent shape characterization. Then, the actual lens with a diameter of 1 mm and a center thickness of 227 µm is printed on top of the baseplate.

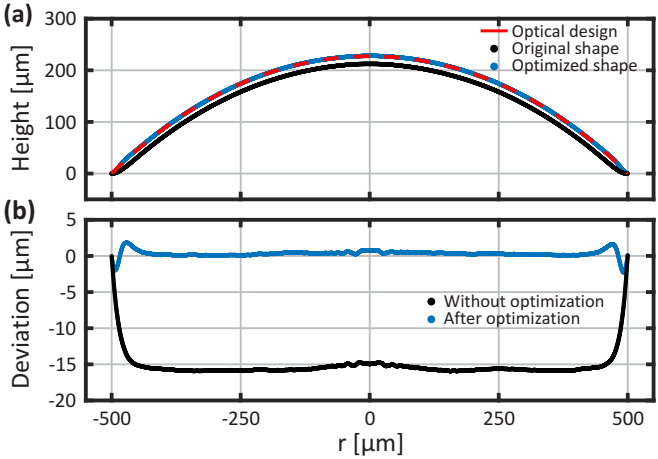

Figure 4.3. Surface analysis of aspherical lens with 1 mm diameter. **(a)** Lens profile before and after optimization compared to the optical design. **(b)** Shape deviation before and after optimization.

In order to achieve the designed spot size it is essential that the deviation of the printed lens from the optical design is minimized. Therefore, we characterize the lens surface using a confocal microscopy technique (Nanofocus µsurf expert). We fabricate four identical lenses and extract two profiles per lens, using the flat area of the baseplate as reference plane. In Figure 4.3a the mean profile (black) is compared to the optical design (red). The printed lenses are on average 15 µm thinner in the center than designed, which results from shrinking effects during the polymerization and the subsequent developing step. The radial dependence of the shape deviation is depicted in black in Figure 4.3b. We use a polynomial fitting function to determine the

shape of the deviation. The fitting function is added to the original optical design and the lens is reprinted. This procedure is repeated iteratively to optimize the shape fidelity. The surface profile after two iterations (blue) in Figure 4.3a matches the optical design much better than the first printed lens (black). Over the main part of the lens (r < 450 µm) the residual deviation (Figure 4.3b, blue) is smaller than 1 µm after optimization.

For further characterization, the focusing capability of the lens is compared to simulations. The lens is designed for an operation wavelength of 550 nm using the raytracing software ZEMAX OpticStudio. In the optical design the radius of the Airy disk at the focal point is 0.762 µm. In the experiment, a collimated laser at 550 nm with a beam diameter of 1 cm is used for illumination. The beam size is chosen much larger than the lens aperture to ensure homogeneous illumination. The laser is focused by the printed lens 880 µm behind the glass coverslip, which is very close to the designed distance of 873 µm. In the focal plane a weak ring-shaped intensity distribution is visible around the actual spot (Figure 4.4a). The Gaussian functions fitted to profiles through the focus in x- and y-direction (Figure 4.4b) have beam radii of 0.760 µm in x-direction and 0.711 µm in y-direction, which is in good agreement with our simulations.

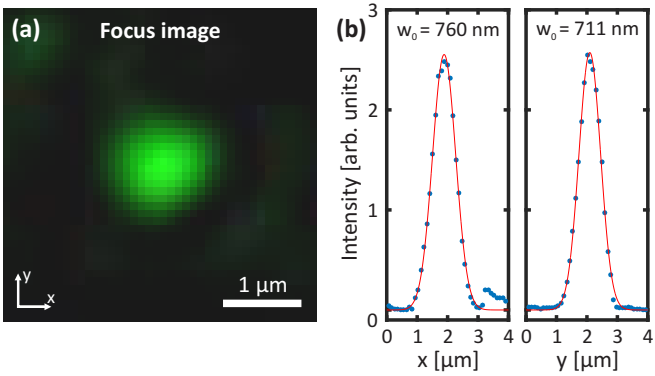

Figure 4.4. Green laser focused by an aspherical lens with 1 mm diameter. **(a)** Image of the focal plane under monochromatic illumination at 550 nm in combination with the aspherical lens from Figure 4.2b. **(b)** Profiles through **(a)** in x- and y-direction with Gaussian fitting functions.

Possible reasons for the ring-shaped halo around the focus spot are the surface roughness of the printed lens, the residual shape deviation, especially in the outer part of the lens, and diffraction at the lens aperture. The bigger deviations at the rim of the lens are most likely caused by shrinking of the flat baseplate. Our optimization algorithm only takes into account the measured height deviation. We assume, however, that there is also a lateral component of the shrinking behavior. A lateral shrinking of the flat ring surrounding the lens could lead to the observed deviations at the transition to the curved lens surface. For a more exact prediction of the shrinking effects the interplay of lateral and perpendicular shrinking should be considered, however, this requires the evaluation of numerous test structures of different size and shape and extensive simulations, which is part of another ongoing thesis at our institute.

4.4 COMPARISON WITH GLASS LENSES

While our aspherical lenses emphasize the design freedom of our 3D printing technique, it is impracticable to compare them directly to similar lenses made from glass, which is the ultimate benchmark material for polymer optics in terms of stability and surface roughness. Aspherical glass lenses with 1 mm diameter cannot be obtained easily, therefore we print spherical half-ball lenses with diameters of 1 mm and 2 mm and compare them to readily available equivalent glass lenses (Edmund Optics).

4.4.1 *Shape analysis*

Before we compare the optical properties of the lenses we have to verify that both lenses have identical or at least very similar shape. Therefore, we take scanning electron microscopy (SEM) images (Figures 4.5a and 4.5b). While the glass lens has a perfectly flat bottom and therefore lies tightly on the substrate, a small part at the edge of the printed lens has delaminated from the coverslip. We attribute this to internal tension in the lens caused by shrinking. Furthermore, on the top of the printed lens different slices can be distinguished. This can be expected, as the lens is composed of slices with a finite thickness, resulting in a staircase-shaped surface. For the main part of the lens the difference in diameter between adjacent slices is comparably small and the transition between them is smoothened by the finite voxel size and the proximity effect during the printing process [65]. As the lens

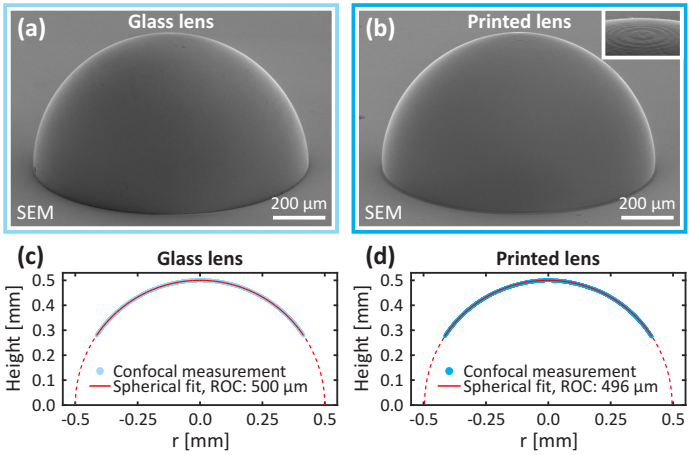

Figure 4.5. Half-ball lenses with 1 mm diameter. **(a)** SEM image of the glass lens. **(b)** SEM image of the 3D printed lens. The inset shows a magnified image of the top of the lens. **(c)** Surface profile of the glass lens. **(d)** Surface profile of the 3D printed lens.

surface becomes flatter towards the top, the subsequent slices differ more in diameter, which leads to higher visibility of the distinct steps. While decreasing the slicing distance could reduce this effect, this was omitted here, as it would significantly prolong the writing time. The surface profiles of both lenses are characterized using a confocal microscopy technique. As the measurement principle relies on light which is directly reflected from the curved lens surface, the steeper parts of the lens cannot be measured. The limiting factor is the numerical aperture of the microscope objective (50x, NA 0.95), which is used both for illumination and detection. As a result, the profile measurement is not performed for the total diameter of 1 mm, but only for the upper part of the lens up to a diameter of 0.83 mm (Figures 4.5c and 4.5d). Another limitation is the finite working distance of 300 µm of the microscope objective, since it makes it impossible to include the coverslip in the measurement, which is normally used as flat reference plane to compensate for any sample tilt caused by the microscopy setup. Because of these limitations we do not apply the iterative optimization used for the aspherical lenses. Instead, we determine the actual radius of curvature (ROC) of the measured area for both lenses by using a spherical fitting function, plotted in red in Figures 4.5c and 4.5d. The dashed red line extends the fit to the steeper regions which could not be measured. For the

glass lens the ROC is 500 µm, which perfectly matches the specifications. Due to shrinking, the printed lens has a ROC of 496 µm, which corresponds to a 0.8% deviation from the designed 500 µm.

4.4.2 *Imaging quality*

Since the shape analysis of the lenses shows only minor differences, it is reasonable to compare them also in terms of imaging quality. The used microscopy setup is sketched in Figure 4.6 and is similar to the setup published previously by Toulouse et al. [36]. Light from a white LED is collimated by an achromatic lens and illuminates a diffuser plate to ensure homogeneous radiant intensity. It is focused by a microscope objective onto the half-ball lens. A USAF 1951 resolution test target is placed between the objective and the lens. The image of the test target created by the lens is viewed with a standard microscopy setup consisting of objective, tube-lens, and CMOS sensor. As our lenses lack a physical aperture stop to block unwanted stray light, we add an adjustable iris diaphragm between the diffuser plate and the objective. Its position is chosen such that a sharp image of the iris is projected onto the coverslip supporting the half-ball lens. The diameter of the image of the diaphragm is then adjusted to match the diameter of the lens, simulating a physical aperture.

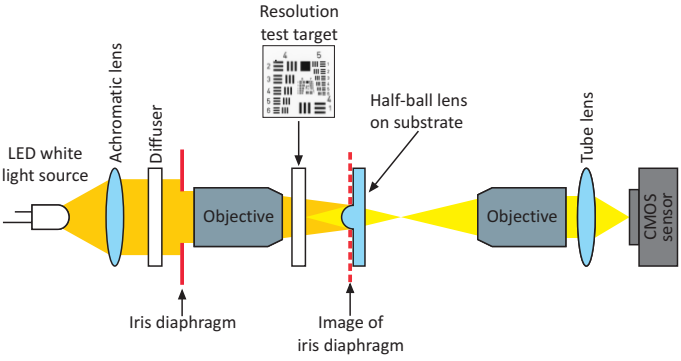

Figure 4.6. Microscopy setup for imaging comparison experiments, illumination beam path in dark yellow, detection beam path in light yellow.

The imaging quality of the two lenses is compared in Figures 4.7a and 4.7b. The object distance between target and half-ball lens is chosen such that the size of the image equals the original size of the test target (1:1 imaging). Exposure time, gain and white balance settings are identical for both images. The general color impression and contrast is very similar and no visible difference can be seen for groups 4 and 5. When zooming in on the groups 6 and 7 (Figures 4.7c and 4.7d), the glass lens shows a slightly better imaging quality, e.g., when looking at elements 4 to 6 of group 7. Reasons for this could be residual deviations from the spherical shape and the surface roughness. Overall, these measurements underline the excellent optical quality and performance of our 3D printed lenses as well as of the lens material.

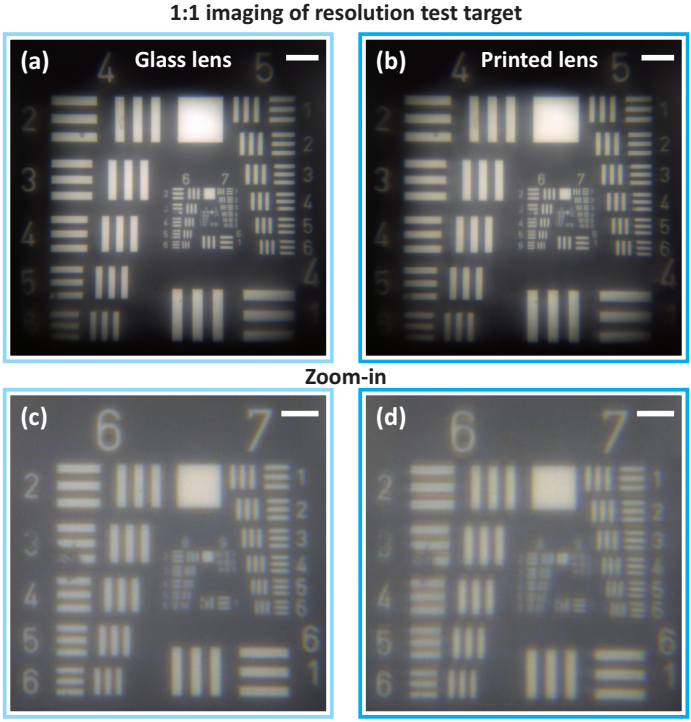

FIGURE 4.7. Imaging quality of half-ball lenses with 1 mm diameter. **(a)** Resolution test target imaged through a glass lens, scale bar: 100 µm. **(b)** Resolution test target imaged through a printed lens, scale bar: 100 µm. **(c)** and **(d)** Magnified images of the central area in **(a)** and **(b)**, scale bars: 30 µm.

4.4.3 *Modulation transfer function*

So far we have studied optics at the 1 mm scale, yet, our setup allows to push sizes even larger. According to specifications, the utilized 10x microscope objective should only be used for writing field diameters of up to 1 mm to ensure optimal structural fidelity. This is, however, not the ultimate size limit of our applied configuration. To demonstrate this, we also fabricate a half-ball lens with a diameter of 2 mm shown in Figure 4.8a. A glass lens is placed next to the printed lens to illustrate the visual similarity of the lens materials. We determine the ROC of the upper part of the printed lens to be 961 µm, corresponding to a deviation of 3.9%. The spatial root mean square roughness parameter Sq is 2.9 nm for the printed lens and 1.9 nm for the glass lens. In order to get an impression of the full cross-section of the lenses, we tilt the sample by 90° (Figures 4.8b and 4.8c). The horizontal red line indicates the surface of the coverslip and the dashed red line forms a spherical arc with a radius of 1 mm. While the arc overlaps well with the lens boundary of the glass lens in Figure 4.8c, the printed lens in Figure 4.8b shows deviations from the design. The lens has delaminated from the substrate at the edges, despite the previous plasma treatment which should ensure good adhesion. Delamination is most probably caused by increased internal tension, resulting from the shrinking of the bigger lens volume. The center-thickness is slightly larger and the lens has a stronger curvature than designed, which is corroborated by confocal microscopy results. Consequently, the shape of the glass lens and the printed lens is not identical, which has to be considered when comparing the imaging quality of the lenses. We use a commercially available measurement setup (Trioptics Image Master HR) to determine the modulation transfer function (MTF) (Figure 4.8d). The MTF of the printed lens falls below 10% contrast at 210 linepairs/mm, while this happens only at 290 linepairs/mm for the glass lens. We expect the glass lens to have a better MTF in general, which is true for spatial frequencies above 50 linepairs/mm. The better performance for lower frequencies could result from the delaminated parts of the lens reflecting light away and not contributing to the imaging, as light rays passing the outer sections of a spherical lens are known to deteriorate imaging quality. Overall, we can conclude that the performance of the 3D printed lens is comparable to the capabilities of the glass lens. As also significant efforts have been invested to optimize commercial glass lenses, we are confident that the shrinkage and additional minimal shape deviations in our 3D printed structures can be overcome as well. Additionally, we again observe that certain tailored deviations can even improve performance. The

freedom afforded by 3D printing allows to straightforwardly implement such tailored deviations, underpinning the strength of our ansatz.

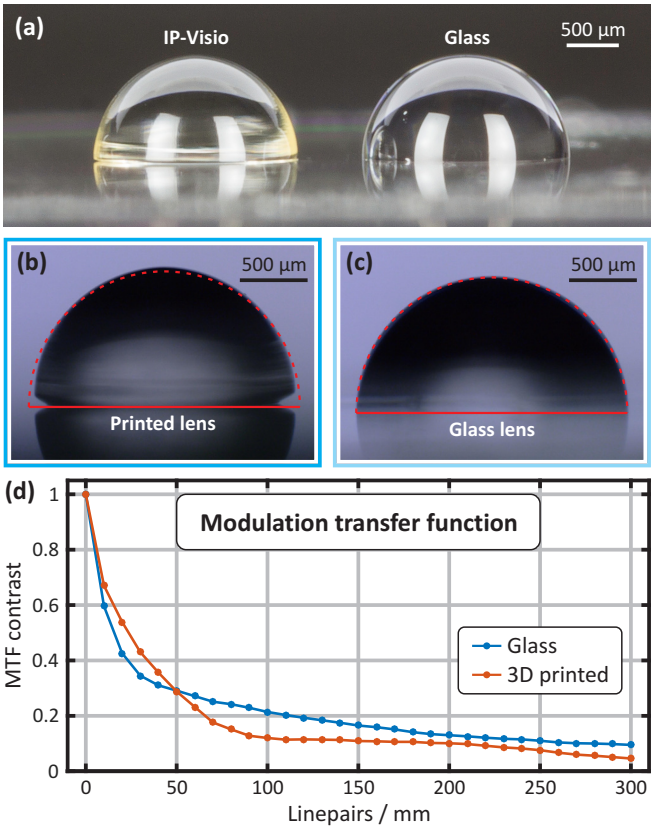

Figure 4.8. Half-ball lenses with 2 mm diameter. **(a)** Glass lens and printed lens side-by-side. Photographic image by Moritz Flöss. **(b)** Side-view of glass lens. **(c)** Side-view of printed lens. **(d)** Comparison of modulation transfer function for normal incidence (0°).

4.5 POST-PRINTING SURFACE SMOOTHING

The lenses described in this chapter so far were printed with a comparably large slicing distance of 1.5 µm. The main reason for this is the increased writing time for smaller slicing distances. In general, slice-by-slice fabrication leads to steps in inclined surfaces which were designed to be smooth (Figure 4.9b). If the slicing distance is small enough, the surfaces will often still be smooth, due to the proximity effect [65]. For a spherical half-ball lens, however, the diameter of subsequent slices (which are of circular shape) in the upper part of the lens is rapidly changing, as the surface gets flatter and flatter towards the top. Thus, the individual slices can be distinguished there. In Figure 4.9a, a confocal surface measurement shows the upper part of a 3D printed half-ball lens with 2 mm diameter. The discrete steps caused by the large slicing distance are clearly visible. While the imaging quality of this lens was comparable to a smooth glass lens, a smoother lens surface should be beneficial for more critical imaging applications and multi-lens systems. This can be achieved by introducing a post-printing coating step, similar to the one described in [13]. A thin layer of an UV curable, optically transparent liquid is deposited on the lens surface. The liquid effectively forms a droplet encapsulating the lens. The general shape of the droplet is determined by the shape of the underlying lens surface. On the micro scale, the liquid connects the edges of subsequent steps via a meniscus-shaped curve, which resembles the lens design much better than the discrete steps (Figure 4.9c). After the liquid film has been applied, it is baked on a hotplate and hardened by UV radiation

Here, we use SU-8 photoresist (micro resist technology) as coating material, which is a standard photoresist for lithography applications. The 3D printed lens and the supporting glass coverslip are first cleaned with isopropyl alcohol and dried with nitrogen, and then placed on a spin coater. A drop of SU-8 is dispensed on the sample with a pipette, covering the entire sample surface. The spin coating process is started immediately after SU-8 deposition. First, the sample is spun for 60 s at 250 rpm, followed by 45 s at 6000 rpm. Afterwards, the back of the glass coverslip is carefully cleaned with acetone, to remove any residual SU-8. The sample is then placed on a hotplate set to 95 °C for 2 min. Then the photoresist is hardened by UV illumination for 20 s (Karl Suss MJB-3 Mask Aligner). Finally, the sample is again placed on the hotplate at 95 °C for 2 min.

A visual comparison of the top region of a printed half-ball lens with 2 mm diameter before and after the coating process is shown in Figure 4.10.

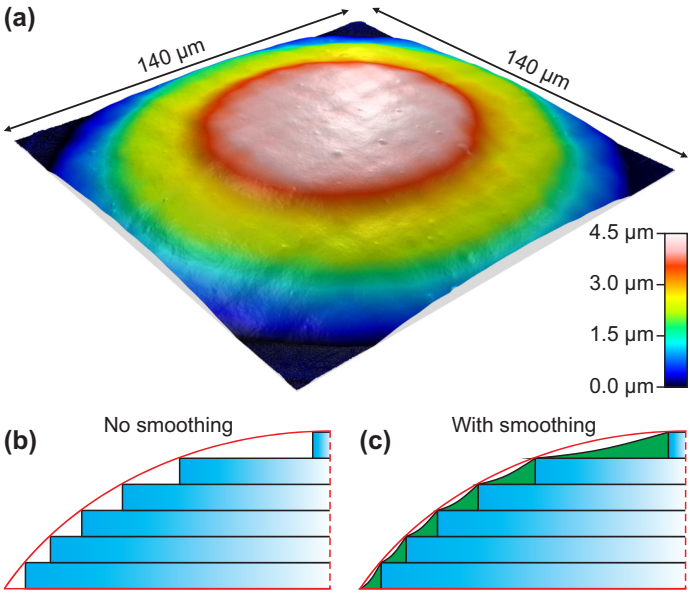

FIGURE 4.9. Deposition of SU-8 on 3D printed lenses for surface smoothing. **(a)** Confocal microscopy measurement of the top of a printed half-ball lens with 2 mm diameter. The slicing distance of 1.5 µm is clearly visible. **(b)** and **(c)** Illustration of a curved lens surface divided into slices with fixed height. The deviation with respect to the design (red) can be reduced by coating the lens with a transparent liquid material (depicted in green) which is subsequently hardened.

In addition, a glass lens made from N-BK7 glass with identical dimensions is characterized as a reference in terms of surface roughness. Without the coating step, the printed lens exhibits visible artifacts caused by the printing process, e.g., linear patterns resulting from the laser scanning trajectory (Figure 4.10a). The step-like topography can also be distinguished. After the SU-8 deposition and hardening, the surface has a much smoother appearance and the printing artifacts are no longer visible (Figure 4.10b). In general, the surface looks very similar to the surface of a reference glass lens in Figure 4.10c. The coating reduced the RMS roughness of the printed lens from 2.9 nm to 1.1 nm (glass lens: 1.9 nm). This emphasizes that the coating step not only improves the general shape accuracy of the lens surface, but also results in a surface finish which is comparable to lenses made from glass.

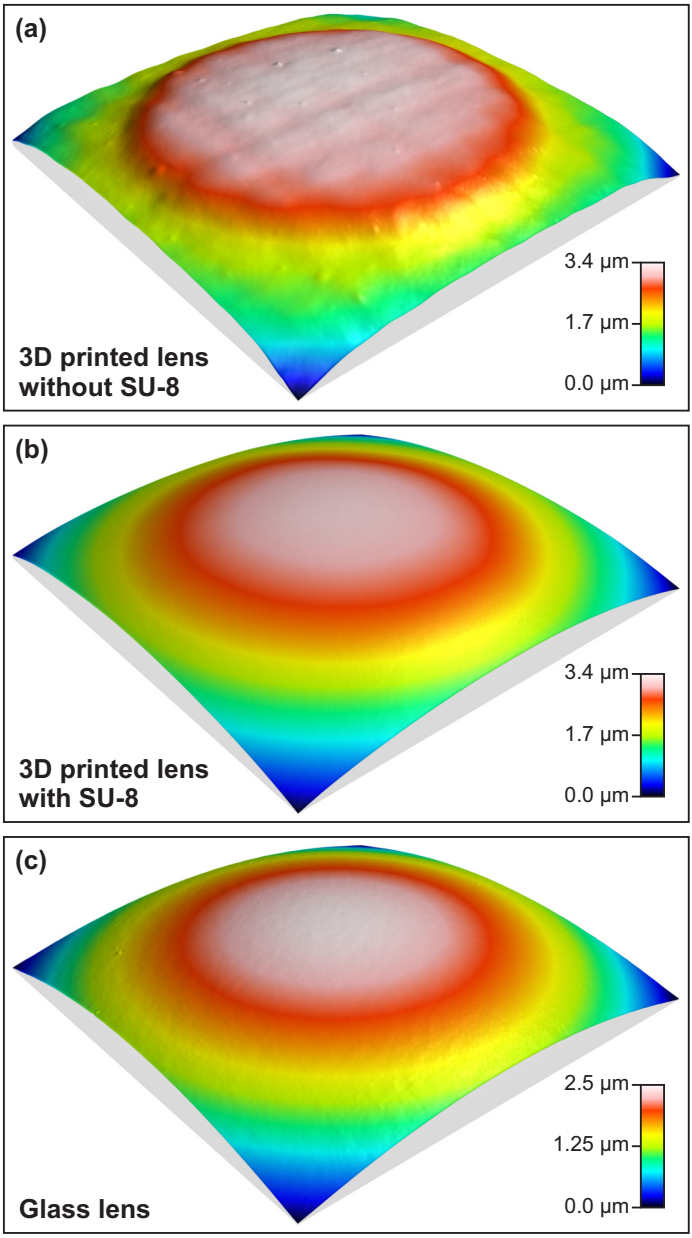

FIGURE 4.10. Confocal microscopy measurements of different half-ball lenses with 2 mm diameter. **(a)** Top of a printed lens without post-printing smoothing. **(b)** Top of a printed lens with smoothed surface. **(c)** Top of a commercial glass lens.

4.6 CONCLUSION

In conclusion, we have successfully fabricated aspherical and spherical lenses with diameters up to 2 mm by femtosecond 3D printing. Our aspherical lenses are optimized in terms of shape fidelity and have high focusing capability, outperforming commercial spherical glass lenses and illustrating the advantage of free-form 3D printing. Spherical half-ball lenses with 1 mm diameter show good imaging quality nearly equal to comparable glass lenses. The modulation transfer function of a printed half-ball lens with 2 mm diameter generally shows a behavior similar to the MTF of the glass counterpart. As they are not optimized, both printed half-ball lenses show certain deviations from the optical design, which are more prominent for the bigger lens. These shape deviations result mainly from the shrinking of the photoresist. The shrinking effects can be effectively counteracted if the lens shape can be characterized accurately. Since this can be challenging for bigger lenses and steeper optical surfaces, new measurement methods will be considered in the future, e.g., X-ray tomography. In order to reduce the residual artifacts caused by slicing and hatching on the lens surface, we investigated a post-processing method where the lenses are coated with a thin layer of a transparent photoresist, which is then hardened by UV light. We find the resulting surface quality comparable to commercially available glass lenses.

Although the lenses studied in this work are basic optical components with a single curved surface, the knowledge of the underlying fabrication process is a crucial first step towards more complex optical systems, e.g., free-hanging lenses with two surfaces or multi-lens objectives for smartphone cameras. Furthermore, we expect the new resist to have a high damage threshold due to its high transparency, which is crucial for high-power applications, e.g., customized optical instruments for medical surgery.

5

ANTI-REFLECTIVE COATINGS FOR 3D PRINTED LENSES

In this chapter, we introduce the fabrication of multi-layer anti-reflective (AR) coatings on 3D printed micro-optics. A conformal low-temperature atomic layer deposition (ALD) technique is optimized in order to create high-quality 4-layer AR coatings, which can decrease the broadband reflectivity of coated flat substrates in the visible to below 1%. In contrast to standard coating methods, the unique properties of ALD enable the simultaneous deposition of conformal anti-reflective coatings on all surfaces of 3D printed micro-optical multi-lens systems, which contain undercuts and cavities. Coated and uncoated 3D printed test structures are investigated and compared using transmission measurements, emphasizing the enhanced transmission through AR coated interfaces. Finally, we use a 3D printed double-lens imaging system to illustrate the advantage of our ALD process, as the internal lens surfaces cannot be coated using standard techniques. In this multi-lens system, the reflectivity is significantly reduced and the transmission is enhanced. For optical systems with even more lenses, the importance of AR coatings is even higher, especially when the lenses are used for low-light applications.

This chapter is mostly based on the following publication:

S. Ristok, P. Flad, and H. Giessen
"**Atomic layer deposition of conformal anti-reflective coatings on complex 3D printed micro-optical systems**",
Optical Materials Express **12**, 2063-2071 (2022),
DOI 10.1364/OME.454475.

5.1 INTRODUCTION

In order to manufacture high-quality micro-optical devices, the fabrication process has to be controlled and monitored very precisely, similar to the commercial fabrication of macroscopic optical elements. While the fabrication methods on the macroscopic scale are well-established standard processes nowadays, 3D printing of optics is a comparably new technique. To unleash the full potential of optical systems designed on the micrometer scale, it is necessary to transfer the experience and knowledge of macroscopic optical systems to the micro-realm. This results in a list of key elements which are required to realize complex micro-optical designs. First, the refractive index and the dispersion of the lens material must be carefully characterized in order to transfer those material parameters to the otical design software. This characterization has already been done for many standard 3D printing materials [57, 80]. Furthermore, the general shape of an optical surface should match the optical design as close as possible. Because 3D printed structures naturally experience a certain degree of shrinking after development, the shape accuracy of the first printing iteration is usually not sufficient. This can be overcome by the iterative shape optimization procedure introduced in Chapter 3. While most optical systems consist of transparent refractive or diffractive elements, absorptive structures are also important to include aperture stops which can significantly increase the imaging quality in complex optical systems. For 3D printed micro-optics, there are different approaches for the fabrication of absorptive structures, e.g., evaporating absorptive or reflective materials [37], filling hollow cavities in the 3D printed structure with absorptive black liquid [36, 81] or by direct laser writing using a black photoresist. As the applications for 3D printed micro-optics become increasingly demanding, the design of optical systems needs to become more complex. Usually, this is achieved by combining multiple optical elements (lenses, aperture stops, etc.). As the number of optical interfaces increases, the overall transmission through the system is reduced due to Fresnel reflections at the interfaces. For micro-optical elements with a single optical surface, there are various microfabrication techniques for AR coatings, ranging from 3D printing of moth-eye type AR coatings [82] over ion-assisted electron beam evaporation [83], to the deposition of polymer or metal oxide nanoparticles by spin-coating from the liquid phase [84, 85]. For multi-lens systems, anti-reflective coatings play an important role, as well as the lateral alignment of the lenses and the axial distances between them. Such multi-lens systems can be fabricated with perfect alignment via 3D printing if all components are interconnected with supporting structures,

resulting in a single-step printing process. Unfortunately, this single-step fabrication makes the application of AR coatings on all lens surfaces very challenging.

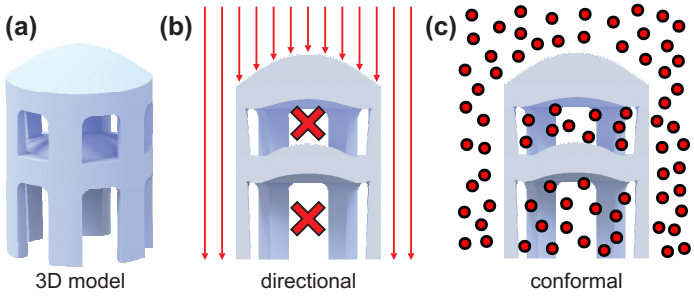

Figure 5.1. Directional vs. conformal coating techniques. **(a)** CAD model of a typical 3D printed doublet lens imaging system. **(b)** Illustration of directional material deposition (red arrows). Crosses mark regions which cannot be reached. **(c)** Conformal coating process where material is deposited from the vapor phase. Red dots symbolize the coating material.

To illustrate this, a 3D model of a doublet lens imaging system introduced in Chapter 3 is shown in Figure 5.1a. The bottom lens is connected to the supporting substrate by six supporting pillars, which also form a connection between the bottom and the top lens. Consequently, the lens surfaces cannot be coated separately like in macroscopic polymer optics, e.g., eyeglasses. Instead, all surfaces have to be coated in one single step, which effectively limits the choice of possible coating techniques. Most of the standard coating methods, e.g., sputtering and electron beam evaporation, are based on the directional deposition of the coating material. The lower surface of the top lens and both surfaces of the bottom lens cannot be reached by coating material which is applied to the lens from the top (Figure 5.1b). Thus, only the upper surfaces of the top lens can be coated by a directional process, and therefore such processes are not suited for the coating of micro-optical multi-lens systems. To overcome this, a conformal coating method is required where the lens is surrounded by a carrier medium (e.g., a gas or a liquid) containing the building blocks of the AR coating (Figure 5.1c). If the openings in the 3D printed structure are sufficiently large, the carrier medium can enter into the hollow parts of the lens system (between top and bottom lens and between substrate and bottom lens) and the coating can be deposited

there. One approach using a liquid as carrier medium is the deposition of single layer AR coatings consisting of silica nanoparticles [86]. Here, we introcude an atomic layer deposition process where the coating material is deposited on the lens from the vapor phase.

5.2 ATOMIC LAYER DEPOSITION

Anti-reflective coatings can in principle be fabricated using various different techniques. Many standard processes are based on adding a thin homogeneous layer of a material with a different refractive index than the substrate material (the lens), e.g., evaporating a single layer of magnesium fluoride (MgF_2) [87]. Other approaches are based on altering the surface topography of the lens in order to achieve a smooth transition between the refractive index of the lens and the incident medium, e.g., by nanostructuring the surface of polymer lenses using ion-assisted plasma etching [88]. While both methods are directional techniques and therefore are not feasible for the coating of 3D printed multi-lens systems, they highlight one of the key prerequisites concerning AR coatings for visible light: the layer thickness is typically in the sub-wavelength region, and therefore must be controlled with nanometer precision. This is achieved by our PICOSUN® R-200 Advanced atomic layer deposition system, which enables the simultaneous coating of all external and internal surfaces of an optical lens system. In the past, ALD has been used to fabricate different types of optical coatings on different substrate materials [89–92]. Standard ALD coating processes are conducted using process temperatures of several 100 °C, which would destroy our polymer lenses. Instead, we apply our coatings at 150 °C, which can be sustained by the polymer structures. With our system, coatings made from four different inorganic materials can be realized: silica (SiO_2), titania (TiO_2), alumina (Al_2O_3) and hafnia (HfO_2). Apart from the fabrication of AR coatings, those materials can also be used as passivation and protection layers for more sensitive structures, e.g., to prevent the degradation of polymer structures in certain chemical solvents or to avoid the diffusion of water molecules into the polymer [93]. AR coatings on polymer lenses also increase their physical and chemical durability, which is particularly interesting for lenses designed for the use in medical endoscopic applications. For the fabrication of AR coatings via ALD, a glass coverslip with 3D printed structures (or any other substrate) is placed inside the vacuum chamber of our ALD system at a pressure of ~6 mbar and a temperature of 150 °C. We insert the sample into the vacuum chamber 24 h prior to the

actual coating deposition in order to achieve thermal equilibrium. Furthermore, any volatile substance inside the printed polymer structures should evaporate during this phase, e.g., solvent from the chemical development or water molecules from atmospheric humidity.

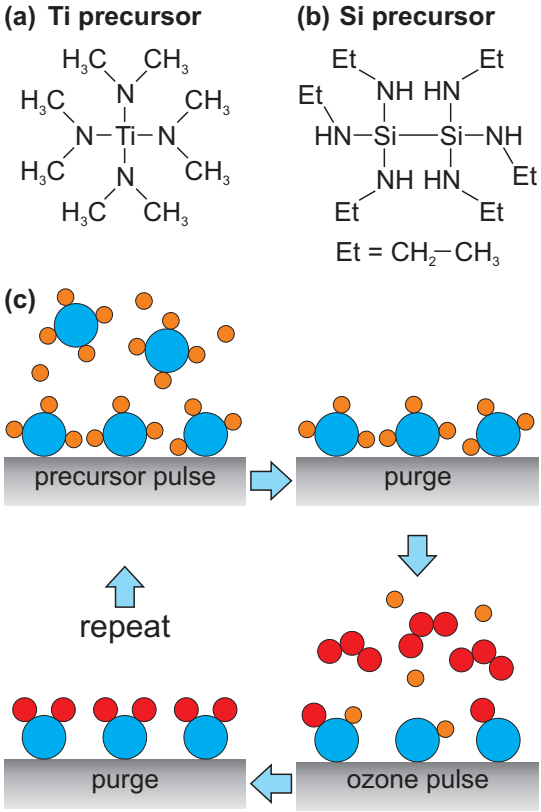

FIGURE 5.2. Atomic layer deposition cycle illustration. **(a)** Ti precursor molecule Tetrakis(dimethylamido)titanium(IV). **(b)** Si precursor molecule Hexakis(ethylamino)disilane. **(c)** Coating cycle overview. After a certain settling time the precursor molecules have deposited on the lens surfaces and the excess molecules are removed. The organic ligands of the precursor molecules are then replaced by oxygen atoms provided by ozone molecules. The reaction byproducts are removed and the cycle can start anew and is repeated until the desired material thickness is reached.

Our AR coatings consist of multiple layers of TiO_2 and SiO_2. Silicon and titanium are supplied by precursor molecules shown in Figures 5.2a and 5.2b. The Ti precursor consists of a central titanium atom surrounded by four identical organic ligand groups (Tetrakis(dimethylamido)titanium(IV)). The Si precursor has two silicon atoms in the center, surrounded by six ligands (Hexakis(ethylamino)disilane). Both precursors are liquid under standard conditions. The deposition cycle is outlined in Figure 5.2c. The lens (or any other substrate) is placed inside the process chamber at a pressure of 10^{-6} mbar and a temperature of 150 °C. The bottles containing the precursors are heated to a temperature of 65 °C (Ti precursor) and 100 °C (Si precursor) during the whole deposition process. In the first step, the precursor pulse, the valve connecting precursor bottle and reaction chamber is opened for a specific amount of time, the pulse duration. The precursor molecules will deposit on every surface in the chamber, including the hollow cavities of the 3D printed structures. In the following purging pulse, the chamber is flushed with nitrogen (N_2) and the vacuum pump is switched on, in order to remove the precursor molecules which have not settled on any surface. Then, the valve to the ozone generator is opened for a specific time. As ozone is chemically highly reactive, the organic ligands of the precursor molecules are successively replaced by oxygen atoms, forming a thin layer of TiO_2 or SiO_2. The byproducts of the reaction are removed by another purging pulse. After this, the deposition cycle can be repeated until the designed layer thickness is reached. As the typical increase in layer thickness after one cycle is in the range of 0.1 nm, the layer thickness can be adjusted very precisely by the number of deposition cycles. This dependence, namely the average thickness per cycle, is determined for each material separately. A certain number of deposition cycles is executed, using a 5" silicon wafer as substrate. The silicon wafer provides a high refractive index contrast to the coating layer and therefore facilitates the measurement of the layer thickness by ellipsometry. Once the calibration is successfully completed, the actual coating is deposited on another silicon wafer, and the different material thicknesses inside the multi-layer stack are again determined by ellipsometry.

5.3 AR COATING DESIGN

Multi-layer AR coatings typically consist of two materials which have significantly different refractive indices. For our coating design, we use SiO_2 as low index material and TiO_2 as high index material. As we want to achieve a

broadband AR coating ranging over the whole visible wavelength spectrum, we choose a center wavelength of 550 nm for our design. Here, the refractive indices of the coating materials are n(SiO_2) = 1.479 and n(TiO_2) = 2.29. For simple AR coating designs, e.g., when only the transmission at one specific wavelength λ is important, the multi-layer stack consists of a certain arrangement of so called quarter-wave layers. For each quarter-wave layer, the condition $\lambda/4 = n \cdot d$ is fulfilled, where n is the refractive index of the layer material and d is the layer thickness. For more complex coatings, e.g., broadband AR coatings, the layer thickness can also be different and can no longer be calculated by simple analytical methods. Instead, programs like the free online design tool Thin Film Cloud[1] or the commercially available software Essential Macleod[2] can be used for the coating design. Here, the available materials, angle of incidence, spectral range, maximum layer count and the boundary materials can be specified and are included in the calculation and optimization of the AR coating design. The materials used for 3D printing of optical elements are designed to resemble the optical properties of standard lens materials (glass), therefore we use N-BK7 glass as lens material for the design, which is available in the standard material catalog. The coating is designed for a single air-glass interface where the light with a center wavelength of 550 nm impinges perpendicularly. We strive for a minimum number of layers to reach the desired target reflectivity in order to minimize fabrication time. The initial design was calculated using Thin Film Cloud with a target reflectivity of <0.5% between 440 nm and 660 nm. The resulting 4-layer design was then further optimized using Essential Macleod. The simulated reflectivity of the refined design is depicted in Figure 5.3a and the corresponding layer thicknesses in Figure 5.3b. While an uncoated air-glass interface typically reflects about 4% of the incident light in the visible spectrum, the reflectivity of the coated surface is below 0.5% between 440 nm and 660 nm, which covers the main part of the visible wavelength range. Apart from ellipsometry, we also use scanning electron microscopy (SEM) to analyze the fabricated layer structure in Figure 5.3c. The different layers are clearly visible in the SEM image on the left, where the cleaving face of a coated silicon wafer is depicted. Contrast enhancement was applied here for better visibility. The atomic composition of the different coating layers is illustrated by energy-dispersive X-ray spectroscopy (EDX). Oxygen containing regions are marked in green, silicon in purple and titanium in yellow color.

[1] https://lightmachinery.com/optical-design-center/thin-film-cloud/
[2] http://www.thinfilmcenter.com/essential.php

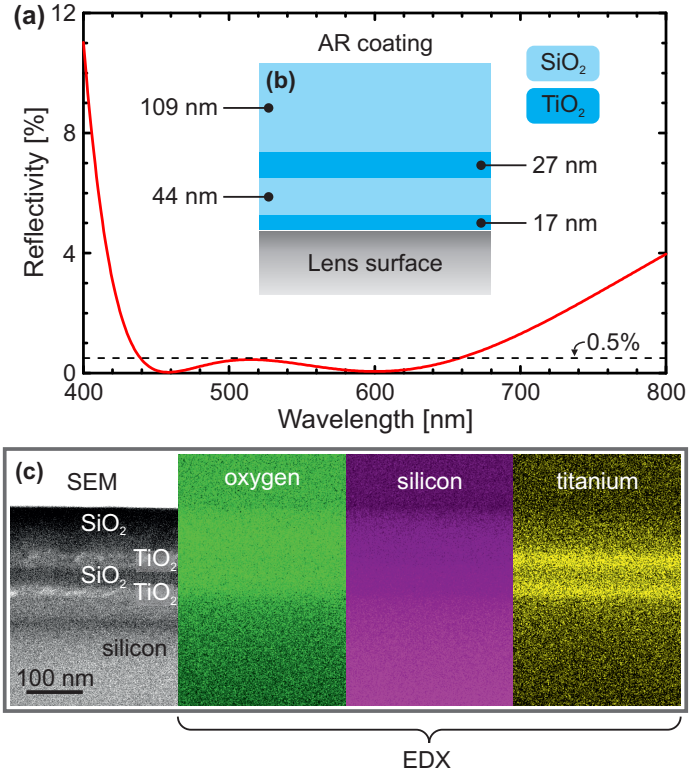

Figure 5.3. Design and material composition of AR coatings for 3D printed optics. **(a)** Simulated spectral reflectivity of an AR coated glass-air interface. **(b)** Multi-layer AR coating design. **(c)** Scanning electron microscopy image of a cleaving face of a coated silicon reference wafer and energy-dispersive X-ray (EDX) spectroscopy images. Layers containing oxygen are highlighted in green, silicon in purple, and titanium in yellow.

5.4 REFLECTIVITY MEASUREMENTS

The good agreement of the design and the deposited multi-layer stack in terms of layer thickness measured by ellipsometry and scanning electron microscopy is a strong indicator for a well-performing AR coating. Minor deviations in the layer thickness and the refractive index of the deposited materials might, however, still result in non-optimal performance. Therefore, the quantity of interest, namely the small reflectivity, must also be measured directly. Before we approach the challenging task of characterizing the performance of our coatings on 3D printed structures with sub-millimeter size, we first use a commercial Cary 7000 spectrophotometer to compare the reflectivity of AR coated and uncoated glass coverslips with $1 \times 1\,\mathrm{cm}^2$ size. The working principle is outlined in Figure 5.4a. Light from a broadband source (spectral range: 175 nm - 3300 nm) is impinging on the sample under an angle of incidence α. The reflected part of the light is collected by a detector. The light transmitted at the first air-glass interface is reflected once more when exiting the sample on the backside, and is also collected by the detector. The measurement area has a rectangular shape of $3 \times 4\,\mathrm{mm}^2$ size. The coating design assumes an angle of incidence of 0° (perpendicular incidence). As this condition cannot be realized by the spectrophotometer, we use the smallest angle available, which is $\alpha = 7°$. Furthermore, we measure the reflectivity from 400 nm to 800 nm, as the design window. As mentioned earlier, about 4% of light are typically reflected at an uncoated air-glass interface. If reflection occurs at both interfaces of the sample, this adds up to ~8%, which is illustrated by the black data in Figure 5.4b, where we measured the reflectivity of an uncoated reference substrate. The blue data points were obtained from a sample where the front (the side facing the light source) was AR coated and the back was uncoated. Here, the spectral dependence of the reflectivity matches the design well, with two local minima and one local maximum. The overall offset of ~4% is caused by the reflection at the uncoated back surface. The data set plotted in red represents a sample where both front and back have an AR coating. Again, the general shape is very similar to the design and the reflectivity is below 1% between 450 nm and 680 nm, covering the main part of the visible spectrum. It is worth noting that the measured signal here is caused by reflections at two interfaces, so the reflectivity of a single surface should be below 0.5% for the stated spectral range, which again emphasizes the good agreement with our design. Apart from the quantitative evaluation, the different reflecting behaviors of substrates with zero, one and two AR coated surfaces is shown in the photograph in the inset. A bright-to-dark transition is reflected by

the samples, and the different contrast between the bright and the dark part is obvious.

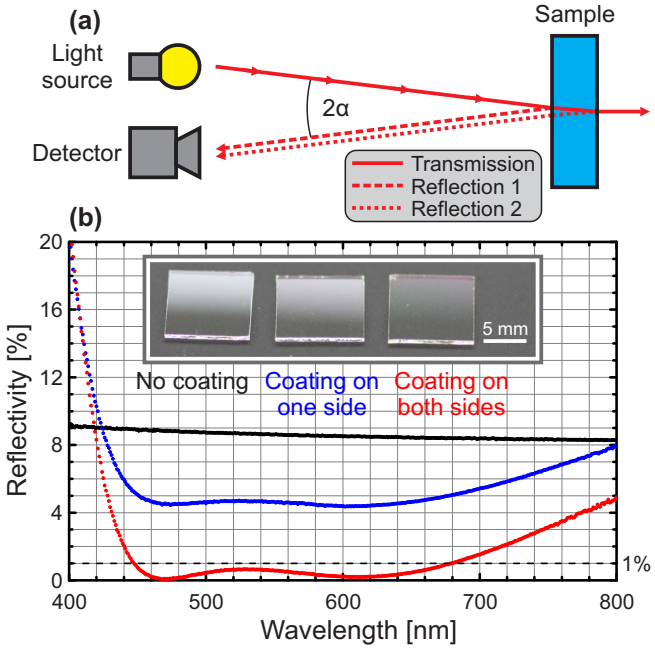

Figure 5.4. Reflectivity measurements of AR coatings on flat glass substrates. **(a)** Measurement principle for reflection experiments. For flat glass substrates light is reflected two times, first at the front and then at the back of the sample. Therefore, an uncoated substrate has a reflectivity of approximately $2 \cdot 4\% = 8\%$. **(b)** Reflectivity measurements of an uncoated glass substrate and substrates with one and two AR coated surfaces. A visual comparison of coated and uncoated substrates is shown in the inset.

The materials used in 3D printed optics are designed to have optical properties similar to glass. However, as they are very different in terms of their chemical composition, they might exhibit a different behavior than glass when they are used as substrate for an AR coating. Therefore, it is necessary to examine the performance of our coatings when they are deposited on 3D printed structures. As the typical diameter of 3D printed lenses is smaller

than 1 mm, their reflectivity cannot be measured using the Cary 7000 spectrophotometer, because the measured area is much larger there. However, spectrophotometry is a very convenient and straightforward way to determine the reflectivity of a sample, therefore we changed the geometry of the 3D printed structure in order to fulfill the requirements for this measuring technique. Instead of printing a sub-millimeter size lens, a thin plate of 30 µm thickness with a size of ~6.5 × 6.5 mm² was printed on an glass substrate. In the next step, the printed plate (and also the surrounding supporting

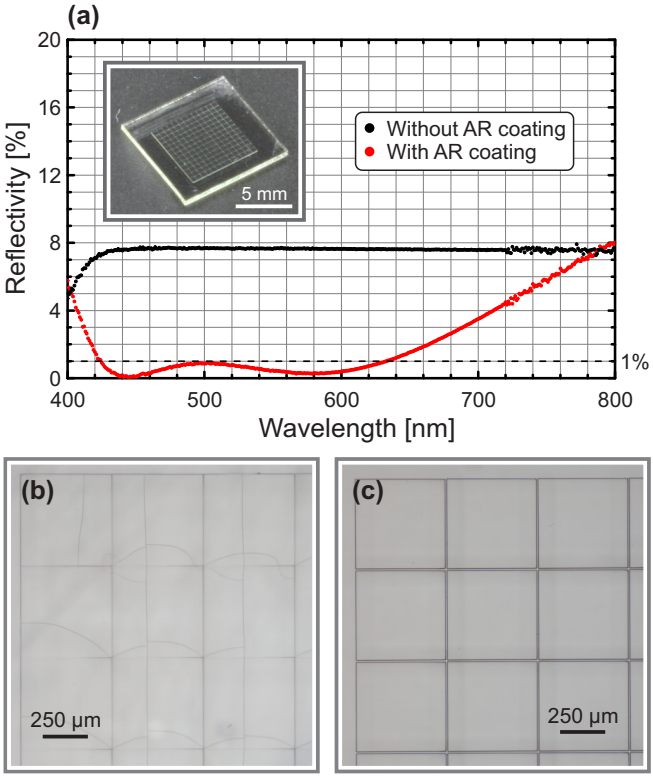

Figure 5.5. AR coating on a large-area 3D printed plate. **(a)** Reflectivity of coated and uncoated 3D printed flat structure shown in the inset. For the coated sample the back of the glass substrate was also coated. **(b)** Microscope image of AR coated 3D printed plate made from 500 × 500 µm² stitching fields with visible cracks in the coating. **(c)** 3D printed plate made from 493 × 493 µm² stitching fields (gaps of 7 µm between adjacent fields) without cracks after ALD coating.

substrate) are AR coated. The back side of the glass substrate was also AR coated, prior to the the fabrication of the plate on the front side. We measure the reflectivity of the sample and the corresponding reference sample, which is also a glass substrate with the 3D printed plate, but without any AR coatings applied. However, as the coated sample is heated to 150 °C for many hours during the ALD process, we also placed the reference sample inside the ALD machine at 150 °C for an equivalent period of time. The spectral reflectivity of both samples is depicted in Figure 5.5a. The reference sample (black data set) has a reflectivity of slightly below 8% between 440 nm and 800 nm which is lower than the reflectivity of the uncoated glass substrate shown in Figure 5.4b. Possible reasons for the reduction are absorption inside the printed structure and scattering at its surface. Photons which are absorbed or scattered do not reach the detector and therefore do not contribute to the measured reflectivity. For wavelengths below 440 nm, the reflectivity decreases significantly. This is attributed to increased absorption and scattering inside the photoresist, which contains molecules designed to absorb light in the UV spectral range, especially around 390 nm. The reflectivity of the AR coated sample (red) again resembles the designed spectral behavior, and the reflectivity is below 1% between 425 nm and 655 nm, demonstrating the compatibility of our coating process with polymer surfaces. The inset in Figure 5.5a shows a photograph of the 3D printed plate on a glass substrate. The visible lines in the plate indicate the boundaries of adjacent stitching fields. As the structure is too large to be printed in one single step, it is composed of smaller structures with $500 \times 500\,\mu m^2$ size. Our Nanoscribe Quantum X microfabrication system was used for 3D printing, the magnification of the focusing objective was 25x and the used material was Nanoscribe IP-S. Initially, the stitching fields were designed with a size of exactly $500 \times 500\,\mu m^2$, as was the periodicity (center-to-center distance of adjacent stitching fields). This way, all the stitching fields were physically connected, resulting in one large structure. Unfortunately, the combination of a large lateral structure size with a very small structure height often results in the delamination of the printed object from the substrate, caused by high internal tension induced by shrinking during and after the printing process. Furthermore, the AR coating applied to such samples has multiple cracks visible in the microscope image in Figure 5.5b, covering the whole 3D printed plate. The reason for this is most likely the difference of the thermal expansion behavior of the polymer and the coating material. When cooling down from 150 °C to ambient temperature, this might induce tensions in the coating, which add up over the whole structure surface and eventually

lead to the formation of cracks. This explanation is supported by the experimental observation that the cracks do not appear if we introduce small gaps between the stitching fields, separating them into individual 3D printed structures. We reduce the size of the stitching fields to 493 × 493 µm² while keeping the periodicity at 500 µm, resulting in gaps of 7 µm width between neighboring fields (Figure 5.5c). This way, we ensure good adhesion to the glass surface without delamination and also avoid crack formation in the coating. While there might still be tension at the polymer-coating interface, this does not add up over a large area, but is restricted to a single field and can distribute evenly there. The area fraction occupied by gaps is below 3%, which is sufficiently low to have negligible influence on the reflectivity measurements.

5.5 TRANSMISSION MEASUREMENTS

Combining the AR coating process with 3D printed structures introduces limitations and requirements into the overall process chain. As stated before, the polymers cannot withstand high temperatures, so the coating process is carried out at 150 °C. Printing speed is also to be considered, the 30 µm thin plate mentioned in the previous section has a printing duration of ~1 h. Therefore, it is unfeasible to 3D print bigger structures, e.g., a 10 × 10 × 0.5 mm³ plate for a direct comparison to a glass substrate of the same size. For the reflectivity measurements, the large size was necessary due to the large spot size of the measurement area, which can be also viewed as a certain limitation in the process chain. In general, when we switch to smaller 3D printed structures with sub-millimeter size, characterizing the applied AR coating becomes more challenging because of the limited choice of measurement techniques. To demonstrate the importance of AR coatings for optical systems with multiple interfaces, we therefore start with a very basic sample geometry designed for transmission measurements. The polymer blocks depicted in Figure 5.6a have flat surfaces, a height of 520 µm and a width of 700 µm. When we shine light along the y-axis onto the blocks, the transmission should be different for the big single block, the set of two blocks and the triple block set, as the number of polymer-air interfaces is different, causing different degrees of reflection losses (Figures 5.6b, 5.6c and 5.6d). The thickness of the biggest block is 300 µm, the two blocks in the middle are each 150 µm thick and the three blocks on the right have a thickness of 100 µm each. This way, the light passes identical distances inside the printed material for each measurement position, so any difference

in the transmission signal can be attributed to effects at the polymer-air interfaces. While we expect reflections to be the main source of reduced transmission, scattering caused be surface roughness might also contribute to a certain degree.

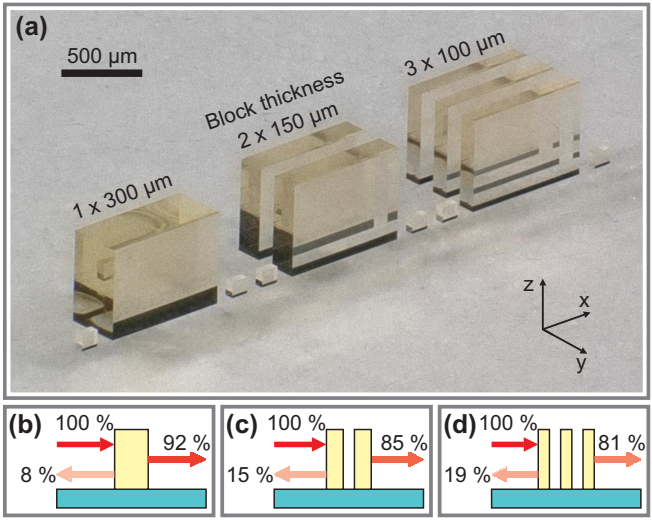

Figure 5.6. Test sample for transmission measurements through 3D printed structures with AR coating. **(a)** 3D printed test structures for transmission experiments. Light passing through the different sets of printed blocks experiences reduced transmission due to reflections at the air-polymer interfaces as well as scattering and absorption inside the printed structures. **(b) - (d)** Illustration of transmitted and reflected light of an uncoated test sample. The thickness of each block set is chosen such that the cumulative optical path length through 3D printed material is 300 µm for each block set. This should ensure equal losses inside the printed structures, so any difference in the transmission through the different block sets can be exclusively attributed to reflection losses caused by the different number of air-polymer interfaces.

5.5.1 *Experimental setup*

The experimental setup for transmission measurements is sketched in Figure 5.7a. Light with a center wavelength of 525 nm is provided by an LED

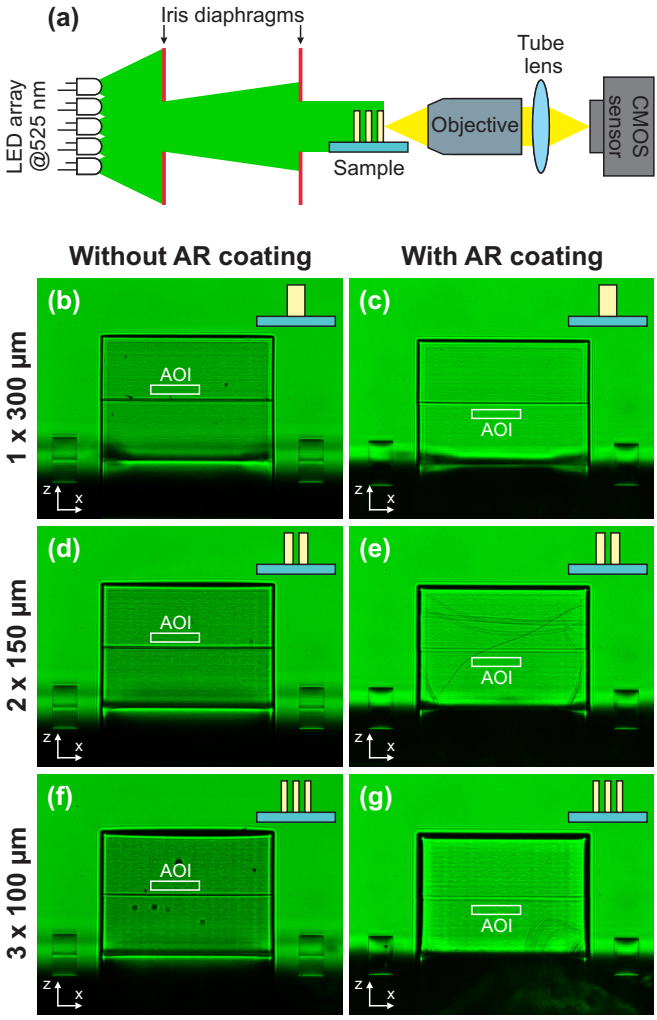

Figure 5.7. Transmission experiments with uncoated and AR coated 3D printed test structures. **(a)** Experimental setup for transmission experiments. The illumination beam path is illustrated in green, the detection beam path in yellow. A large-area LED array at 525 nm is used as light source. Two iris diaphragms positioned 22.5 cm apart from each other are adjusted to a diameter of 2 mm each, in order to achieve normal incidence on the sample. **(b) - (g)** Images of AR coated and uncoated samples. Rectangles indicate the area of interest (AOI) from which the data for the quantitative evaluation was extracted.

array with ~2 cm diameter and a wide angular emission distribution. As the 3D printed structures on the sample are much smaller and because we designed the AR coating for perpendicular incidence, we use two iris diaphragms which are adjusted to a diameter of ~2 mm positioned 22.5 cm from each other to eliminate unwanted angular light components. The light passes through the 3D printed blocks and is partly reflected at each air-polymer interface, reducing the transmission. The detection beam path is a standard microscopy setup consisting of a CMOS sensor, a tube lens and an objective, which is focused on the surface of the closest block. Images of uncoated test structures are shown in Figures 5.7b, 5.7d and 5.7f. In Figure 5.7b the transmission through an uncoated single block with 300 µm thickness is depicted. Compared to the surrounding area, the block appears darker, indicating reduced transmission. This contrast can be seen even better in Figures 5.7d and 5.7f, as there are more reflective interfaces, resulting in lower transmission. The small dark spots which are particularly visible in Figure 5.7f are artifacts of the printing process and can form when the laser is scattered and absorbed by impurities inside the liquid photoresist, leading to local heating and sometimes even micro-explosions [59]. As the block height exceeds the working distance of the printing objective, the lower halves of all the blocks are printed fist, and then the upper halves are added, in order to have all structures in close vicinity. The horizontal line in the images represents the border between lower and upper part. The AR coated counterparts can be seen in Figures 5.7c, 5.7e and 5.7g. While the blocks also appear darker with increasing interface number, the difference in intensity compared to the background is much smaller due to the AR coating. The cracks in the coating in Figure 5.7e are located on the four large block surfaces ($520 \times 700\,\mu m^2$). As discussed earlier, the different thermal expansion behavior of the coating materials and the polymer can result in such cracks. In Figure 5.5 crack formation could be successfully suppressed by dividing the large 3D printed structure into smaller units of $500 \times 500\,\mu m^2$, which is similar to the size of the largest face of the block structures in Figure 5.7. The orientation of the two structures is, however, very different. The 500 x 500 μm^2 plate is only 30 µm thick and is printed directly onto the glass substrate, fixing the size of the printed object there. This most likely also limits the shrinking and deforming potenial of the surface where the AR coating is applied, as it s very close to the fixed glass-polymer interface. For the block structures, the contact area is much smaller, depending on the block thickness. Furthermore, the influence of the fixed glass-polymer interface is reduced by the larger block height. In summary, the block structures are geometrical objects with a comparably large aspect

ratio and small contact area to the glass substrate, which makes them more vulnerable to thermal expansion and thus also to crack formation. This can be partly counteracted by replacing the sharp angled edges by round shapes, reducing possible starting locations for crack formation, and by adding a thin adhesion layer of alumina (Al_2O_3) directly on the polymer surface prior to the fabrication of the actual AR coating [94], but sometimes cracks are formed nonetheless, independent of the block thickness. However, as we do not need the entire block surface for the quantitative evaluation of our transmission measurements, we can simply choose crack-free regions for this, indicated by the rectangles.

5.5.2 *Quantitative evaluation*

For each pixel column in z-direction the mean intensity is calculated. Along the x-axis a moving average algorithm is applied to generate the transmission profiles in Figure 5.8. The transmission through different uncoated block structures is shown in Figure 5.8a. Black data represents the reference measurement, which was realized by removing the sample from the setup, measuring directly the intensity of the illumination at the same position as for the measurements with the sample in place. We calculate the mean value of the intensity along the profile in x-direction and set the resulting value to 100%. Compared to the reference, the transmission through the 3D printed blocks is reduced as block number increases. For the single block with 300 µm thickness the mean transmission drops to 85.3%, for the pair of 150 µm thick blocks to 79.7%, and for the block triplet with 100 µm width only 73.6% of the incident light are transmitted. The curves in Figure 5.8b show the transmission of the corresponding block structures with AR coating. In comparison, the transmission is increased to 96.3%, 92.3% and 90.1% for the respective blocks, clearly emphasizing the performance of our AR coatings. The measured transmission is generally lower than the theoretical predicted value, which is attributed to losses not caused by reflections, e.g., scattering due to surface roughness or absorption inside the printed polymer material.

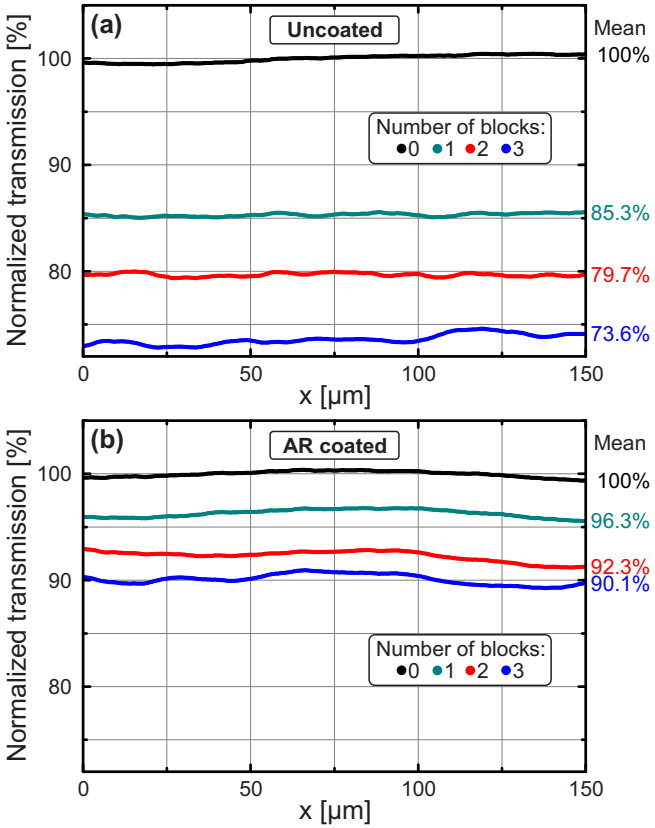

Figure 5.8. Quantitative comparison of transmission through AR coated and uncoated blocks. **(a)** Normalized transmission through different numbers of uncoated polymer blocks at 525 nm. Black data is measured without any 3D printed structure between illumination and detection beam path. **(b)** Normalized transmission through different numbers of AR coated polymer blocks. Compared to the uncoated sample the transmission is increased significantly.

5.6 AR COATED DOUBLET LENS

After the successful fabrication and characterization of our AR coatings on flat surfaces we finally apply the established coating process to a 3D printed two-lens imaging system. The optical design is depicted in Figure 5.9a. The full field of view is 60° for an object located at an infinite distance. The light rays first pass the 500 µm thick glass substrate which supports the 3D printed lenses. The first smaller lens is printed directly on the substrate and has a single curved surface with a diameter of 140 µm. We add a flat ring with 30 µm width around the lens which serves as reference for shape analysis. The curved lens area is also the aperture stop in the optical design, which is realized by adjusting the illumination conditions in the following imaging experiment. The flat bottom surface of the second bigger lens is situated 190 µm above the center of the curved surface of the lower lens. The lens diameter is 517 µm. To facilitate characterization of the surface we also add a flat ring with 42 µm width around the lens. As the lens is not connected to the substrate or the lower lens, we design supporting structures visible in the microscope image in Figure 5.9b. The diameter of the entire 3D printed structure is 600 µm and the height is 437 µm. For the fabrication of the AR coated lens we first apply an AR coating to one side of a glass substrate. Then we 3D print the imaging system on the opposite side of the substrate and finally use another coating run to apply AR coatings to all lens surfaces simultaneously. The lenses were again fabricated with our Nanoscribe Quantum X system, using a 25x objective and Nanoscribe IP-S photoresist. The printing process is separated into three steps. First, the position of the glass-resist interface is determined by the automatic interface finding algorithm. The result is recorded for the subsequent printing steps. Then the first smaller lens is printed using the 2.5D grayscale printing mode of the Quantum X. Next, the supporting structure for the big upper lens is printed, using the 3D printing mode. As the already printed first lens might interfere with the automatic interface finding, the glass-resist interface is moved back to the focal plane of the laser manually. After the printing of the supporting structure is finished, the upper lens is printed directly on top without any further interface finding or movement of the substrate, using the 2.5D grayscale printing mode. At that time, this printing mode was designed to fabricate lenses which are printed directly on a substrate and have only a single optically active surface. Therefore, the bottom surface of the big upper lens is not curved, but flat. The geometry of the doublet lens system emphasizes the challenge of applying AR coatings to 3D printed multi-lens systems. While the top surface of the big upper lens can be coated

using various standard (directional) fabrication techniques, the other optical surfaces, namely the flat bottom surface of the top lens and the surface of the lower lens cannot be reached by coating material applied via a directional fabrication method, as the upper lens and the supporting structures limit the access to those surfaces. Therefore, a non-directional process is required for such multi-lens systems.

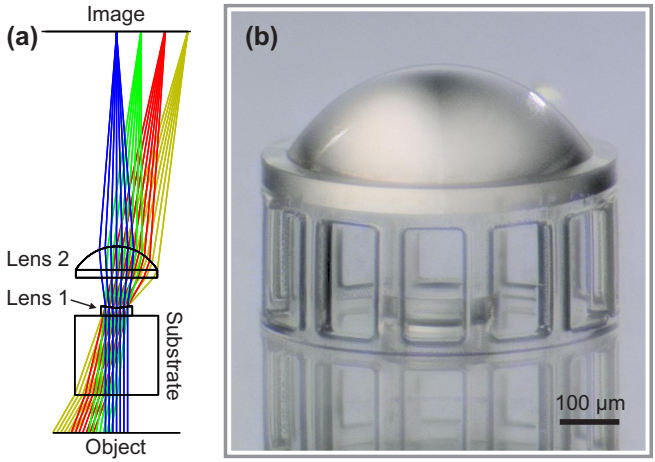

Figure 5.9. Doublet lens for AR coating experiments. **(a)** Optical design of doublet imaging system, including the glass substrate. **(b)** Tilted microscope image of the imaging system with supporting structures for bigger lens.

We use the microscopy setup described earlier [27] to compare images of a 1951 USAF resolution test target viewed by an uncoated and an AR coated lens (Figures 5.10a and 5.10b). For both lenses identical illumination conditions were used. The general imaging quality is very similar, the dark and bright lines can be distinguished with the naked eye up to element 1 of group 3 in both images. The image taken with the AR coated lens looks slightly brighter overall. This is in particular visible when looking at the bright square between element 2 of group 0 and element 1 of group 1. For a quantitative analysis, we extracted intensity profiles along the red line through element 1 of group 0 and compare them in Figure 5.10c. The black curve represents the uncoated lens and the red curve is associated with the AR coated lens. The transmitted intensity is in general higher for the

coated lens, proving the functionality of our coating in combination with a multi-lens imaging system. If we multiply the black curve by a factor of 1.2, the resulting black dotted curve coincides well with the red curve, especially in the region of the central intensity maximum. This indicates an increase in transmission of ~20%, which is a significant improvement for many optical systems. Particularly when short exposure times are required or under low-light illumination conditions this can make an important difference.

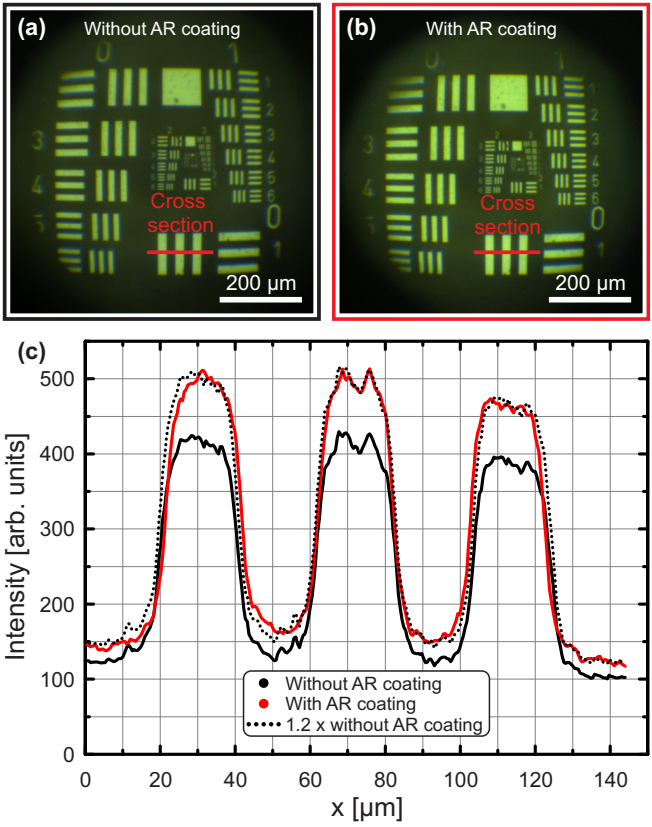

FIGURE 5.10. Imaging quality of uncoated and AR coated doublet imaging systems. **(a)** USAF 1951 resolution test target imaged by uncoated lens. **(b)** USAF 1951 resolution test target imaged by AR coated lens. **(c)** Intensity profiles extracted along the red line in **(a)** and **(b)**.

For the sake of completeness the influence of the AR coating on the imaging contrast should be discussed at this point, as this is closely related to typical resolution test targets such as the 1951 USAF target used here. The resolution of an imaging system is often quantified by the element and group number of the structure with the smallest line width for which the modulation between bright and dark stripes is bigger than a certain threshold value (typically 10%). For test structures consisting of similar portions of bright and dark areas the modulation is usually defined by the Michelson contrast

$$C_M = \frac{I_{max} - I_{min}}{I_{max} + I_{min}} \tag{5.1}$$

where I_{max} and I_{min} are the intensities at the three local maxima and at the two local internal minima of the profiles [95]. For $I_{max} = I_{min}$ the contrast is 0, and for $I_{min} = 0$ the contrast has a maximum value of 1. The influence of the AR coating can be expressed by simply multiplying both I_{max} and I_{min} with a factor of 1.2, which effectively does not change the contrast. The benefit of the AR coating is therefore not an increased contrast here, but rather an increased overall transmission and the potential reduction of imaging artifacts, e.g., ghost images and flares.

5.7 CONCLUSION

In conclusion, we have demonstrated the fabrication of anti-reflective coatings on 3D printed polymer structures by atomic layer deposition, which is a conformal coating process and therefore enables the single-step formation of AR coatings on every surface of a complex micro-optical system, including undercuts and hollow cavities. First, AR coatings were fabricated on standard glass substrates for characterization with a commercial spectrophotometer. The residual reflectivity was below 1% for the main part of the visible wavelength spectrum. Measurements with an AR coated 3D printed large-area plate resulted in similar behavior, hinting sufficient robustness of the process when switching the substrate material. Next, the coatings were deposited on different 3D printed polymer blocks, which are designed for transmission measurements. Here, the different numbers of polymer-air interfaces resulted in different amounts of reflection losses. The AR coated structure with six interfaces has ~90% transmission compared to ~74% for the uncoated reference sample, illustrating the importance of AR coatings for multi-lens applications. Finally, we compared the imaging quality of

an uncoated and an AR coated 3D printed double-lens system, resulting in an increase of ~20% in the overall transmitted intensity. For applications where the amount of accessible illumination light or the exposure time of a camera sensor is limited this is particularly interesting. To make use of the full potential of our coating process, we will combine our AR coatings with more complex optical systems consisting of more than two lenses in the future, using advanced coating designs with more layers, resulting in even lower reflection losses for designated wavelengths.

6

MASS-PRODUCIBLE DIFFRACTIVE OPTICAL ELEMENTS

While 3D printing is a superior fabrication technique for micro-optics in terms of design freedom, shape accuracy and alignment of multi-lens optics, the comparably slow printing speed limits the use for large-scale production. Particularly when the optical element is not too complex, e.g., if it contains only one structured (curved) surface, the fabrication of a highly accurate master in combination with replication methods such as injection molding makes large-scale manufacturing very convenient. Here, we present the mass production compatible fabrication of polymer-based micro Fresnel lenses by injection compression molding. The extremely robust titanium molding tool is structured with high precision by focused ion beam milling. In order to achieve optimal shape accuracy in the titanium we use an iterative design optimization. The inverse Fresnel lens structured into the titanium is transferred to polymers by injection compression molding, enabling rapid mass replication. We show that the optical performance of the molded diffractive Fresnel lenses is in good agreement with simulations, rendering our approach suitable for applications that require compact and high-quality optical elements in large numbers.

This chapter is mostly based on the following publication:

S. Ristok, M. Roeder, S. Thiele, M. Hentschel, T. Guenther, A. Zimmermann, A. M. Herkommer, and H. Giessen
"**Mass-producible micro-optical elements by injection compression molding and focused ion beam structured titanium molding tools**",
Optics Letters **45**, 1184-1187 (2020),
DOI 10.1364/OL.385599.

6.1 INTRODUCTION

Injection molded polymers are the material of choice for micro-optics used in mass-producible devices such as smartphones or optical sensors [96–98]. Hundreds of millions of such micro-optical elements are manufactured every year using a so-called LIGA process (German "Lithographie, Galvanoformung, Abformung") in which a silicon (Si) master is fabricated by gray-scale electron beam lithography and subsequent etching. An electroplating process is then used to transfer the structured Si surface into a solid nickel (Ni) shim, which serves as the mold in the following replication step. Techniques like injection (compression) molding [99–101], hot embossing [102], or nanoimprint lithography [103–105] are commonly used for the replication in polymers [106, 107]. In total, two inversion steps are necessary to transfer the structure from the Si master to a plastic polymer part. For injection molding, a polymer is heated, injected into the Ni shim, pressurized, and released. A Ni shim usually lasts for about 10,000 repetitions before it has to be replaced. Coating the Ni shim with a hard material such as titanium nitride (TiN) can increase the repetition number before failure [108]. An alternative method to fabricate micro-optical elements is nanoimprint lithography. However, this method also requires two inversion steps, as well as photopolymers that react to UV light. This can easily leave a yellowish hue in the micro-optics due to the residual photoinitiator [66] and might render the plastic devices prone to degradation and aging.

Here, we introduce an alternative method that requires only a single inversion step and works with clear plastics without photoinitiator, avoiding a UV curing step. A non-magnetic titanium master (Ti-6Al-4V Grade 5) is structured directly using focused ion beam (FIB) milling [109] and is subsequently used as mold insert for injection compression molding. While the surface quality should be similar to structures fabricated with the commonly used electroplated Ni shims, Titanium (Ti), as extremely hard material, should minimize the wear from the molding step, resulting in a large number of replications before it needs to be replaced. We make use of the fact that FIB milling is an intrinsic "gray-scale process" with potentially thousands of levels, as the material etch rate depends directly on the ion dose (in contrast to the UV and electron beam gray-scale lithography). We demonstrate the manufacturing and the characterization of the Ti mold insert and show the imaging performance of diffractive Fresnel lenses made by injection compression molding. As Fresnel lenses are often used in various micro-optical applications [110–112], they are well suited to point out the benefits and the

limitations of the fabrication process. The lenses have a diameter of 100 µm, a focal length of 200 µm, and are designed for a target wavelength of 550 nm.

6.2 FABRICATION AND REPLICATION

The fabrication process is outlined in Figure 6.1. First, the inverse profile of the Fresnel lens is milled by a focused beam of singly charged Gold (Au+) ions (Figure 6.1a) into the Ti mold insert polished to optical quality. To avoid drift due to thermal expansion, it is transferred into the vacuum chamber of the FIB machine (Raith ionLine Plus) 24 h prior to the actual structuring process. The ion dose is not deposited in a single step, but in ~130 successive structuring cycles to avoid nonlinear milling effects. During each cycle, the ion beam is scanned in concentric circles of increasing diameter over the Ti surface in order to prevent directionally dependent deviations. As the diameter of the structure is 100 µm, and its maximum depth is around 1 µm, the volume which has to be removed by FIB milling is comparably large, resulting in a structuring duration of ~24 h. The comparably long structuring times are also related to the high resolution and form accuracy afforded by

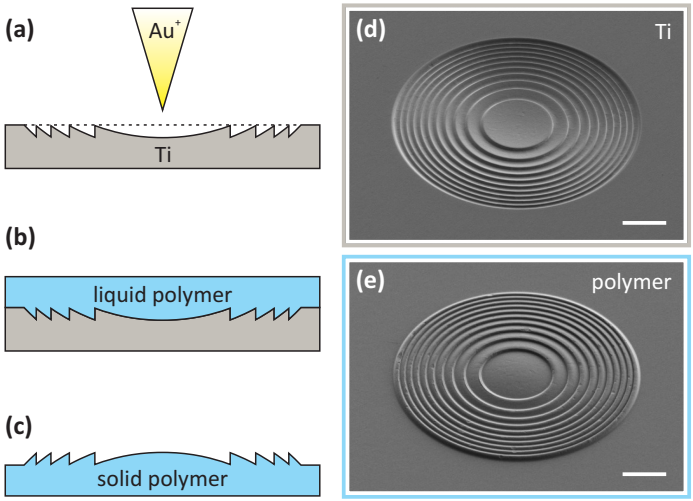

FIGURE 6.1. Workflow diagram for the fabrication of Fresnel lenses. **(a)** FIB structuring of inverse geometry in Ti. **(b)** Injection compression molding in transparent polymer. **(c)** Solid polymer Fresnel lens. **(d)** and **(e)** SEM images of Ti mold insert and polymer Fresnel lens. Scalebars: 20 µm.

our method. Larger diameters and deeper features are possible, if longer fabrication times can be accepted.

In the next step the structures milled into the Ti surface are replicated in polymers by injection compression molding (Figure 6.1b). The Ti mold insert is integrated into an injection compression molding tool, into which the plasticized polymer Zeonex 330R is injected. After the polymer has cooled and solidified, the molded sample can be removed and characterized (Figure 6.1c). The scanning electron microscope (SEM) images of the structured Ti surface and the molded polymer Fresnel lens are shown in Figures 6.1d and 6.1e.

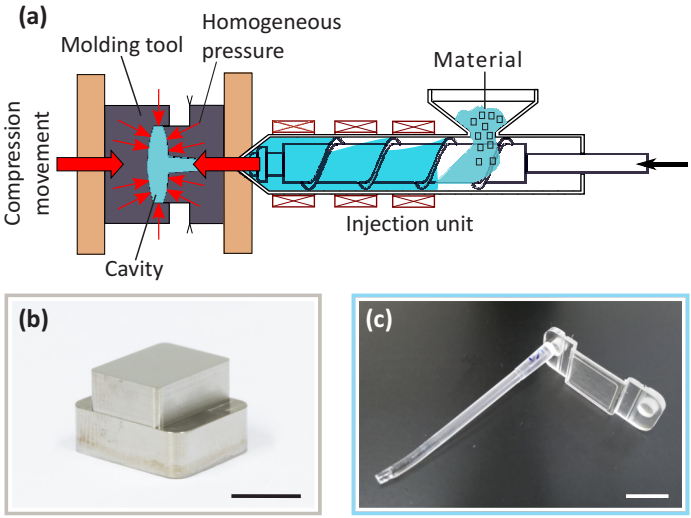

Figure 6.2. Injection compression molding setup for Fresnel lens replication. **(a)** Fabrication setup. **(b)** Ti molding tool. **(c)** Polymer part after molding. Scalebars: 1 cm.

The injection molding process is illustrated in more detail in Figure 6.2a. The transparent polymer is heated to 255 °C and injected into the molding cavity, which is preheated to 120 °C. The injection pressure is 1500 bar. Unlike in classical injection molding, the molding tool is initially not closed completely during the injection phase. With a defined delay after the material injection, a movable compression stamper in the molding tool is used to

shape the molded part into its final dimensions. Pressure applied this way is very homogeneous throughout the entire cavity. Therefore, less residual stress remains within the solid plastic part, resulting in reduced birefringence compared to parts made by the standard injection molding [113]. Less birefringence, in turn, usually leads to superior imaging properties. The time needed for one replication is 26 s. A photograph of the used Ti mold insert is shown in Figure 6.2b. The inverse Fresnel lenses are milled into the polished surface on top. After the molding process, the sample is prepared for further characterization by removing the excess plastic parts, as visible in Figure 6.2c. The resulting part has a thickness of 900 µm and measures $1.3 \times 1.3\,\mathrm{cm}^2$. No further post-process treatment is required, and the sample can directly be examined by optical microscopy and atomic force microscopy (AFM) to verify the quality of the replication process.

6.3 SHAPE OPTIMIZATION

An essential prerequisite for the shape accuracy of the injection molded structures is the shape accuracy of the inverse structures milled into the Ti molding tool. Therefore, we examine the Ti mold insert after FIB milling with a confocal microscopy technique (Nanofocus µsurf expert) to measure the profile of the inverse Fresnel lens and characterize and improve the fabrication results.

As a first step, we mill the target design, assuming a one-to-one correspondence between deposited dose and milled structure depth, into the Ti mold insert. The profile in Figure 6.3a indicates that the depth of the central part is 1.11 µm, which is close to the design depth of 1.18 µm. However, the height difference between the adjacent peaks and valleys is significantly reduced towards the outer boundary of the lens. Possible reasons are the finite beam size and defocusing due to the significant depth of the structure [114]. The steps are most critical features in the diffractive Fresnel lens design as regions with maximum and zero ion doses are in direct vicinity of each other. If the size of the ion beam is too large, part of the high dose might impinge on the region where no dose is supposed to go, reducing the step height and rounding the sharp edge of the step. Furthermore, the ion beam is initially focused at the top of the Ti surface and is not refocused when milling into deeper lying regions. This could lead to defocusing with increasing depth, resulting in a reduced milling rate and therefore causing deviations from the designed depth and shape. It is, however, challenging to determine how these different effects impact the milling process quantitatively. For this

reason, we refrain from tuning the process parameters (e.g., focusing or beam size). Instead, we incorporate the measured deviations into the milling design to iteratively approach the target design in the Ti mold insert. The original and optimized designs are displayed in Figure 6.3b. In the original design the step height is constant over the entire profile. Deviations visible in Figure 6.3a are evaluated and used to generate the optimized structuring design. The radial positions and height values of the minima and maxima are extracted. We use linear fits to calculate the slopes, which describe the behavior of the minima and maxima separately. For the maxima, the first peak at the border of the central spherical region serves as reference point, where the deviation is set to zero. For the minima, the depth in the center is used as reference point. The deviations at the step positions are calculated and added to the original design, resulting in an increase of the step height towards the outer parts of the structure.

The optimized design is FIB milled into the Ti molding tool, and the profile is measured with atomic force microscopy (Veeco Dimension Icon, AFM probe: Tap300Al-G (BudgetSensors)) (Figure 6.3c). The profile is mirrored horizontally to facilitate comparison with the profile of the molded polymer lens, plotted in black. Compared to Figure 6.3a the decrease of the step height is strongly reduced. Generally, the milled structure is very close to the ideal Fresnel lens design. The rounded edges are, however, still visible. Another optimization step where the shape of each segment of the Fresnel lens is measured and optimized separately could help to minimize this effect.

In the next step, we compare the quality and the shape accuracy of the polymer replication process. The profile of the replicated polymer lens, again determined by AFM measurement, is shown in red in Figure 6.3c. In the central part, the agreement between the mold insert and the molded lens is good, whereas some smaller deviations can be seen for the finer structures in the outer parts. We attribute this mainly to the shrinkage of the polymer during the cooldown. Both profiles are taken from the AFM measurements shown in Figures 6.3d and 6.3e.

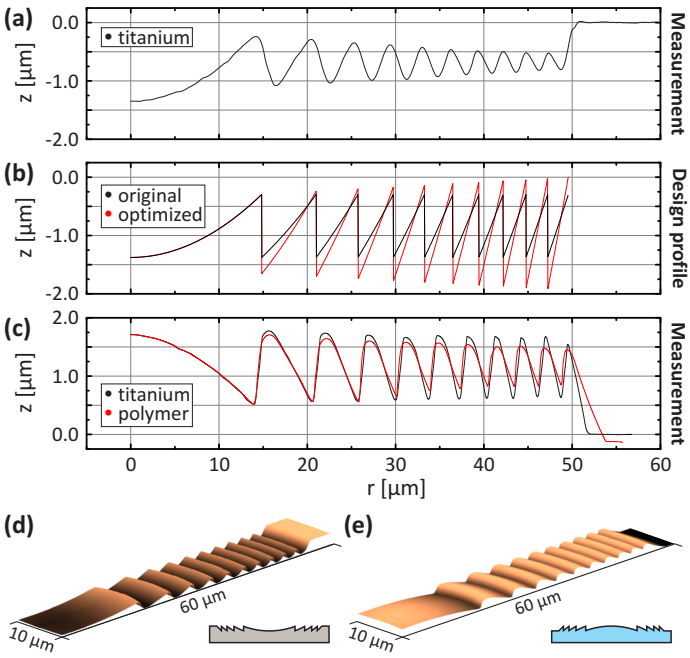

Figure 6.3. Shape accuracy measurements of titanium mold insert and replicated polymer Fresnel lens. **(a)** Profile of inverse Fresnel lens on Ti mold insert. **(b)** Original and optimized design profile. **(c)** Comparison of optimized profile in Ti and polymer. **(d)** and **(e)** AFM measurements of Ti mold insert and polymer Fresnel lens.

6.4 IMAGING CHARACTERIZATION

While high shape accuracy is a suitable indicator for the quality of the molded Fresnel lenses, their optical performance is ultimately the most important benchmark. An overview of the optical setup used to characterize the imaging properties is shown in Figure 6.4. A LED white light source is used for illumination. The light is collimated and then sent through a 550 nm filter ($\Delta\lambda = 40$ nm), as this is the wavelength that the diffractive Fresnel lens is designed for. Homogeneous radiant intensity is achieved by using a diffuser plate. An inverse USAF 1951 resolution test target is used as a test object. The light is focused onto the Fresnel lens by a microscope objective and the resolution test target is placed between the objective and the Fresnel lens. The imaging plane of the Fresnel lens is viewed by a standard microscopy setup (objective, tube lens and CMOS sensor). To

minimize unwanted stray light, an adjustable iris diaphragm is added to the illumination and placed between the light source and the objective. The exact position is chosen such that an image of the iris is projected onto the Fresnel lens. The size of the iris is then adjusted to match the diameter of the lens, which has the same effect as a physical aperture.

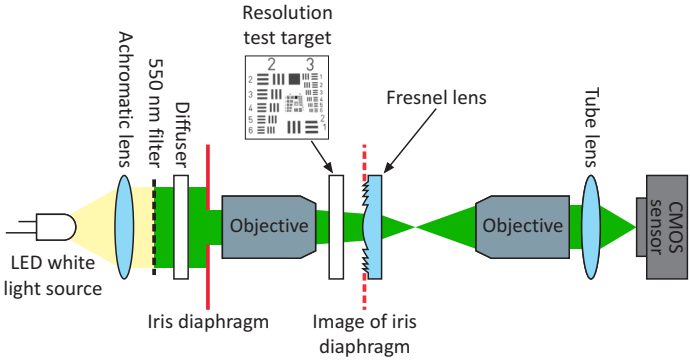

Figure 6.4. Optical setup for imaging characterization of Fresnel lenses.

In Figure 6.5 the experimental imaging quality is compared to the simulations. Figures 6.5a - 6.5c show the resolution test target imaged by the replicated Fresnel lens using monochromatic illumination. The distance between the target and the Fresnel lens is varied (5.25 mm, 1.75 mm, 0.75 mm) to determine the smallest visible features. To facilitate the evaluation by the reader, the contrast of the images was subsequently enhanced. In addition, we simulate the imaging performance of the ideal diffractive Fresnel lens design for the different object distances using the built-in "Image Simulation" tool of the raytracing software ZEMAX 13 (Figures 6.5d - 6.5f). In Figure 6.5a, the image of group 2 and group 3 of the test target is shown. A barrel distortion is present both in the measurement and in the simulation. Figure 6.5b shows group 4 and group 5, with the smaller group 6 and group 7 in the center. There is good agreement between the experiment and the simulation for the imaging of group 4 and group 5. While all the elements of group 6 can be distinguished in the simulation, this is only possible up to element 2 in the measurement. When the target is placed very close (0.75 mm, Figure 6.1c) to the lens, group 6 and group 7 can be distinguished, which indicates a resolution down to 2.5 µm, which can be expected from our 0.24 NA Fresnel

lens design at 550 nm. The imaging quality is similar for the experiment and the simulation, but there is some slight mismatch in magnification.

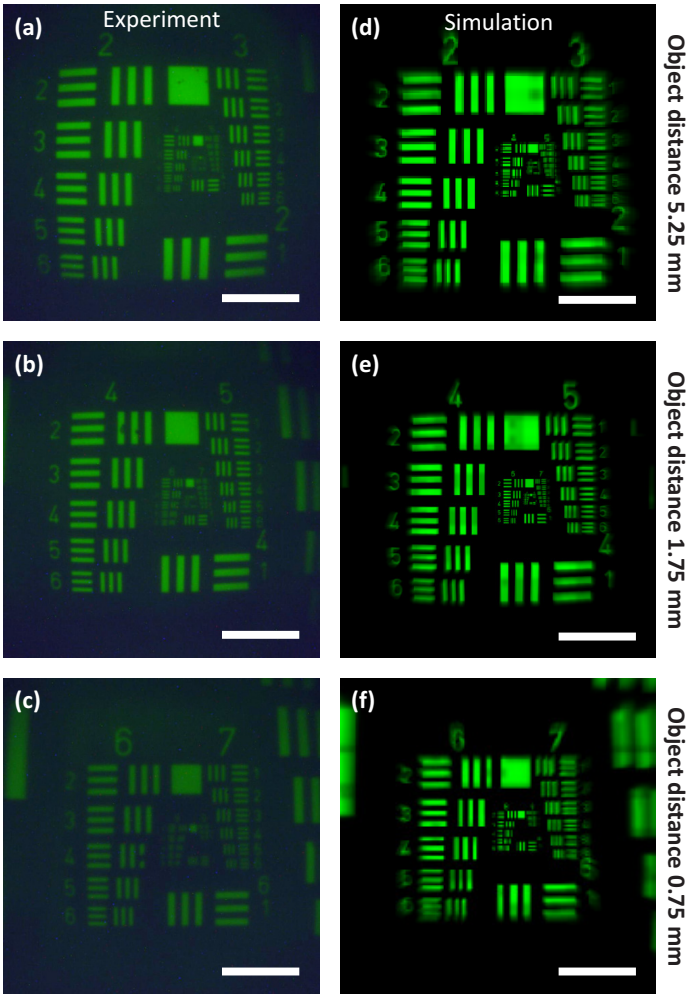

Figure 6.5. Measured and simulated images of USAF 1951 test target for distances 5.25, 1.75 and 0.75 mm from the Fresnel lens. Measurements are shown in **(a) - (c)** and simulations in **(d) - (f)**. Scalebars: 50 µm.

6.5 CONCLUSION

In conclusion, we have presented an alternative approach for the fabrication of a master for mass replication of micro-optical elements. The Ti master was structured directly by FIB milling, avoiding the necessity of a second inversion step. We used the measured profile of the milled Fresnel lens to iteratively optimize the structuring process. After the optimization, the Ti master was used as mold insert for injection compression molding. The AFM measurements confirmed the good agreement of the inverse Fresnel lens in the molding tool and the replicated polymer lens, with some minor deviations. Those deviations could most probably be reduced by optimizing the injection compression molding process, e.g., by using a hot runner system and a variothermal mold temperature control [100]. The imaging performance of the diffractive Fresnel lenses was demonstrated using a standard resolution test target. In contrast to the standard mold fabrication processes, such as diamond turning, FIB milling offers a multitude of degrees of freedom in the optical design. It is thus very intriguing to use the described fabrication process for the realization of advanced optical designs, e.g., aspheric Fresnel lenses or non-rotationally symmetric free-form geometries. We envision the use of this technique also for more complex polymer optics in combination of refractive and diffractive components [115, 116].

7

CONCLUSION

In this thesis, different microfabrication techniques were investigated and combined, in order to realize high-quality, complex optical elements. A key goal was to increase the diameter of 3D printed micro-lenses to ~500 µm diameter, matching the requirements of specialized endoscopic applications and miniaturized optical sensors. This was demonstrated by the fabrication of multiple doublet objectives designed for imaging applications. The objectives feature a high imaging quality due to their four aspheric lens surfaces, which were optimized by an iterative process. The surface shape was analyzed by confocal microscopy and the shape deviation was precompensated in the optical design. The adapted design was printed and analyzed again, and this cycle was repeated until the shape deviations were sufficiently small. The optimization process significantly improved the imaging quality, rendering the printed objectives ready for prototype fabrication in combination with other optical components. First, doublet objectives were printed directly onto imaging fiber bundles with 500 µm diameter, forming the prototype of an endoscopic device. The quality of the image transmitted through the fiber was mainly limited by the coarse size of the individual fiber cores. We investigated ways to change the direction of view from 0° to 90°, which is necessary for many endoscopic applications. While the first approach based on total internal reflection in a solid prism worked in principle, a hollow prism-like structure coated with a metallic reflecting layer is independent of the angle of incidence on the reflecting surface, resulting in more design freedom. Apart from the fiber-based endoscope prototype, 3D printing was also demonstrated on a distal chip endoscopic system, but this topic was not pursued further. Instead, camera sensors of a Raspberry Pi camera were used as substrate for the fabrication of doublet objectives. The printing parameters had to be adapted to avoid micro-explosions caused by increased reflections and absorption at the sensor surface. In general, the

fabrication on camera sensors is very similar to standard glass substrates. Different optical designs for infinite and finite object distance were printed on sensors and their imaging quality was evaluated to be sufficient for tasks like gesture recognition. To counteract the increase in printing duration caused by the larger lens diameter, we investigated a two-step core-shell fabrication process. The inner part of the lens (core) is printed with coarse slicing and hatching parameters, resulting in high printing speed. Then, the outer shell of the lens is printed again with high-resolution printing parameters and a customized laser scanning trajectory. This way, a 25% reduction of the printing time was achieved, while maintaining a high imaging quality comparable to a lens printed entirely with the high resolution parameters.

In an attempt to bridge the size gap between 3D printed and commercial lenses, we combined a new printing objective with a larger writing field with a new printing material with superior transparency. This setup enables the fabrication of lenses with up to 2 mm diameter. The well-known yellowish hue caused by residual photoinitiator in the standard printing materials was reduced to a minimum by the introduction of the new material. An optimized aspheric lens with 1 mm diameter was able to focus light from a green laser into a spot with $< 1\,\mu m$ beam radius, in good agreement with simulations. Comparing a printed half-ball lens with 1 mm diameter to an identically shaped lens made from glass, both showed comparable imaging quality. The modulation transfer functions of a commercial glass lens with 2 mm diameter and an identical printed lens were compared, with similar results for both lenses. However, the printed lens had delaminated partly from the underlying substrate, which might have influenced the measurements. Delamination is not unusual for large contact areas between printed structure and substrate. By spin-coating and curing a thin layer of SU-8 photoresist on the substrate surface before 3D printing, this issue could be minimized. The same photoresist was also used for a post-process surface smoothing treatment, during which a thin layer of SU-8 is applied to the lens, reducing the staircasing effect and increasing the conformity of design and printed lens.

For optical systems with multiple lens-air interfaces, the overall transmission is reduced due to the reflection losses at each interface. Anti-reflective coatings are therefore added to high-quality lenses before they are assembled into a multi-lens system. As we have seen in Chapter 3, multi-lens micro-optics can be fabricated in a single 3D printing process. To add AR coatings to such lens systems, the standard directional coating techniques cannot be used, as the undercuts and the inner surfaces of the hollow parts

will not be coated. Therefore, we introduced an atomic layer deposition process which can apply the coating material to every surface of a printed multi-lens system simultaneously. In order to prevent thermal damage to the printed polymer lenses, the process temperature was reduced to 150 °C. Using four alternating layers of high and low refractive index materials, the coating with an overall thickness of ~200 nm was first applied to flat glass substrates for characterization and optimization purposes. Reflectivity measurements confirmed good agreement with simulations. Next, the coating was deposited on a 3D printed flat surface. Again, a reflectivity < 1% was measured throughout the main part of the visible wavelength spectrum. To test the influence of AR coatings in structures with multiple interfaces we switched to transmission experiments. Coated and uncoated 3D printed test structures with varying number of interfaces were compared. The transmission through six air-polymer interfaces was increased from ~74% to ~90%. Residual deviations from the theoretical prediction are attributed to absorption in the printed structures and to scattering induced by surface roughness. Finally, the coating was applied to a doublet imaging system, increasing the overall transmission by 20%.

While 3D printing offers huge freedom in optical design, it is not the ideal fabrication method for every micro-optical structure. Especially when large numbers of optical elements with a single optical surface are required, fast reproduction techniques such as injection compression molding are a better solution. The molding tool with the inverse optical geometry is normally made by nickel electroplating on a master structure, which has to be fabricated with high precision. We demonstrated a new fabrication method for a molding tool made from titanium, using direct focused ion beam structuring without the need of an additional master, simplifying the process and reducing the susceptibility to errors. An optical design for a Fresnel lens with maximum height of ~1 µm and 100 µm diameter was conceived and the inverse geometry was FIB milled into a titanium block. Using advanced milling strategies in combination with iterative shape analysis and design adaption, the agreement between design and FIB milled structure was optimized. The injection compression molding process induces only minor deviations between the shape of the molded polymer Fresnel lenses and the titanium molding tool. We find the imaging quality of the Fresnel lenses close to simulations, utilizing a standard USAF 1951 resolution test target.

As 3D printing by two-photon polymerization is a very powerful and versatile fabrication technique, its use is not restricted to optics, but covers

a wide range of topics, e.g., micro-fluidics and biomedical applications. The advances presented in this thesis have contributed to the available toolbox of microfabrication techniques for optical elements, but could also be transferred to other fields. Combining the 3D printed micro-optical elements demonstrated in this work with 3D printed structures from other fields could lead to cutting-edge innovative devices and novel intriguing research topics.

8

OUTLOOK

The results obtained in the course of this thesis inspired many ideas for future research in this field, which might either be direct follow-ups of the presented work or introduce completely new concepts.

Concerning the surface quality of 3D printed optical components, the introduction of the Nanoscribe Quantum X system was a milestone. The structures printed with its 2GL mode show nearly no visible staircasing effect. At the moment, this printing mode is limited to 2.5D, but this might change in the future, enabling the reproduction of the doublet objectives from Chapter 3 with superior surface quality. Regarding the endoscopic applications of the doublet objectives, an illumination system is usually required here. Typically, light-guiding fibers are arranged around the imaging fiber bundle, but 3D printing could also enable the realization of a combined illumination and imaging system, where part of the imaging fiber is used to transmit the illumination light.

The combination of doublet objectives and camera sensors could be improved by covering the entire sensor surface with an array of objectives. If identical objectives are used, this would increase the signal strength and widen the total field of view. If objectives with different optical properties are used, applications like foveated imaging [61] or multi-aperture cameras [117] could be realized in video mode. In both cases, the images of the individual objectives have to be aligned and combined. Performing this task manually is rather cumbersome, instead, new approaches such as self-learning algorithms using artificial intelligence could be applied.

Micro-optics at the presented size scale might also be interesting for the rapidly growing field of augmented and virtual reality applications. For devices such as smart goggles a high degree of miniaturization and

integration is demanded, which could be achieved by customized 3D printed optics.

In order to increase the size of 3D printed objects even more, a new printing objective was recently announced by Nanoscribe. It has a magnification of 5x and a printing field diameter of 3.2 mm [118].

In an ongoing project, the Nanoscribe PPGT system is extended by a hexapod, which can translate the substrate in all three dimensions and additionally provides two rotational axes. With this setup, we will be able to remove residual substrate tilt and gain the capability of printing on strongly curved surfaces.

Our anti-reflective coatings will be adapted to different requirements, e.g., the lowest possible reflectivity at a specific wavelength. Coating designs with a higher layer count can reduce reflections even more, and other coating types such as high-reflective coatings or optical filters can also be deposited.

The fabrication of master structures for injection compression molding by focused ion beam milling is also developed further. It is particularly interesting for multi-level diffractive optical elements, as the level height can be adjusted directly via the ion dose.

Although it is not completely new, 3D printing by two-photon polymerization is still a very vibrant field, because completely new fields of application, such as mechanical metamaterials [119], continue to emerge. In a recent publication, Hahn et al. proposed a new absorption scheme for two-photon polymerization, which uses CW laser light instead of femtosecond pulses [120]. As the femtosecond laser is one of the most advanced components in the 3D printer, systems based on this new technique might be significantly cheaper, and thus easily accessible to a broader community, accelerating the evolution of this field even more.

A

LIST OF AVAILABLE FOCUSING OBJECTIVES

When the focusing objectives are mentioned in the main text, they are referred to by their magnification. The two 25x objectives have different working distances, the one with the long working distance (LWD) is referred to as the 25x LWD objective. The 63x, 25x and 10x objectives are covered by the Nanoscribe support, as they belong to the PPGT system. As both the 63x and the 25x objective are Zeiss products, it seemed plausible that other Zeiss objectives with similar properties can also be used, which is the case for the 25x LWD objective. We state the serial numbers of the Zeiss objective catalog for further technical details on the different objectives. The Nanoscribe Quantum X system has its own set of objectives (63x, 25x and 10x). The optical parameters are identical to the objectives used with the Nanoscribe PPGT system, although the geometry of the 25x objective was changed, and it therefore has a new serial number (420852-9973-710). As the 25x LWD objective is not an official Nanoscribe product, it was so far not used with the Quantum X.

Objective	**63x**	**25x**	**25x LWD**	**10x**
Zeiss serial number	420782 -9900-799	420852 -9972-710	420852 -9871	-
Magnification	63x	25x	25x	10x
Numerical aperture	1.4	0.8	0.8	0.3
Working distance	380 µm	380 µm	740 µm	700 µm
Maximum writing field diameter	400 µm	800 µm	720 µm	2 mm

Table A.1. Focusing objectives used with the Nanoscribe PPGT system.

B

FABRICATION PARAMETERS FOR 3D PRINTING

NANOSCRIBE PPGT

The fabrication parameters for structures printed with the Nanoscribe PPGT system are summarized here, and the parameters are briefly introduced:

Objective indicates which focusing objective was used, identifying the specific objective by its magnification.

Substrate denotes the type of the supporting substrate for the printed objects, e.g., a glass coverslip, imaging fiber bundle or camera sensor.

Photoresist states the printing material, which is either Nanoscribe IP-S or Nanoscribe IP-Visio.

Laser power is given as a percentage of a defined reference value, explained in detail in Chapter 2.

Scan speed quantifies the speed at which the laser focus is moved through the photoresist by the two galvo mirrors, which were used for all printed structures presented here.

Z-Axis specifies if the piezo stage, the microscope z-drive or a combination of both were used for translation in z-direction.

Slicing distance indicates the distance between adjacent printing slices.

Hatching distance denotes the distance between neighboring hatching lines.

Doublet design 2	
Objective	25x LWD
Substrate	Nanoscribe DiLL substrate
Photoresist	IP-S
Laser power	70%
Scan speed	50, 000 µm/s
Z-Axis	Piezo and microscope z-drive
Slicing distance	0.25 µm
Hatching distance	0.5 µm

Table B.1. Fabrication parameters for doublet design 2, shown in Figure 3.4.

Doublet design 3 on imaging fiber bundle	
Objective	25x LWD
Substrate	Imaging fiber bundle, ⌀500 µm
Photoresist	IP-S
Laser power	70%
Scan speed	50, 000 µm/s
Z-Axis	Piezo and microscope z-drive
Slicing distance	0.2 µm
Hatching distance	0.5 µm

Table B.2. Fabrication parameters for doublet design 3 on imaging fiber bundle, shown in Figure 3.8a.

Doublet design 1 on imaging fiber bundle	
Objective	25x
Substrate	Imaging fiber bundle, ⌀500 µm
Photoresist	IP-S
Laser power	70%
Scan speed	50, 000 µm/s
Z-Axis	Microscope z-drive
Slicing distance	0.25 µm
Hatching distance	0.5 µm

Table B.3. Fabrication parameters for doublet design 1 on imaging fiber bundle, shown in Figure 3.8d.

Prism for TIR on imaging fiber bundle	
Objective	25x
Substrate	Imaging fiber bundle, ⌀500 µm
Photoresist	IP-S
Laser power	70%
Scan speed	50, 000 µm/s
Z-Axis	Microscope z-drive
Slicing distance	0.25 µm
Hatching distance	0.5 µm

Table B.4. Fabrication parameters for TIR prism on imaging fiber bundle, shown in Figure 3.9a.

Hollow prism on imaging fiber bundle	
Objective	25x LWD
Substrate	Imaging fiber bundle, ⌀500 µm
Photoresist	IP-S
Laser power	70%
Scan speed	50, 000 µm/s
Z-Axis	Microscope z-drive
Slicing distance	0.25 µm
Hatching distance	0.5 µm

Table B.5. Fabrication parameters for hollow prism on imaging fiber bundle, shown in Figure 3.10a.

Doublet objective on Al coated 3D printed mirror	
Objective	25x LWD
Substrate	Al coated 3D printed mirror (B.5)
Photoresist	IP-S
Laser power	70%
Scan speed	50, 000 µm/s
Z-Axis	Piezo and microscope z-drive
Slicing distance	0.25 µm
Hatching distance	0.5 µm

Table B.6. Fabrication parameters for doublet objective on Al coated 3D printed mirror, shown in Figure 3.10b.

Doublet design 3 on Raspberry Pi camera sensor	
Objective	25x LWD
Substrate	Raspberry Pi camera sensor
Photoresist	IP-S
Laser power	5%, 35%, 70%
Scan speed	10,000 µm/s, 50,000 µm/s
Z-Axis	Piezo and microscope z-drive
Slicing distance	0.25 µm
Hatching distance	0.5 µm

Table B.7. Fabrication parameters for doublet design 3 on Raspberry Pi camera sensor, shown in Figure 3.13a.

Doublet design 1 on Raspberry Pi camera sensor	
Objective	25x LWD
Substrate	Raspberry Pi camera sensor
Photoresist	IP-S
Laser power	5%, 35%, 70%
Scan speed	10,000 µm/s, 50,000 µm/s
Z-Axis	Microscope z-drive
Slicing distance	0.25 µm
Hatching distance	0.5 µm

Table B.8. Fabrication parameters for doublet design 1 on Raspberry Pi camera sensor, used for imaging characterization shown in Figure 3.14.

Doublet objective on distal chip sensor	
Objective	25x LWD
Substrate	Distal chip sensor
Photoresist	IP-S
Laser power	70%
Scan speed	50, 000 µm/s
Z-Axis	Piezo and microscope z-drive
Slicing distance	1 µm
Hatching distance	1 µm

TABLE B.9. Fabrication parameters for doublet objective on distal chip sensor,shown in Figure 3.15b.

Core-shell writing of spherical lenses: core	
Objective	25x
Substrate	Nanoscribe DiLL substrate
Photoresist	IP-S
Laser power	70%
Scan speed	50, 000 µm/s
Z-Axis	Piezo
Slicing distance	2 µm
Hatching distance	1 µm

TABLE B.10. Fabrication parameters for the core of the spherical lens with coarse hatching and slicing parameters, shown in Figure 3.18a.

Core-shell writing of spherical lenses: shell	
Objective	25x
Substrate	Nanoscribe DiLL substrate
Photoresist	IP-S
Laser power	70%
Scan speed	50,000 µm/s
Z-Axis	Piezo
Slicing distance	0.1 µm
Hatching distance	0.5 µm

Table B.11. Fabrication parameters for the shell of the spherical lens with fine hatching and slicing parameters, shown in Figure 3.18b.

Reference lens for core-shell printed lenses	
Objective	25x
Substrate	Nanoscribe DiLL substrate
Photoresist	IP-S
Laser power	70%
Scan speed	50,000 µm/s
Z-Axis	Piezo
Slicing distance	0.1 µm
Hatching distance	0.5 µm

Table B.12. Fabrication parameters for the spherical lens serving as reference for the core-shell printed lenses, used for the imaging characterization shown in Figure 3.18f.

Aspheric lens with 1 mm diameter	
Objective	10x
Substrate	18 × 18 mm² coverslip
Photoresist	IP-Visio
Laser power	100%
Scan speed	50,000 µm/s
Z-Axis	Piezo
Slicing distance	1.5 µm
Hatching distance	0.5 µm

Table B.13. Fabrication parameters for the aspheric lens with 1 mm diameter, shown on the left in Figure 4.1a.

Spherical half-ball lens with 1 mm diameter	
Objective	10x
Substrate	18 × 18 mm² coverslip
Photoresist	IP-Visio
Laser power	100%
Scan speed	50,000 µm/s
Z-Axis	Microscope z-drive
Slicing distance	1.5 µm
Hatching distance	0.5 µm

Table B.14. Fabrication parameters for the spherical half-ball lens with 1 mm diameter, shown in the middle in Figure 4.1a.

Spherical half-ball lens with 2 mm diameter	
Objective	10x
Substrate	18 × 18 mm² coverslip
Photoresist	IP-Visio
Laser power	100%
Scan speed	50,000 µm/s
Z-Axis	Microscope z-drive
Slicing distance	1.5 µm
Hatching distance	0.5 µm

Table B.15. Fabrication parameters for the spherical half-ball lens with 2 mm diameter, shown on the right in Figure 4.1a.

Cubes made from IP-S and IP-Visio	
Objective	10x
Substrate	18 × 18 mm² coverslip
Photoresist	IP-S and IP-Visio
Laser power	100%
Scan speed	50,000 µm/s
Z-Axis	Microscope z-drive
Slicing distance	1.5 µm
Hatching distance	0.5 µm

Table B.16. Fabrication parameters for the cubes made from IP-S and IP-Visio, shown in Figure 4.1b.

NANOSCRIBE QUANTUM X

The 3D printed structures in Chapter 5 were fabricated with the Nanoscribe Quantum X system. The 25x objective was used exclusively. The additional and altered printing parameters are explained below:

Printing mode indicates if the standard 3D printing mode or the 2.5D grayscale printing mode is used.

Laser power is now explicitly given in milliwatts when using the 3D printing mode. For the grayscale mode the laser power cannot be adjusted directly, as it is internally calculated from a calibration file.

Multilayer attenuation specifies the amount of surface smoothing in the grayscale mode, using a numeric value between 0 and 1. No smoothing is applied for a value of 0.

Z-Axis is no longer required, as there is only the translation stage for movement in z-direction.

Large-area plate for reflectivity measurements	
Printing mode	2.5D
Laser power	-
Multilayer attenuation	0
Substrate	10 × 10 mm² coverslip
Photoresist	IP-S
Scan speed	200, 000 µm/s
Slicing distance	1 µm
Hatching distance	0.2 µm

Table B.17. Fabrication parameters for the large-area plate for reflection measurements, shown in Figure 5.5a.

Blocks for transmission measurements	
Printing mode	3D
Laser power	70 mW
Multilayer attenuation	-
Substrate	10 × 10 mm² coverslip
Photoresist	IP-S
Scan speed	200, 000 µm/s
Slicing distance	0.25 µm
Hatching distance	0.2 µm

Table B.18. Fabrication parameters for the blocks for transmission measurements, shown in Figure 5.6a.

Supporting structure for dual-lens imaging system	
Printing mode	3D
Laser power	100 mW
Multilayer attenuation	-
Substrate	10 × 10 mm² coverslip
Photoresist	IP-S
Scan speed	200,000 µm/s
Slicing distance	1 µm
Hatching distance	0.2 µm

Table B.19. Fabrication parameters for the supporting structure of the upper lens in the dual-lens imaging system shown in Figure 5.9b.

Top and bottom lens of dual-lens imaging system	
Printing mode	2.5D
Laser power	-
Multilayer attenuation	0.8
Substrate	10 × 10 mm² coverslip
Photoresist	IP-S
Scan speed	200,000 µm/s
Slicing distance	1 µm
Hatching distance	0.2 µm

Table B.20. Fabrication parameters for the supporting structure of the upper lens in the dual-lens imaging system shown in Figure 5.9b.

LIST OF ACRONYMS

1PA	one-photon absorption
2PA	two-photon absorption
2PP	two-photon polymerization
2.5D	two-and-a-half dimensional
3D	three-dimensional
°C	degree Celsius
µm	micrometer
AFM	atomic force microscopy
ALD	atomic layer deposition
AOI	area of interest
AR	anti-reflective
Al	aluminum
Al_2O_3	alumina
Au	gold
B.C.	before Christ
CAD	computer-aided design
CMOS	complementary metal-oxide-semiconductor
DOE	diffractive optical element
DiLL	dip-in laser lithography
EDX	energy-dispersive x-ray spectroscopy
FIB	focused ion beam
GM	Göppert-Mayer
GRIN	gradient-index
H	hafnium
HfO_2	hafnia
Hz	hertz
LED	light emitting diode
LIGA	Lithographie, Galvanoformung, Abformung
MHz	megahertz

MTF	modulation transfer function
MgF_2	magnesium fluoride
N	nitrogen
NA	numerical aperture
NIR	near infrared
Ni	nickel
O	oxygen
PNG	portable network graphics
PPGT	Photonic Professional GT
R&D	research and development
RMS	root mean square
ROC	radius of curvature
SEM	scanning electron microscope
Si	silicon
SiO_2	silica
TIR	total internal reflection
Ti	titanium
TiN	titanium nitride
TiO_2	titania
USAF	United States Air Force
UV	ultraviolet
W	watt
cm	centimeter
fs	femtosecond
h	hour
m	meter
mW	milliwatt
mbar	millibar
min	minute
mm	millimeter
nm	nanometer
rpm	revolutions per minute
s	second

LIST OF FIGURES

Figure 1.1 Commercial endoscope and 3D printed endoscope prototype . . . 6
Figure 2.1 Principle of two-photon absorption . . . 12
Figure 2.2 Two-photon vs. one-photon fluorescence . . . 16
Figure 2.3 Polymerization reaction diagram . . . 18
Figure 2.4 Gaussian beam width . . . 19
Figure 2.5 Voxel size estimation for different laser powers . . . 24
Figure 2.6 3D model of a cube with extreme slicing and hatching parameters . . . 25
Figure 2.7 Nanoscribe PPGT overview . . . 26
Figure 2.8 Printing preparations for Photonic Professional GT . . . 28
Figure 2.9 Array printing of high structures with the Nanoscribe PPGT . . . 32
Figure 2.10 Maximum slope angle in confocal surface analysis . . . 35
Figure 2.11 Nanoscribe Quantum X setup overview . . . 36
Figure 2.12 Preparation of 2GL project for the Nanoscribe Quantum X 37
Figure 3.1 Multi-lens objectives with different numbers of optical surfaces . . . 39
Figure 3.2 Optical design parameters and CAD models of 3D printed doublet objectives . . . 41
Figure 3.3 Printing strategy for hanging parts in doublet objectives 42
Figure 3.4 Sample for shape optimization of doublet objectives . . . 44
Figure 3.5 Shape deviations and optimization of lens surfaces in doublet objectives . . . 46
Figure 3.6 Imaging quality of optimized and unoptimized doublet objectives . . . 48
Figure 3.7 Image conducting fiber for semi-flexible endoscopic devices 50
Figure 3.8 Doublet objectives on image conducting fibers . . . 52
Figure 3.9 3D printed prism on image conducting fiber . . . 54
Figure 3.10 Mirror and doublet objective on image conducting fiber 55
Figure 3.11 Raspberry Pi camera module . . . 57
Figure 3.12 Printing on camera sensor . . . 58
Figure 3.13 Imaging with Raspberry Pi camera sensor and doublet objective 3 . . . 59
Figure 3.14 Imaging with Raspberry Pi camera sensor and doublet design 1 . . . 60
Figure 3.15 Distal chip endoscopic devices . . . 62
Figure 3.16 Slicing strategy for the core-shell printing mode . . . 63

Figure 3.17 Hatching strategy for core-shell printing mode 64
Figure 3.18 Imaging quality of core-shell printed spherical lenses . 65
Figure 4.1 2PP fabrication of millimeter-sized singlet lenses 72
Figure 4.2 Spherical and aspherical singlet lens design for laser focusing 73
Figure 4.3 Surface analysis of aspherical lens with 1 mm diameter 74
Figure 4.4 Green laser focused by an aspherical lens with 1 mm diameter 75
Figure 4.5 Comparison of a 3D printed and a commercial half-ball lens with 1 mm diameter 77
Figure 4.6 Microscopy setup for imaging experiments with with millimeter-sized half-ball lenses 78
Figure 4.7 Imaging quality of a 3D printed half-ball lens with 1 mm diameter compared to a commercial lens 79
Figure 4.8 Visual comparison and modulation transfer function of half-ball lenses with 2 mm diameter 81
Figure 4.9 Deposition of SU-8 on 3D printed lenses for surface smoothing 83
Figure 4.10 Confocal microscopy comparison of smoothened and unsmoothened lenses 84
Figure 5.1 Directional vs. conformal coating techniques for AR coatings on multi-lens objectives 89
Figure 5.2 Atomic layer deposition precursors and deposition cycle overview 91
Figure 5.3 Design and material composition of AR coatings for 3D printed optics 94
Figure 5.4 Reflectivity measurements of AR coatings on flat glass substrates 96
Figure 5.5 Reflectivity of 3D printed flat large-area structure with AR coating 97
Figure 5.6 Test sample for transmission measurements through 3D printed structures with AR coating 100
Figure 5.7 Transmission experiments with uncoated and AR coated 3D printed test structures. 101
Figure 5.8 Quantitative comparison of transmission through AR coated and uncoated 3D printed polymer blocks 104
Figure 5.9 Doublet lens for AR coating experiments 106
Figure 5.10 Imaging quality of uncoated and AR coated doublet imaging systems 107
Figure 6.1 Ion beam structuring of Fresnel lens into a titanium mold insert 113
Figure 6.2 Injection compression molding setup for Fresnel lens replication 114

Figure 6.3 Shape accuracy measurements of titanium mold insert and replicated polymer Fresnel lens. 117
Figure 6.4 Optical setup for imaging characterization of Fresnel lenses 118
Figure 6.5 Measured and simulated images of USAF 1951 test target for different distances from the Fresnel lens. 119

LIST OF TABLES

Table 2.1 Parameters for voxel size estimation 23
Table A.1 Focusing objectives used with the Nanoscribe PPGT system 127
Table B.1 Fabrication parameters for doublet design 2, shown in Figure 3.4. 130
Table B.2 Fabrication parameters for doublet design 3 on imaging fiber bundle, shown in Figure 3.8a. 130
Table B.3 Fabrication parameters for doublet design 1 on imaging fiber bundle, shown in Figure 3.8d. 131
Table B.4 Fabrication parameters for TIR prism on imaging fiber bundle, shown in Figure 3.9a. 131
Table B.5 Fabrication parameters for hollow prism on imaging fiber bundle, shown in Figure 3.10a. 132
Table B.6 Fabrication parameters for doublet objective on Al coated 3D printed mirror, shown in Figure 3.10b. 132
Table B.7 Fabrication parameters for doublet design 3 on Raspberry Pi camera sensor, shown in Figure 3.13a. 133
Table B.8 Fabrication parameters for doublet design 1 on Raspberry Pi camera sensor, used for imaging characterization shown in Figure 3.14. 133
Table B.9 Fabrication parameters for doublet objective on distal chip sensor,shown in Figure 3.15b. 134
Table B.10 Fabrication parameters for the core of the spherical lens with coarse hatching and slicing parameters, shown in Figure 3.18a. 134
Table B.11 Fabrication parameters for the shell of the spherical lens with fine hatching and slicing parameters, shown in Figure 3.18b. 135
Table B.12 Fabrication parameters for the spherical lens serving as reference for the core-shell printed lenses, used for the imaging characterization shown in Figure 3.18f. 135
Table B.13 Fabrication parameters for the aspheric lens with 1 mm diameter, shown on the left in Figure 4.1a. 136
Table B.14 Fabrication parameters for the spherical half-ball lens with 1 mm diameter, shown in the middle in Figure 4.1a. 136
Table B.15 Fabrication parameters for the spherical half-ball lens with 2 mm diameter, shown on the right in Figure 4.1a. 137
Table B.16 Fabrication parameters for the cubes made from IP-S and IP-Visio, shown in Figure 4.1b. 137

Table B.17 Fabrication parameters for the large-area plate for reflection measurements, shown in Figure 5.5a. 139
Table B.18 Fabrication parameters for the blocks for transmission measurements, shown in Figure 5.6a. 139
Table B.19 Fabrication parameters for the supporting structure of the upper lens in the dual-lens imaging system shown in Figure 5.9b. 140
Table B.20 Fabrication parameters for the supporting structure of the upper lens in the dual-lens imaging system shown in Figure 5.9b. 140

BIBLIOGRAPHY

[1] Aristophanes: *The Clouds*, http://data.perseus.org/citations/urn:cts:greekLit:tlg0019.tlg003.perseus-eng1:731-775 (visited on June 5, 2022). Cit. on p. 5.

[2] G. W. Marshall, M. R. Lipsey, M. A. Heuer, C. Kot, R. Smarz, and M. Epstein: *An endodontic fiber optic endoscope for viewing instrumented root canals*. Journal of Endodontics **7**, 85–88 (1981). DOI 10.1016/S0099-2399(81)80248-8, cit. on pp. 5, 40.

[3] H. Iro, J. Zenk, M. Koch, and A. Bozzato: *Das Erlanger Konzept - Teil 1: Sialendoskopie bei obstruierenden Erkrankungen der großen Kopfspeicheldrüsen*, https://www.karlstorz.com/cps/rde/xbcr/karlstorz_assets/ASSETS/3315441.pdf (visited on June 5, 2022). Cit. on pp. 5, 6, 40.

[4] K. Schwertz: *An Introduction to the Optics Manufacturing Process* (2008). Cit. on p. 6.

[5] P. T. Brun, C. Inamura, D. Lizardo, G. Franchin, M. Stern, P. Houk, and N. Oxman: *The molten glass sewing machine*. Philosophical Transactions of the Royal Society A: Mathematical, Physical and Engineering Sciences **375** (2017). DOI 10.1098/rsta.2016.0156, cit. on p. 6.

[6] D. T. Nguyen, C. Meyers, T. D. Yee, N. A. Dudukovic, J. F. Destino, C. Zhu, E. B. Duoss, T. F. Baumann, T. Suratwala, J. E. Smay, and R. Dylla-Spears: *3D-Printed Transparent Glass*. Advanced Materials **29**, 1701181 (2017). DOI 10.1002/adma.201701181, cit. on p. 6.

[7] F. Kotz, A. S. Quick, P. Risch, T. Martin, T. Hoose, M. Thiel, D. Helmer, and B. E. Rapp: *Two-Photon Polymerization of Nanocomposites for the Fabrication of Transparent Fused Silica Glass Microstructures*. Advanced Materials **33**, 2006341 (2021). DOI 10.1002/adma.202006341, cit. on p. 6.

[8] D. G. Moore, L. Barbera, K. Masania, and A. R. Studart: *Three-dimensional printing of multicomponent glasses using phase-separating resins*. Nature Materials **19**, 212–217 (2020). DOI 10.1038/s41563-019-0525-y, cit. on p. 6.

[9] B. G. Assefa, M. Pekkarinen, H. Partanen, J. Biskop, J. Turunen, and J. Saarinen: *Imaging-quality 3D-printed centimeter-scale lens.* Optics Express **27**, 12630–12637 (2019).
DOI 10.1364/oe.27.012630, cit. on pp. 6, 70.

[10] G. Shao, R. Hai, and C. Sun: *3D Printing Customized Optical Lens in Minutes.* Advanced Optical Materials **8**, 1901646 (2020).
DOI 10.1002/adom.201901646, cit. on p. 6.

[11] F. Alam, M. Elsherif, B. AlQattan, A. Salih, S. M. Lee, A. K. Yetisen, S. Park, and H. Butt: *3D Printed Contact Lenses.* ACS Biomaterials Science and Engineering **7**, 794–803 (2021).
DOI 10.1021/acsbiomaterials.0c01470, cit. on p. 6.

[12] Y. Zhang, L. Wu, M. Zou, L. Zhang, and Y. Song: *Suppressing the Step Effect of 3D Printing for Constructing Contact Lenses.* Advanced Materials **34**, 2107249 (2022).
DOI 10.1002/adma.202107249, cit. on p. 6.

[13] X. Chen, W. Liu, B. Dong, J. Lee, H. O. T. Ware, H. F. Zhang, and C. Sun: *High-Speed 3D Printing of Millimeter-Size Customized Aspheric Imaging Lenses with Sub 7 nm Surface Roughness.* Advanced Materials **30**, 1705683 (2018).
DOI 10.1002/adma.201705683, cit. on pp. 6, 70, 82.

[14] V. Melissinaki, O. Tsilipakos, M. Kafesaki, M. Farsari, and S. Pissadakis: *Micro-Ring Resonator Devices Prototyped on Optical Fiber Tapers by Multi-Photon Lithography.* IEEE Journal of Selected Topics in Quantum Electronics **27**, 5900107 (2021).
DOI 10.1109/JSTQE.2021.3062716, cit. on p. 6.

[15] J. Li, S. Thiele, B. C. Quirk, R. W. Kirk, J. W. Verjans, E. Akers, C. A. Bursill, S. J. Nicholls, A. M. Herkommer, H. Giessen, and R. A. McLaughlin: *Ultrathin monolithic 3D printed optical coherence tomography endoscopy for preclinical and clinical use.* Light: Science and Applications **9**, 124 (2020).
DOI 10.1038/s41377-020-00365-w, cit. on p. 6.

[16] X. Q. Liu, R. Cheng, J. X. Zheng, S. N. Yang, B. X. Wang, B. F. Bai, Q. D. Chen, and H. B. Sun: *Wear-Resistant Blazed Gratings Fabricated by Etching-Assisted Femtosecond Laser Lithography.* Journal of Lightwave Technology **39**, 4690–4694 (2021).
DOI 10.1109/JLT.2021.3066976, cit. on p. 6.

[17] A. Landowski, J. Gutsche, S. Guckenbiehl, M. Schönberg, G. von Freymann, and A. Widera: *Coherent remote control of quantum emitters embedded in polymer waveguides.* APL Photonics **5**, 016101 (2020).
DOI 10.1063/1.5124618, cit. on p. 6.

[18] S. Woska, A. Münchinger, D. Beutel, E. Blasco, J. Hessenauer, O. Karayel, P. Rietz, S. Pfleging, R. Oberle, C. Rockstuhl, M. Wegener, and H. Kalt: *Tunable photonic devices by 3D laser printing of liquid crystal elastomers.* Optical Materials Express **10**, 2928–2943 (2020).
DOI 10.1364/ome.402855, cit. on p. 6.

[19] M. Blaicher, M. R. Billah, J. Kemal, T. Hoose, P. Marin-Palomo, A. Hofmann, Y. Kutuvantavida, C. Kieninger, P. I. Dietrich, M. Lauermann, S. Wolf, U. Troppenz, M. Moehrle, F. Merget, S. Skacel, J. Witzens, S. Randel, W. Freude, and C. Koos: *Hybrid multi-chip assembly of optical communication engines by in situ 3D nano-lithography.* Light: Science and Applications **9**, 71 (2020).
DOI 10.1038/s41377-020-0272-5, cit. on p. 6.

[20] A. Bertoncini and C. Liberale: *3D printed waveguides based on photonic crystal fiber designs for complex fiber-end photonic devices.* Optica **7**, 1487–1494 (2020).
DOI 10.1364/optica.397281, cit. on p. 6.

[21] L. Bremer, K. Weber, S. Fischbach, S. Thiele, M. Schmidt, A. Kaganskiy, S. Rodt, A. Herkommer, M. Sartison, S. L. Portalupi, P. Michler, H. Giessen, and S. Reitzenstein: *Quantum dot single-photon emission coupled into single-mode fibers with 3D printed micro-objectives.* APL Photonics **5**, 106101 (2020).
DOI 10.1063/5.0014921, cit. on p. 6.

[22] S. Schmidt, S. Thiele, A. Toulouse, C. Bösel, T. Tiess, A. Herkommer, H. Gross, and H. Giessen: *Tailored micro-optical freeform holograms for integrated complex beam shaping.* Optica **7**, 1279–1286 (2020).
DOI 10.1364/optica.395177, cit. on p. 6.

[23] M. Schmid, F. Sterl, S. Thiele, A. Herkommer, and H. Giessen: *3D printed hybrid refractive/diffractive achromat and apochromat for the visible wavelength range.* Optics Letters **46**, 2485–2488 (2021).
DOI 10.1364/OL.423196, cit. on pp. 6, 7.

[24] A. Toulouse, J. Drozella, S. Thiele, H. Giessen, and A. Herkommer: *3D-printed miniature spectrometer for the visible range with a 100 × 100 μm^2 footprint.* Light: Advanced Manufacturing **2**, 20–30 (2021).
DOI 10.37188/lam.2021.002, cit. on p. 6.

[25] G. S. Sokolovskii, V. Melissinaki, K. A. Fedorova, V. V. Dudelev, S. N. Losev, V. E. Bougrov, W. Sibbett, M. Farsari, and E. U. Rafailov: *3D laser nano-printing on fibre paves the way for super-focusing of multimode laser radiation.* Scientific Reports **8**, 14618 (2018).
DOI 10.1038/s41598-018-32970-6, cit. on p. 6.

[26] D. Schäffner, T. Preuschoff, S. Ristok, L. Brozio, M. Schlosser, H. Giessen, and G. Birkl: *Arrays of individually controllable optical tweezers based on 3D-printed microlens arrays.* Optics Express **28**, 8640–8645 (2020).
DOI 10.1364/oe.386243, cit. on p. 6.

[27] S. Ristok, S. Thiele, A. Toulouse, A. M. Herkommer, and H. Giessen: *Stitching-free 3D printing of millimeter-sized highly transparent spherical and aspherical optical components*. Optical Materials Express **10**, 2370–2378 (2020).
DOI 10.1364/ome.401724, cit. on pp. 6, 106.

[28] S. Ristok, P. Flad, and H. Giessen: *Atomic layer deposition of conformal anti-reflective coatings on complex 3D printed micro-optical systems*. Optical Materials Express **12**, 2063–2071 (2022).
DOI 10.1364/OME.454475, cit. on p. 6.

[29] K. Weber, D. Werdehausen, P. König, S. Thiele, M. Schmid, M. Decker, P. W. De Oliveira, A. Herkommer, and H. Giessen: *Tailored nanocomposites for 3D printed micro-optics*. Optical Materials Express **10**, 2345–2355 (2020).
DOI 10.1364/ome.399392, cit. on pp. 6, 7.

[30] K. Weber, F. Hütt, S. Thiele, T. Gissibl, A. Herkommer, and H. Giessen: *Single mode fiber based delivery of OAM light by 3D direct laser writing*. Optics Express **25**, 19672–19679 (2017).
DOI 10.1364/oe.25.019672, cit. on p. 6.

[31] A. Asadollahbaik, S. Thiele, K. Weber, A. Kumar, J. Drozella, F. Sterl, A. M. Herkommer, H. Giessen, and J. Fick: *Highly Efficient Dual-Fiber Optical Trapping with 3D Printed Diffractive Fresnel Lenses*. ACS Photonics **7**, 88–97 (2020).
DOI 10.1021/acsphotonics.9b01024, cit. on p. 6.

[32] M. Sartison, K. Weber, S. Thiele, L. Bremer, S. Fischbach, T. Herzog, S. Kolatschek, M. Jetter, S. Reitzenstein, A. Herkommer, P. Michler, S. L. Portalupi, and H. Giessen: *3D printed micro-optics for quantum technology: Optimised coupling of single quantum dot emission into a single-mode fibre*. Light: Advanced Manufacturing **2**, 6 (2021).
DOI 10.37188/lam.2021.006, cit. on p. 6.

[33] A. V. Baranikov, S.-Q. Li, D. Eschimese, X. Xu, S. Thiele, S. Ristok, R. M. Veetil, T. W. W. Mass, P. Moitra, H. Giessen, R. Paniagua-Dominguez, and A. I. Kuznetsov: *80-degree field-of-view transmissive metasurface-based spatial light modulator*, https://arxiv.org/abs/2107.11096.
Cit. on p. 6.

[34] S. Fischbach, A. Schlehahn, A. Thoma, N. Srocka, T. Gissibl, S. Ristok, S. Thiele, A. Kaganskiy, A. Strittmatter, T. Heindel, S. Rodt, A. Herkommer, H. Giessen, and S. Reitzenstein: *Single Quantum Dot with Microlens and 3D-Printed Micro-objective as Integrated Bright Single-Photon Source*. ACS Photonics **4**, 1327–1332 (2017).
DOI 10.1021/acsphotonics.7b00253, cit. on pp. 6, 70.

[35] M. Schmid, S. Thiele, A. Herkommer, and H. Giessen: *Three-dimensional direct laser written achromatic axicons and multi-component microlenses*. Optics Letters **43**, 5837–5840 (2018).
DOI 10.1364/ol.43.005837, cit. on p. 7.

[36] A. Toulouse, S. Thiele, H. Giessen, and A. M. Herkommer: *Alignment-free integration of apertures and nontransparent hulls into 3D-printed micro-optics*. Optics Letters **43**, 5283–5286 (2018).
DOI 10.1364/ol.43.005283, cit. on pp. 7, 70, 78, 88.

[37] K. Weber, Z. Wang, S. Thiele, A. Herkommer, and H. Giessen: *Distortion-free multi-element Hypergon wide-angle micro-objective obtained by femtosecond 3D printing*. Optics Letters **45**, 2784–2787 (2020).
DOI 10.1364/ol.392253, cit. on pp. 7, 70, 88.

[38] M. Göppert-Mayer: *Über Elementarakte mit zwei Quantensprüngen*. Annalen der Physik **401**, 273–294 (1931).
DOI 10.1002/andp.19314010303, cit. on p. 11.

[39] W. Kaiser and C. G. Garrett: *Two-photon excitation in CaF_2: Eu^{2+}*. Physical Review Letters **7**, 229–231 (1961).
DOI 10.1103/PhysRevLett.7.229, cit. on p. 11.

[40] H. Kodama: *Automatic method for fabricating a three-dimensional plastic model with photo-hardening polymer*. Review of Scientific Instruments **52**, 1770–1773 (1981).
DOI 10.1063/1.1136492, cit. on p. 11.

[41] S. Maruo, O. Nakamura, and S. Kawata: *Three-dimensional microfabrication with two-photon-absorbed photopolymerization*. Optics Letters **22**, 132–134 (1997).
DOI 10.1364/OL.22.000132, cit. on p. 11.

[42] K. S. Lee, R. H. Kim, D. Y. Yang, and S. H. Park: *Advances in 3D nano/microfabrication using two-photon initiated polymerization*. Progress in Polymer Science (Oxford) **33**, 631–681 (2008).
DOI 10.1016/j.progpolymsci.2008.01.001, cit. on p. 12.

[43] M. Rumi and J. W. Perry: *Two-photon absorption: an overview of measurements and principles*. Advances in Optics and Photonics **2**, 451–518 (2010).
DOI 10.1364/aop.2.000451, cit. on p. 12.

[44] J. Burris and T. J. McIlrath: *Theoretical study relating the two-photon absorption cross section to the susceptibility controlling four-wave mixing*. Journal of the Optical Society of America B **2**, 1313–1317 (1985).
DOI 10.1364/josab.2.001313, cit. on p. 13.

[45] R. W. V. Boyd: *Nonlinear optics*, 3. ed. edition, Elsevier, Academic Press, 2008.
ISBN 9780123694706, cit. on pp. 13–15.

[46] Y. R. V. Shen: *The principles of nonlinear optics*. Wiley-Interscience Publication, Wiley, 1984.
ISBN 0-471-88998-9, cit. on p. 14.

[47] R. Salem: *Characterization of two-photon absorption detectors for applications in high-speed optical systems*, http://photonics.umd.edu/wp-content/uploads/pubs/t-3/Salem_MS_Thesis_2003.pdf (visited on June 4, 2022).
Cit. on p. 15.

[48] M. Pawlicki, H. A. Collins, R. G. Denning, and H. L. Anderson: *Two-photon absorption and the design of two-photon dyes*. Angewandte Chemie - International Edition **48**, 3244–3266 (2009).
DOI 10.1002/anie.200805257, cit. on p. 16.

[49] S. Ruzin and H. Aaron: *1P vs 2P fluorescence imaging*, https://microscopy.berkeley.edu/tlm/2P/index.html (visited on May 14, 2022).
Cit. on p. 16.

[50] C. N. LaFratta and T. Baldacchini: *Two-photon polymerization metrology: Characterization methods of mechanisms and microstructures*. Micromachines **8**, 101 (2017).
DOI 10.3390/mi8040101, cit. on pp. 17, 18.

[51] K. Studer, C. Decker, E. Beck, and R. Schwalm: *Overcoming oxygen inhibition in UV-curing of acrylate coatings by carbon dioxide inerting, Part I*. Progress in Organic Coatings **48**, 92–100 (2003).
DOI 10.1016/S0300-9440(03)00120-6, cit. on p. 17.

[52] M. Awokola, W. Lenhard, H. Löffler, C. Flosbach, and P. Frese: *UV crosslinking of acryloyl functional polymers in the presence of oxygen*. Progress in Organic Coatings **44**, 211–216 (2002).
DOI 10.1016/S0300-9440(02)00015-2, cit. on p. 17.

[53] D. S. Correa, L. De Boni, A. J. G. Otuka, V. Tribuzi, and C. R. Mendonça: *Two-Photon Polymerization Fabrication of Doped Microstructures*. In: Polymerization, InTech, 2012.
Cit. on p. 19.

[54] R. V. Menzel: *Photonics: linear and nonlinear interactions of laser light and matter*, Springer, 2001.
ISBN 3540670742, cit. on p. 20.

[55] J. Serbin, A. Egbert, A. Ostendorf, B. N. Chichkov, R. Houbertz, G. Domann, J. Schulz, C. Cronauer, L. Fröhlich, and M. Popall: *Femtosecond laser-induced two-photon polymerization of inorganic–organic hybrid materials for applications in photonics*. Optics Letters **28**, 301–303 (2003).
DOI 10.1364/ol.28.000301, cit. on pp. 20–24, 33.

[56] K. Weber: *3D printed micro-optics: materials, methods and applications*. Hochschulschrift, 2022.
Cit. on pp. 20, 21.

[57] M. Schmid, D. Ludescher, and H. Giessen: *Optical properties of photoresists for femtosecond 3D printing: refractive index, extinction, luminescence-dose dependence, aging, heat treatment and comparison between 1-photon and 2-photon exposure.* Optical Materials Express **9**, 4564–4577 (2019).
DOI 10.1364/ome.9.004564, cit. on pp. 23, 71, 88.

[58] B. H. Cumpston, S. P. Ananthavel, S. Barlow, D. L. Dyer, J. E. Ehrlich, L. L. Erskine, A. A. Heikal, S. M. Kuebler, I.-Y. S. Lee, D. McCord-Maughon, J. Qin, H. Röckel, M. Rumi, X.-L. Wu, S. R. Marder, and J. W. Perry: *Two-photon polymerization initiators for three-dimensional optical data storage and microfabrication.* Nature **398**, 51–54 (1999).
DOI 10.1038/17989, cit. on p. 22.

[59] J. B. Mueller, J. Fischer, Y. J. Mange, T. Nann, and M. Wegener: *In-situ local temperature measurement during three-dimensional direct laser writing.* Applied Physics Letters **103**, 123107 (2013).
DOI 10.1063/1.4821556, cit. on pp. 29, 57, 102.

[60] A. Buček, A. Brablec, D. Kováčik, P. Sťahel, and M. Černák: *Glass bond adhesive strength improvement by DCSBD atmospheric-pressure plasma treatment.* International Journal of Adhesion and Adhesives **78**, 1–3 (2017).
DOI 10.1016/j.ijadhadh.2017.06.017, cit. on p. 29.

[61] S. Thiele, K. Arzenbacher, T. Gissibl, H. Giessen, and A. M. Herkommer: *3D-printed eagle eye: Compound microlens system for foveated imaging.* Science Advances **3**, e1602655 (2017).
DOI 10.1126/sciadv.1602655, cit. on pp. 32, 70, 125.

[62] Y. Liao, W. Li, Z. Zhan, H. Duan, P. Liu, Y. Chen, and Z. Wang: *3D-Printed Complex Microstructures with a Self-Sacrificial Structure Enabled by Grayscale Polymerization and Ultrasonic Treatment.* ACS Omega **6**, 18281–18288 (2021).
DOI 10.1021/acsomega.1c02177, cit. on p. 33.

[63] X. Z. Dong, Z. S. Zhao, and X. M. Duan: *Improving spatial resolution and reducing aspect ratio in multiphoton polymerization nanofabrication.* Applied Physics Letters **92**, 091113 (2008).
DOI 10.1063/1.2841042, cit. on p. 33.

[64] H. B. Sun, K. Takada, M. S. Kim, K. S. Lee, and S. Kawata: *Scaling laws of voxels in two-photon photopolymerization nanofabrication.* Applied Physics Letters **83**, 1104–1106 (2003).
DOI 10.1063/1.1599968, cit. on p. 33.

[65] E. H. Waller and G. von Freymann: *Spatio-temporal proximity characteristics in 3D μ-printing via multi-photon absorption.* Polymers **8**, 297 (2016).
DOI 10.3390/polym8080297, cit. on pp. 33, 76, 82.

[66] T. Gissibl, S. Thiele, A. Herkommer, and H. Giessen: *Two-photon direct laser writing of ultracompact multi-lens objectives*. Nature Photonics **10**, 554–560 (2016).
DOI 10.1038/nphoton.2016.121, cit. on pp. 39, 70, 112.

[67] T. Gissibl, M. Schmid, and H. Giessen: *Spatial beam intensity shaping using phase masks on single-mode optical fibers fabricated by femtosecond direct laser writing*. Optica **3**, 448–451 (2016).
DOI 10.1364/optica.3.000448, cit. on pp. 39, 70.

[68] T. Gissibl, S. Thiele, A. Herkommer, and H. Giessen: *Sub-micrometre accurate free-form optics by three-dimensional printing on single-mode fibres*. Nature Communications **7**, 11763 (2016).
DOI 10.1038/ncomms11763, cit. on pp. 39, 70.

[69] S. Thiele, T. Gissibl, H. Giessen, and A. M. Herkommer: *Ultra-compact on-chip LED collimation optics by 3D femtosecond direct laser writing*. Optics Letters **41**, 3029–3032 (2016).
DOI 10.1364/ol.41.003029, cit. on p. 39.

[70] A. Heinrich and M. Rank: *3D Printing of Optics*, 2018.
ISBN 9781510619982, cit. on p. 70.

[71] J. Y. Kim, N. B. Brauer, V. Fakhfouri, D. L. Boiko, E. Charbon, G. Grutzner, and J. Brugger: *Hybrid polymer microlens arrays with high numerical apertures fabricated using simple ink-jet printing technique*. Optical Materials Express **1**, 259–269 (2011).
DOI 10.1364/ome.1.000259, cit. on p. 70.

[72] P. I. Dietrich, M. Blaicher, I. Reuter, M. Billah, T. Hoose, A. Hofmann, C. Caer, R. Dangel, B. Offrein, U. Troppenz, M. Moehrle, W. Freude, and C. Koos: *In situ 3D nanoprinting of free-form coupling elements for hybrid photonic integration*. Nature Photonics **12**, 241–247 (2018).
DOI 10.1038/s41566-018-0133-4, cit. on p. 70.

[73] G. von Freymann, A. Ledermann, M. Thiel, I. Staude, S. Essig, K. Busch, and M. Wegener: *Three-dimensional nanostructures for photonics*. Advanced Functional Materials **20**, 1038–1052 (2010).
DOI 10.1002/adfm.200901838, cit. on p. 70.

[74] J. K. Hohmann, M. Renner, E. H. Waller, and G. von Freymann: *Three-Dimensional μ-Printing: An Enabling Technology*. Advanced Optical Materials **3**, 1488–1507 (2015).
DOI 10.1002/adom.201500328, cit. on p. 70.

[75] J. Li, P. Fejes, D. Lorenser, B. C. Quirk, P. B. Noble, R. W. Kirk, A. Orth, F. M. Wood, B. C. Gibson, D. D. Sampson, and R. A. McLaughlin: *Two-photon polymerisation 3D printed freeform micro-optics for optical coherence tomography fibre probes*. Scientific Reports **8**, 14789 (2018).
DOI 10.1038/s41598-018-32407-0, cit. on p. 70.

[76] Z. C. Ma, X. Y. Hu, Y. L. Zhang, X. Q. Liu, Z. S. Hou, L. G. Niu, L. Zhu, B. Han, Q. D. Chen, and H. B. Sun: *Smart Compound Eyes Enable Tunable Imaging*. Advanced Functional Materials **29**, 1903340 (2019). DOI 10.1002/adfm.201903340, cit. on p. 70.

[77] J.-J. Xu, W.-G. Yao, Z.-N. Tian, L. Wang, K.-M. Guan, Y. Xu, Q.-D. Chen, J.-A. Duan, and H.-B. Sun: *High Curvature Concave–Convex Microlens*. IEEE Photonics Technology Letters **27**, 2465–2468 (2015). DOI 10.1109/LPT.2015.2470195, cit. on p. 70.

[78] A. Žukauskas, M. Malinauskas, and E. Brasselet: *Monolithic generators of pseudo-nondiffracting optical vortex beams at the microscale*. Applied Physics Letters **103**, 181122 (2013). DOI 10.1063/1.4828662, cit. on p. 70.

[79] L. Jonušauskas, D. Gailevičius, S. Rekštytė, T. Baldacchini, S. Juodkazis, and M. Malinauskas: *Mesoscale laser 3D printing*. Optics Express **27**, 15205–15221 (2019). DOI 10.1364/oe.27.015205, cit. on p. 71.

[80] T. Gissibl, S. Wagner, J. Sykora, M. Schmid, and H. Giessen: *Refractive index measurements of photo-resists for three-dimensional direct laser writing*. Optical Materials Express **7**, 2293–2298 (2017). DOI 10.1364/ome.7.002293, cit. on p. 88.

[81] A. Toulouse, S. Thiele, H. Giessen, and A. M. Herkommer: *Super-fine inkjet process for alignment-free integration of non-transparent structures into 3D-printed micro-optics*. Advanced Fabrication Technologies for Micro/Nano Optics and Photonics XII, 109300W (2019). Cit. on p. 88.

[82] Y. Li, D. B. Fullager, E. Angelbello, D. Childers, G. Boreman, and T. Hofmann: *Broadband near-infrared antireflection coatings fabricated by three-dimensional direct laser writing*. Optics Letters **43**, 239–242 (2018). DOI 10.1364/ol.43.000239, cit. on p. 88.

[83] J. Canning, C. Clark, M. Dayao, D. de LaMela, M. Logozzo, and J. Zhao: *Anti-Reflection Coatings on 3D-Printed Components*. Coatings **11**, 1519 (2021). DOI 10.3390/coatings11121519, cit. on p. 88.

[84] H. Jiang, W. Zhao, C. Li, and Y. Wang: *Polymer nanoparticle-based porous antireflective coating on flexible plastic substrate*. Polymer **52**, 778–785 (2011). DOI 10.1016/j.polymer.2010.12.036, cit. on p. 88.

[85] K. C. Krogman, T. Druffel, and M. K. Sunkara: *Anti-reflective optical coatings incorporating nanoparticles*. Nanotechnology **16**, S338–S343 (2005). DOI 10.1088/0957-4484/16/7/005, cit. on p. 88.

[86] J. Moghal, S. Reid, L. Hagerty, M. Gardener, and G. Wakefield: *Development of single layer nanoparticle anti-reflection coating for polymer substrates*. Thin Solid Films **534**, 541–545 (2013). DOI 10.1016/j.tsf.2013.03.005, cit. on p. 90.

[87] R. Shakoury and R. R. Willey: *Ion assisted deposition of magnesium fluoride films at low temperature.* Optical and Quantum Electronics **50**, 322 (2018).
DOI 10.1007/s11082-018-1594-x, cit. on p. 90.

[88] A. Kaless, U. Schulz, P. Munzert, and N. Kaiser: *NANO-motheye antireflection pattern by plasma treatment of polymers.* Surface and Coatings Technology **200**, 58–61 (2005).
DOI 10.1016/j.surfcoat.2005.01.067, cit. on p. 90.

[89] K. Pfeiffer, U. Schulz, A. Tünnermann, and A. Szeghalmi: *Antireflection coatings for strongly curved glass lenses by atomic layer deposition.* Coatings **7**, 118 (2017).
DOI 10.3390/coatings7080118, cit. on p. 90.

[90] K. Pfeiffer, L. Ghazaryan, U. Schulz, and A. Szeghalmi: *Wide-Angle Broadband Antireflection Coatings Prepared by Atomic Layer Deposition.* ACS Applied Materials and Interfaces **11**, 21887–21894 (2019).
DOI 10.1021/acsami.9b03125, cit. on p. 90.

[91] N. T. Gabriel and J. J. Talghader: *Optical coatings in microscale channels by atomic layer deposition.* Applied Optics **49**, 1242–1248 (2010).
DOI 10.1364/AO.49.001242, cit. on p. 90.

[92] A. Szeghalmi, M. Helgert, R. Brunner, F. Heyroth, U. Gösele, and M. Knez: *Atomic layer deposition of Al_2O_3 and TiO_2 multilayers for applications as bandpass filters and antireflection coatings.* Applied Optics **48**, 1727–1732 (2009).
DOI 10.1364/AO.48.001727, cit. on p. 90.

[93] L. Patsiouras, E. Skotadis, N. Gialama, C. Drivas, S. Kennou, K. Giannakopoulos, and D. Tsoukalas: *Atomic layer deposited Al_2O_3 thin films as humidity barrier coatings for nanoparticle-based strain sensors.* Nanotechnology **29**, 465706 (2018).
DOI 10.1088/1361-6528/aaddbe, cit. on p. 90.

[94] P. Paul, K. Pfeiffer, and A. Szeghalmi: *Antireflection coating on PMMA substrates by atomic layer deposition.* Coatings **10**, 64 (2020).
DOI 10.3390/coatings10010064, cit. on p. 103.

[95] A. A. Michelson: *Studies in optics.* Phoenix science series ; 514, 3. impr. edition, Chicago Univ. Press, 1962.
Cit. on p. 108.

[96] M. Sortino, G. Totis, and E. Kuljanic: *Comparison of injection molding technologies for the production of micro-optical devices.* Procedia Engineering **69**, 1296–1305 (2014).
DOI 10.1016/j.proeng.2014.03.122, cit. on p. 112.

[97] H. N. Hansen, R. J. Hocken, and G. Tosello: *Replication of micro and nano surface geometries.* CIRP Annals - Manufacturing Technology **60**, 695–714 (2011).
DOI 10.1016/j.cirp.2011.05.008, cit. on p. 112.

[98] M. Roeder, T. Guenther, and A. Zimmermann: *Review on fabrication technologies for optical mold inserts*. Micromachines **10**, 233 (2019).
DOI 10.3390/mi10040233, cit. on p. 112.

[99] M. Roeder, M. Drexler, T. Rothermel, T. Meissner, T. Guenther, and A. Zimmermann: *Injection compression molded microlens arrays for hyperspectral imaging*. Micromachines **9**, 355 (2018).
DOI 10.3390/mi9070355, cit. on p. 112.

[100] C. Rytka, P. M. Kristiansen, and A. Neyer: *Iso- and variothermal injection compression moulding of polymer micro- and nanostructures for optical and medical applications*. Journal of Micromechanics and Microengineering **25**, 065008 (2015).
DOI 10.1088/0960-1317/25/6/065008, cit. on pp. 112, 120.

[101] M. Roeder, S. Thiele, D. Hera, C. Pruss, T. Guenther, W. Osten, and A. Zimmermann: *Fabrication of curved diffractive optical elements by means of laser direct writing, electroplating, and injection compression molding*. Journal of Manufacturing Processes **47**, 402–409 (2019).
DOI 10.1016/j.jmapro.2019.10.012, cit. on p. 112.

[102] T. Mappes, M. Worgull, M. Heckele, and J. Mohr: *Submicron polymer structures with X-ray lithography and hot embossing*. Microsystem Technologies **14**, 1721–1725 (2008).
DOI 10.1007/s00542-007-0499-6, cit. on p. 112.

[103] Y. Yao, H. Liu, Y. Wang, Y. Li, B. Song, A. Bratkovsk, S. Y. Wang, and W. Wu: *Nanoimprint lithography: an enabling technology for nanophotonics*. Applied Physics A: Materials Science and Processing **121**, 327–333 (2015).
DOI 10.1007/s00339-015-9438-z, cit. on p. 112.

[104] Y. Kanamori, M. Okochi, and K. Hane: *Fabrication of antireflection subwavelength gratings at the tips of optical fibers using UV nanoimprint lithography*. Optics Express **21**, 322–328 (2013).
DOI 10.1364/oe.21.000322, cit. on p. 112.

[105] S. Y. Chou, P. R. Krauss, and P. J. Renstrom: *Imprint lithography with 25-nanometer resolution*. Science **272**, 85–87 (1996).
DOI 10.1126/science.272.5258.85, cit. on p. 112.

[106] S. Kang: *Micro / Nano Replication : Processes and Applications*, John Wiley & Sons, Incorporated, 2012.
ISBN 9781118146934, cit. on p. 112.

[107] M. T. Gale: *Replication techniques for diffractive optical elements*. Microelectronic Engineering **34**, 321–339 (1997).
DOI 10.1016/S0167-9317(97)00189-5, cit. on p. 112.

[108] G. Tosello, H. N. Hansen, S. Gasparin, J. A. Albajez, and J. I. Esmoris: *Surface wear of TiN coated nickel tool during the injection moulding of polymer micro Fresnel lenses.* CIRP Annals - Manufacturing Technology **61**, 535–538 (2012).
DOI 10.1016/j.cirp.2012.03.016, cit. on p. 112.

[109] F. Watt, A. A. Bettiol, J. A. van Kan, E. J. Teo, and M. B. H. Breese: *Ion Beam Lithography and Nanofabrication: a Review.* International Journal of Nanoscience **4**, 269–286 (2005).
DOI 10.1142/S0219581X05003139, cit. on p. 112.

[110] J. E. Hergert, D. J. Glugla, A. C. Sullivan, M. D. Alim, and R. R. McLeod: *High efficiency Fresnel lens design and fabrication in a two-stage photopolymer.* Optics Letters **44**, 1540–1543 (2019).
DOI 10.1364/ol.44.001540, cit. on p. 112.

[111] S. Thiele, C. Pruss, A. M. Herkommer, and H. Giessen: *3D printed stacked diffractive microlenses.* Opt. Express **27**, 35621–35630 (2019).
DOI 10.1364/OE.27.035621, cit. on p. 112.

[112] D. Loaldi, D. Quagliotti, M. Calaon, P. Parenti, M. Annoni, and G. Tosello: *Manufacturing signatures of injection molding and injection compression molding for micro-structured polymer fresnel lens production.* Micromachines **9**, 653 (2018).
DOI 10.3390/mi9120653, cit. on p. 112.

[113] S. Y. Yang and M. Z. Ke: *Experimental study on the effects of adding compression to injection molding process.* Advances in Polymer Technology **14**, 15–24 (1995).
DOI 10.1002/adv.1995.060140102, cit. on p. 115.

[114] P. Scholz, U. Kerst, C. Boit, T. Kujawa, and T. Lundquist: *Instant solid immersion lens creation in silicon with a focused ion beam - Comparing refractive and diffractive methods.* Conference Proceedings from the International Symposium for Testing and Failure Analysis, 46–53 (2011).
DOI 10.31399/asm.cp.istfa2011p0046, cit. on p. 115.

[115] *Micro-optics: elements, systems and applications*, Taylor & Francis, 1997.
ISBN 0-7484-0481-3, cit. on p. 120.

[116] H. Zappe: *Fundamentals of Micro-Optics*, Cambridge University Press, 2010.
ISBN 9780511781797, cit. on p. 120.

[117] A. Toulouse, J. Drozella, P. Motzfeld, N. Fahrbach, V. Aslani, S. Thiele, H. Giessen, and A. M. Herkommer: *Ultra-compact 3D-printed wide-angle cameras realized by multi-aperture freeform optical design.* Optics Express **30**, 707 (2022).
DOI 10.1364/oe.439963, cit. on p. 125.

[118] https://www.nanoscribe.com/en/products/xlf-print-set (visited on June 3, 2022).
Cit. on p. 126.

[119] T. Frenzel, M. Kadic, and M. Wegener: *Three-dimensional mechanical metamaterials with a twist*. Science **358**, 1072–1074 (2017). DOI 10.1126/science.aao4640, cit. on p. 126.

[120] V. Hahn, T. Messer, N. M. Bojanowski, E. R. Curticean, I. Wacker, R. R. Schröder, E. Blasco, and M. Wegener: *Two-step absorption instead of two-photon absorption in 3D nanoprinting*. Nature Photonics **15**, 932–938 (2021). DOI 10.1038/s41566-021-00906-8, cit. on p. 126.

ACKNOWLEDGMENTS

During the last years I received help from many people on many different subjects, which ultimately contributed to the successful completion of my work. Here, I would like to express my gratitude to all those who supported me throughout the course of my doctoral thesis.

In particular, I would like to thank:

- Prof. Dr. Harald Gießen for offering me a position in such an interesting and vibrant field of research.
- Prof. Dr. Alois Herkommer and Prof. Dr. Christian Holm for taking the time to be part of my examination committee.
- Dr. Timo Gissibl for laying the ground-work for 3D printing of micro-optics at our institute and for introducing me to this field.
- Dr. Simon Thiele and Dr. Andrea Toulouse for many highly advanced optical designs, help with different experimental challenges and a great collaboration in general.
- Erich Steinbeißer from the Institute of Applied Optics for his help with MTF measurements.
- Dr. Christine von Rekowski for all the help with administrative matters.
- Dr. Mario Hentschel, Monika Ubl and Philipp Flad, who are doing an amazing job at making our cleanroom such a convenient workplace.
- Philipp Flad for the great collaboration on anti-reflective coatings for polymer micro-optics, his support with atomic layer deposition and coating design.

- Dr. Mario Hentschel, Julian Karst and Moritz Flöss for many refreshing lunch and coffee breaks with numerous inspiring scientific and non-scientific conversations.

- Moritz Flöss for his support with photography on several occasions.

- Dr. Mario Hentschel and Dr. Marcel Röder for great collaboration on the fabrication of diffractive optical elements by injection-compression molding.

- Dr. Ksenia Weber, Michael Schmid and Paul Ruchka from the 3D printing team for great collaboration and many productive discussions about this field.

- Nanoscribe GmbH & Co. KG for providing and developing the 3D printing systems utilized in this work, and for their fast and reliable feedback and support when we were often pushing the limits of their devices.

- Ralf Kamella and his team from the mechanical workshop for the fabrication and help with the design of mechanical components.

- My parents and my sisters, who supported me during all situations and always believed in the success of my work.

- My girlfriend Madeleine and our son Jonathan for their constant love and support, and for keeping up my motivation.

- All present and former colleagues from PI4 for the nice working atmosphere, the relaxing and funny group trips and after-work activities.